P 20

N77-13390

VECTOR MAGNETOMETER DESIGN STUDY: ANAYSIS OF A TRIAXIAL FLUXGATE SENSOR DESIGN DEMONSTRATES THAT ALL MAGSAT VECTOR MAGNETOMETER SPECIFICATIONS CAN BE MET

GODDARD SPACE FLIGHT CENTER
GREENBELT, MD

NOV 76

NASA CR-144825

VECTOR MAGNETOMETER DESIGN STUDY

Analysis of a triaxial fluxgate sensor design demonstrates that all MAGSAT Vector Magnetometer specifications can be met

November 1976
Final Report

Prepared for
GODDARD SPACE FLIGHT CENTER
Greenbelt, Maryland 20771

Time·Zero Laboratories
Aerospace Division
Ball Brothers Research Corporation
A SUBSIDIARY OF BALL CORPORATION

1488 WEST 178th STREET • GARDENA • CALIFORNIA 90247 • (213) 327-2221 · 770-8210
TWX (910) 346-7637

1. Report No.	2. Government Accession No.	3. Recipient's Catalog No.

4. Title and Subtitle Vector Magnetometer Design Study
Analysis of a triaxial fluxgate sensor design demonstrates that all MAGSAT Vector Magnetometer specifications can be met.

5. Report Date November 1976

6. Performing Organization Code

7. Author(s) D. F. Adams, U. G. Hartman, L. L. Lazarow, J. O. Maloy, G. W. Mohler

8. Performing Organization Report No.

9. Performing Organization Name and Address
Ball Brothers Research Corporation
Aerospace Division
Time-Zero Laboratories
1488 W. 178th St., Gardena, CA 90247

10. Work Unit No.

11. Contract or Grant No. NAS 5-23661

12. Sponsoring Agency Name and Address
Goddard Space Flight Center
Greenbelt, Maryland 20771
Jack O'Brien Code 406

13. Type of Report and Period Covered

14. Sponsoring Agency Code

15. Supplementary Notes

16. Abstract

The design of the project MAGSAT Vector Magnetometer selected for analysis is capable of exceeding the required accuracy of 5γ per vector field component. The principal elements that assure this performance level are very low power dissipation triaxial feedback coils surrounding ring core fluxgates and temperature control of the critical components of two-loop feedback electronics. An analysis of the calibration problem points to the need for improved test facilities.

17. Key Words (Selected by Author(s))	18. Distribution Statement
Vector Magnetometer triaxial feedback graphite-epoxy.	

19. Security Classif. (of this report)	20. Security Classif. (of this page)	21. No. of Pages	22. Price*
		170	

* For sale by the National Technical Information Service, Springfield, Virginia 22151.

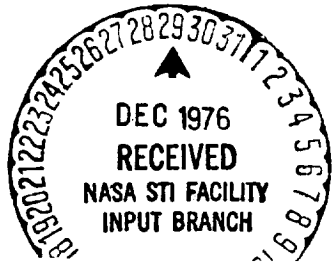

PREFACE

This report is the result of a Vector Magnetometer Design Study sponsored by Goddard Space Flight Center, Contract No. NAS 5-23661.

Objectives - The Vector Magnetometer study was undertaken to establish the feasibility of a magnetometer capable of measuring the three components of the earth's magnetic field with an absolute accuracy of 5γ (1γ = 1 nT) and with an axis alignment stability of 5 seconds of arc.

Scope - The study consisted of the selection and analysis of a specific design approach to establish the feasibility of building such an advanced vector magnetometer. The study also included consideration of the problem of calibration and alignment with the required accuracy.

Conclusions - The study concluded that the design of a vector magnetometer meeting the stringent accuracy requirements is indeed feasible. The selected design uses triaxial vector magnetic field feedback to reduce the effect of fluxgate sensor misalignments, and a graphite-epoxy structure with multilayer thermal shields to attain the required structural stability. The calibration study concluded that the difficult calibration and alignment requirements can be met provided that a magnetic field can be generated whose absolute position is known with sufficient accuracy.

Recommendations -It is recommended that some of the numerical estimates in the study be checked by further analysis and some detailed testing to confirm sensor characteristics. More work on the problem of providing a magnetic field where orientation is well known (or accurately measurable) is needed.

AUTHORS

Dr. Donald F. Adams, Professor of Mechanical Engineering, University of Wyoming, Laramie. Dr. Adams, a recognized expert in the design and application of graphite epoxy materials, assisted in the selection of the mechanical configuration and the analyses presented in Appendix C.

Dr. Ulli G. Hartmann, Staff Scientist, TZL. Dr. Hartmann performed the calibration analysis.

Mr. Lawrence L. Lazarow, Senior Mechanical Engineer, TZL. Mr. Lazarow performed the structural design and analysis.

Dr. J. Owen Maloy, Staff Scientist, TZL. Dr. Maloy performed the magnetometer Sensor design and thermal analysis.

Mr. George W. Mohler, Engineering Manager, TZL. Mr. Mohler performed the electronics design study assisted by Mr. James F. Sherman.

ACKNOWLEDGEMENTS

Time-Zero wishes to acknowledge the contributions to the study made by conversations with the following magnetometer experts;

Dr. Mario H. Acuna	NASA-GSFC
Dr. W. Harry Farthing	NASA-GSFC
Mr. Allan M. A. Frandsen	JPL
Dr. Edward J. Smith	JPL

In particular, Dr. Farthing and Dr. Acuna contributed ideas used directly in the report, although TZL takes full responsibility for the ideas presented.

TABLE OF CONTENTS

	Page No.
SECTION 1 - SUMMARY	
Motivation for the Vector Magnetometer Study and its Tasks	1-2
Description of the Design Approach	1-4
Compliance with Study Contract Specification	1-6
Principal Conclusions of the Study	1-8
Recommendations for Hardware Development and Further Study	1-10
SECTION 2 - MAGNETOMETER DESIGN REQUIREMENTS	
Review of Vector Magnetometer Performance Requirements	2-2
Components of the Vector Magnetometer	2-4
Allocation of the Errors to Sources	2-6
SECTION 3 - MAGNETOMETER SYSTEMS DESIGN	
Meeting the Performance Requirements	3-2
Functional Description of the System Design	3-4
Physical and Interface Characteristics for the Recommended Sensor Design	3-6
SECTION 4 - SENSOR DESIGN	
4.1 - CONFIGURATION ANALYSIS	
Summary of Optimum Sensor Configuration Analysis	4-2
Dependence of Sensor and Feedback Configurations on Misalignment Sensitivity	4-4
Factors Influencing Magnetometer Alignment Stability	4-6
Calculation of the Misalignment Sensitivity of a Single-Axis Magnetometer	4-8
Use of Triaxial Feedback to Reduce Sensor Misalignment Sensitivity	4-10
Uniformity Requirements for the Triaxial Feedback Field	4-12
Dependence of Noise and Offset on Fluxgate Dimensions	4-14
Optimization of Fluxgate Geometry Under the Noise and Size Constraints	4-16
Finding the Simplest Arrangement for Generating a Uniform Feedback Field	4-18
Magnetic Field of Coil Pairs	4-20
Cancellation of the External Field	4-22
Modifying the Feedback Coil Spacing to Minimize Coil Size	4-24
Derivation of Structural Stability Requirements	4-26
4.2 - SENSOR DESIGN AND PERFORMANCE ANALYSIS	
Design of the Sensor for High Stability	4-28
Detailed Design of the Fluxgate Sensors	4-30
Magnetic Configuration of the Feedback Coils	4-32
Electrical Design of the Feedback Coils	4-34
Mechanical and Thermal Design of the Sensor Assembly	4-36
Analysis of Structural Stability	4-38
Strategy for Controlling Thermal Effects	4-40
Analysis of Self-Heating Effects	4-42

Page No.

Design of the Thermal Control System. 4-44
Design of the Thermal Controller. 4-46
Performance of the Thermal Shielding 4-48
Estimates of Sensor Stability 4-50

SECTION 5 - ELECTRONICS DESIGN
Summary of Electronics Analysis 5-2
5.1 - CONFIGURATION ANALYSIS
Characteristics of the Single-Loop System 5-4
Characteristics of the Two-Loop System. 5-6
Frequency Analysis of the Single-Loop System and Inner. . .
Loop of Two-Loop System 5-8
Error Analysis of the Single-Loop System and Inner Loop
of Two-Loop System 5-10
5.2 - ELECTRONICS DESIGN AND PERFORMANCE ANALYSIS
Summary of Two-Loop System Design Parameters 5-12
Design of the Reference Generator and the Probe Drive . . . 5-14
Design of the Second Harmonic Amplifier 5-16
Design of the Demodulator and Integrator 5-18
Design of the 12-Bit ADC. 5-20
Design of the Feedback Current Generator 5-22
Design of the Digital-to-Analog Converter (DAC) 5-24
Alternative DAC Configurations. 5-26
Auxiliary Subsystems and Power Analysis 5-28
Packaging and Thermal Control of the Electronics 5-30

SECTION 6 - CALIBRATION AND ALIGNMENT
Nature of the Calibration and Alignment Problem 6-2
Identification of Contributions to Response Matrix 6-4
Determination of the Response Matrix 6-8
How Alignment is Determined. 6-12
Summary of Accuracy and Equipment Requirements. 6-14

APPENDIX A - NOISE PERFORMANCE OF FLUXGATE SENSORS . A-1

APPENDIX B - DETAILS OF STRUCTURAL ANALYSIS

APPENDIX C - ANALYSIS OF STRUCTURAL STABILITY. C-1

APPENDIX D - PACKAGING OF THE ELECTRONICS. D-1

LIST OF ILLUSTRATIONS

Figure No.		Page No.
1-1	Exploded View of the Sensor.	1-5
2-1	Block Diagram for One Axis of a Vector Magnetometer.	2-5
3-1	Block Diagram for Vector Magnetometer	3-5
4-1	Single-Axis Vector Magntometer.	4-5
4-2	Triaxial - Feedback Vector Magnetometer	4-5
4-3	Typical Fluxgate Sensor	4-9
4-4	Arrangement of Fluxgate Sensors Inside Feedback Coils	4-13
4-5	Fluxgate Sensor Mounting	4-17
4-6	Complexity and Access	4-19
4-7	Symmetrical Coil Pair	4-21
4-8	Variation in Axial Field for Various Radial Offsets in Central Plane	4-25
4-9	Conceptual Sensor Arrangement	4-29
4-10	Fluxgate Sensor	4-31
4-11	Sensor Mounting on a Plastic Cube	4-31
4-12	Variation in Axial Field for Various Radial Offsets in Central Plane	4-33
4-13	Radial Field Difference Between Parallel and Perpendicular Sensors as a Function of Coil Separation	4-33
4-14	Coil Schematic.	4-35
4-15	Sensor Mechanical Design.	4-37
4-16	Orbital Heating	4-41
4-17	Approximate Thermal Model	4-43
4-18	Thermal Control System	4-45
4-19	Temperature Controller Block Diagram	4-47
4-20	Thermal Model for Temperature Gradient Analysis	4-49
5-1	Single-Loop System	5-3
5-2	Two-Loop System	5-3
5-3	Single-Loop System is Characterized by the Need for Wide Bandwidth	5-5
5-4	Two-Loop System	5-7
5-5	Typical Input/Output Curves for Increasing and Decreasing Inputs	5-7
5-6	Reference Generator and Probe Drive	5-15
5-7	Second Harmonic Amplifier	5-17
5-8	Demodulator-Integrator Design	5-19
5-9	Design of the 12-bit ADC	5-20
5-10	Feedback Current Generator	5-22
5-11	Digital-to-Analog Converter (DAC)	5-24
5-12	Constant Current Source	5-27
5-13	DAC Basically a Pulse-Width Modulator	5-27
5-14	Auxiliary Circuits	5-29
5-15	Packaging of the Electronics	5-31
6-1	Absolute Orientation	6-13

LIST OF ILLUSTRATIONS

APPENDICES

	Page No.
Cylindrical Geometry used in Calculation	A-5
Analysis of Fluxgate Sensitivity.	A-7
Magnetostriction Model	A-11
Variation of Flux and Magnetostriction During the Sensor Drive Cycle	A-11
Magnetostrictive Error Voltage.	A-11
Deflection of Spherical Coil Form.	C-2
The Sphere Conservatively Modeled as a Hollow Cylinder with 0.2-inch thick walls	C-2
Deflection of Coil With Respect to Mirror Mount	C-3
Find Deflection of Base	C-3
Deflection and f_n of Sensor Support	C-5
Resonant Frequency.	D-2

LIST OF TABLES

Table No.		Page No.
1-1	Objectives of the MAGSAT Mission	1-3
1-2	Tasks Performed in the Vector Magnetometer Study	1-3
1-3	Principal Design Features	1-5
1-4	Compliance with Study Contract Specification	1-7
1-5	Conclusion of Vector Magnetometer Study	1-9
1-6	Hardware Development Recommendations	1-11
1-7	Further Studies Recommended	1-11
2-1	Performance Requirements for Vector Magnetic Field Measurements	2-3
2-2	Design Error Budget for the Vector Magnetometer	2-7
3-1	How the Performance Requirements can be Met	3-3
3-2	Main Features of Vector Magnetometer Design	3-5
3-3	Overall Weight and Power	3-7
4-1	Sensor Configuration Analysis Summary	4-3
4-2	Alignment Stability Factors	4-7
4-3	How Triaxial Feedback Reduces Misalignment Sensitivity	4-11
4-4	Requirements for Field Uniformity	4-13
4-5	Noise Equivalent Field of a Ring-Core Fluxgate	4-15
4-6	Offset Equivalent Field	4-15
4-7	Reasons for Desiring the Simplest Possible Configuration	4-19
4-8	Spherical Harmonic Expansion for Field of a Coil Pair	4-21
4-9	Strength of External Field for Helmholtz Coils	4-23
4-10	General Expression for the Field Produced by a Current	4-25
4-11	Components of the Field of a Circular Coil	4-25
4-12	Sensitivity of the Field to Dimensional Variations	4-27
4-13	Dimensional Tolerances	4-27
4-14	Features of the Recommended Sensor Design	4-29
4-15	Design Requirements and Approaches	4-37
4-16	Analysis of Critical Elements	4-39
4-17	Thermal Control Strategy	4-41
4-18	Thermal Error Summary	4-43
4-19	Thermal Problems and Control Approach	4-45
4-20	Spatial Dependence of Vector Potential from Periodic Current Distribution	4-47
4-21	Estimated Temperature Gradients Across Components	4-49
4-22	Comparison of Estimated and Required Performance	4-51
5-1	Comparison of Inner-Loop of Two-Loop System with Single-Loop System	5-7
5-2	Equations for Expressing the Frequency Response Characteristics of the Single-Loop System	5-9
5-3	Partial Derivatives for Various Frequencies	5-11

Table No.		Page No.
5-4	Summary of Two-Loop System Error Budget	5-13
5-5	Determination of Output Count	5-21
5-6	ADC System Errors	5-21
5-7	Component Instabilities used in Error Analysis	5-23
5-8	Analysis of Offset and Scale Factor Errors	5-23
5-9	Component Instabilities used in Error Analysis	5-25
5-10	Analysis of Offset and Scale Factor Errors	5-25
5-11	Power Estimate	5-29
5-12	Design Requirement and Approaches	5-31
6-1	Budgeted Errors	6-3
6-2	Summary of Contributions to Response Matrix	6-7
6-3	Summary of Equations	6-11
6-4	Summary of Equations	6-13
6-5	Requirements	6-15
	The Noise Equivalent Field for a Fluxgate Magnetometer	A-3
	Calculation of NE ΔB for TZ Sensor	A-9

SECTION 1
SUMMARY

Motivation for the Vector Magnetometer and its Tasks. 1-2

Description of the Design Approach 1-4

Compliance with Study Contract Specification. . . 1-6

Principal Conclusions of the Study 1-8

Recommendations for Hardware Development and Further Study. 1-10

MOTIVATION FOR THE VECTOR MAGNETOMETER STUDY AND ITS TASKS

The study was undertaken to establish the feasibility of developing a satellite-borne magnetometer required to make a more accurate map of the earth's magnetic field.

In the late 1970's a Scout-launched Application Explorer Satellite, the MAGSAT, will carry advanced vector and scalar magnetometers into earth orbit for the purpose of making a high accuracy global survey of the earth's magnetic field.

To obtain high resolution, a low polar orbit will be used. To prevent temperature variations and to obtain uniform atmospheric conditions, the nominal orbit will be sun-synchronous to the plane of the earth's terminator — a dawn-to-dusk orbit.

The data from this mission will provide an updated quantitative global map of the earth's vector magnetic field. This data will be used to revise the regional magnetic charts used for navigation and other purposes throughout the world.

In addition, the data will indicate the presence of magnetic anomalies in the earth's crust. When correlated with geological and geophysical models of the crust, this information can indicate potential targets for natural resource exploration.

The overall accuracy requirements desired for the vector magnetometer instrument are high. Not only must the instrument measure the vector field with an absolute error per axis of 5 γ and an alignment stability of 5 seconds of arc, but the orientation of the instrument with respect to the earth must also be precisely known. Because an instrument with such accuracy and alignment stability has never been flown, the present study was undertaken under a contract from NASA-GSFC to establish the feasibility of such an instrument. The contract required the development of a design approach to the problem of precise measurement of vector field aboard a low-altitude, earth-orbiting satellite, with analytical verification that the design approach developed is capable of meeting the requirements of the specification. Consideration of the problem of calibrating the instrument was also part of the specified effort.

The tasks actually performed in the study are indicated in Table 1-2. A substantial effort was devoted to the problem of selecting the most promising sensor configuration from the standpoint of alignment stability. Once this configuration was selected, a specific structural and thermal design for the sensor was developed and analyzed.

The need for high accuracy and stability imposes severe requirements on the magnetometer electronics. Most of the study was devoted to the problem of accurate measurement and digitization of the signals produced by the magnetometer.

Calibration and alignment of the magnetometer to the required accuracy poses a difficult problem. One can establish the location of an optical reference with second-of-arc accuracy, but it is not as easy to find the direction of a reference magnetic field that accurately. This problem was also studied, with emphasis on the actual experimental situation and the method of reducing the data to obtain the most reliable scale factor and alignment calibration.

The study produced a feasible design approach, as well as a number of definite conclusions and some recommendations for the development of the flight magnetometer and for extensions of the study to resolve some problem areas uncovered. A summary of the design approach is presented next.

TABLE 1-1. OBJECTIVES OF THE MAGSAT MISSION

- Provide updated global magnetic field maps.
- Locate magnetic anomalies in the earth's crust.

TABLE 1-2. TASKS PERFORMED IN THE VECTOR MAGNETOMETER STUDY

The purpose of the study was to establish the feasibility of a flight vector magnetometer with an absolute accuracy of 5γ and an alignment stability of 5 seconds of arc.

Task	Scope
• Sensor Configuration	- Establish the sensor configuration least sensitive to misalignment errors.
• Sensor Design	- Select a specific sensor design approach and confirm its performance by analysis.
• Electronics	- Select a specific electronics configuration and verify its performance by analysis.
• Calibration	- Develop a plan for calibrating the magnetometer to the required accuracy.

DESCRIPTION OF THE DESIGN APPROACH

The Vector Magnetometer design studied uses a triaxial fluxgate sensor assembly with triaxial vector feedback to eliminate the effects of fluxgate misalignment. The fluxgate electronics has been specifically designed for superior stability using currently available technology.

The requirements for the Vector Magnetometer for MAGSAT are among the most stringent ever conceived. During the study we selected a design and demonstrated by analysis that it exceeds the requirements — in most cases — by substantial margins. The principal features of this design are listed opposite and summarized below.

Principal Features of the Design - To eliminate the effect of sensor misalignments, three orthogonal ring-core fluxgate sensors are operated within a coil system which provides a triaxial vector feedback field that cancels the earth's field, so that the sensors operate in a null-sensing mode. When this is done, the alignment of the system depends almost solely on the alignment of the feedback coils and not on the alignment of the sensor elements, which are difficult to make dimensionally stable. Also, the sensors contribute only to the offset and noise of the system and not to instabilities in the overall gain. This approach was used on the Pioneer 10/11 Vector Helium Magnetometer.

An exploded view of the sensor is shown in the figure opposite. The feedback coils are constructed on spherical graphite-epoxy forms, which provide high structural rigidity and thermal conductivity. Analysis of this construction shows that all alignment and stability requirements can be met with substantial margins.

An external set of coils provides essentially complete cancellation of the external field (to 0.02γ at 60 cm from the center of the sensor).

The sensor housing is made almost entirely of non-conducting materials to eliminate thermo-electric currents. The sensor assembly is thermally insulated and operated at very low power, to control self-heating effects. The multiple-layer thermal shield consists of insulating layers and a shunt conductive layer to conduct heat to the temperature-controlled baseplate. Active temperature control of the baseplate using an ac-driven printed-circuit heater reduces internal gradients.

The electronic design follows a conventional arrangement. The fluxgate cores are excited by a tuned drive circuit to provide high excitation with low drive losses. The second harmonic signal from the sensor is filtered and amplified, synchronously demodulated, and further amplified to provide a dc voltage. This voltage is converted to a current which is fed back to the triaxial coils. The circuits are implemented using modern operational amplifiers to provide the required stability. The critical current feedback components must be thermally stabilized.

Conversion of the dc voltage to a digital signal to be telemetered may be accomplished by either a single-range 17-Bit ADC or a multiple-range 12-Bit ADC with an offset field generator. Only the detailed design of this latter approach however was investigated.

Performance - In the course of the study, we performed an analysis of this design based on a detailed error allocation. Our analysis shows that the MAGSAT requirements can be exceeded by the proposed design, in most cases by substantial margins. The discussion of the specification compliance, presented next, indicates in detail the level of performance that could be achieved.

TABLE 1-3. PRINCIPAL DESIGN FEATURES

Feature	Advantage
• Triaxial Vector Feedback	- Eliminates effects of sensor misalignment.
• Rigid Spherical Feedback Coil Forms	- Provides high thermal and structural stability.
• Multiple Thermal Shield	- Very low internal temperature gradients.
• Active Temperature Control	- Ensures fixed-temperature operation.
• Current Source Temperature Control	- Ensures gain stability and linearity.
• Dual-slope Integrating ADC	- Eliminates zero offset errors.

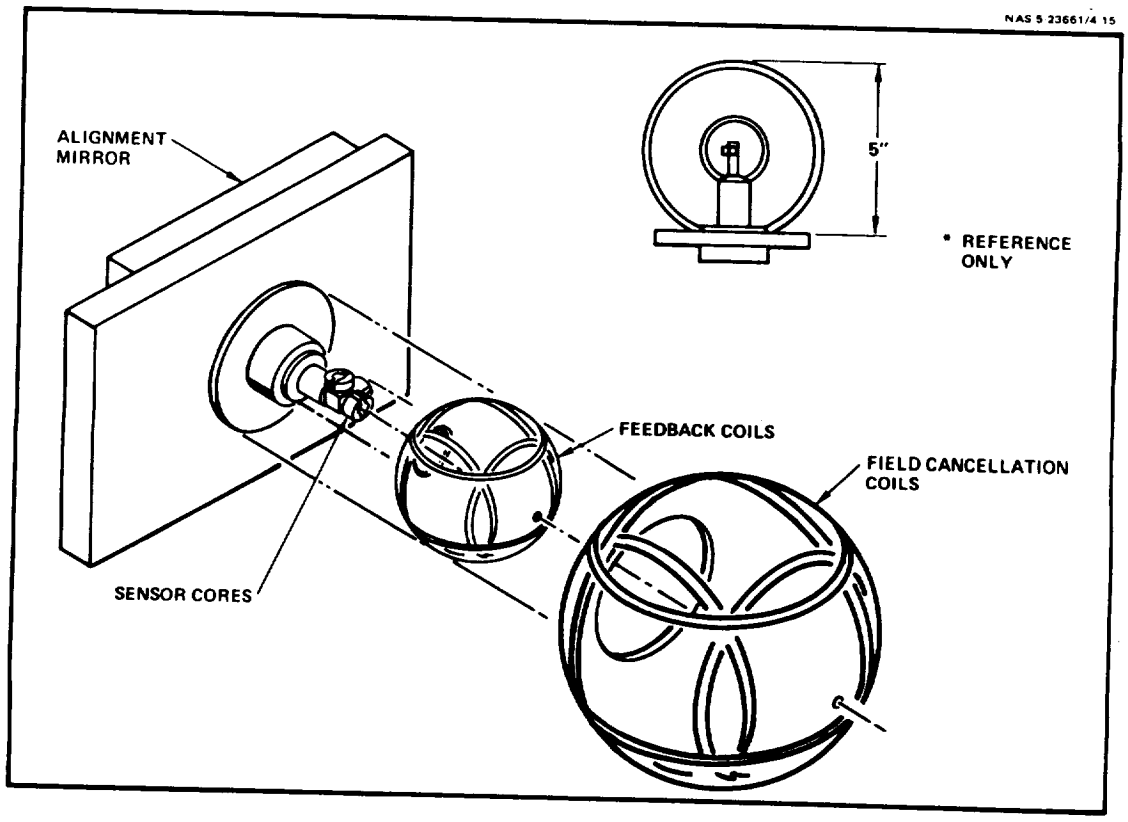

Figure 1-1. Exploded View of the Sensor. Triaxial feedback is provided by coils mounted on rigid thermally stable spherical forms.

COMPLIANCE WITH STUDY CONTRACT SPECIFICATION

The design approach was selected after an optimization analysis. Analysis of the performance shows that it will meet or exceed the specified performance, within the specified weight, power, and environmental constraints.

The contract for the present study specified the performance requirements of the Vector Magnetometer, and required that the performance of any design approach be confirmed by analysis.

Performance Requirements - The specified orthogonality and offset requirements are all similar to those of magnetometers we and others have built and flown before, and we see no difficulty in meeting them.

The noise requirement can be met, but we found that the peak noise requirement in the specification is unnecessarily stringent in view of the fact that the specified quantizing error is ten times larger. With the agreement of NASA technical personnel, we adopted a modified noise specification – the highest noise we thought was acceptable. By doing this, we provided higher design margins for meeting the critical requirements for absolute accuracy and alignment stability. A compromise design with lower noise would make the sensor larger and impact the weight.

Selecting an Approach to Exceed the Requirements - Our approach to the study has been to exceed the MAGSAT requirements rather than merely come close to them. We knew when we started the study that the use of triaxial feedback would enable us to have a good chance of meeting the alignment stability requirements, but we did not expect to be able to exceed them by a large margin. In fact, in our analysis of the triaxial feedback design, we have been unable to identify an error which we cannot control by design to well within the specification. The analysis is presented in the body of the report.

The analysis presented does not consist only of a detailed analysis of the specific design which was studied. To select the design approach and narrow down the range of possible design characteristics, we performed tradeoff analyses to show that the approach selected was actually the best approach, or very near to it.

The principal features of the design which meets these specifications have already been described. In Table 1-4 we have identified those design features which enable us to meet each requirement.

Analysis of Performance - As explained previously, our ability to exceed these requirements is a direct consequence of two design features – the use of triaxial feedback and the fabrication of spherical feedback coil forms and other structural components from graphite-epoxy materials. These materials provide the required high rigidity and high thermal conductivity, but yet are light in weight and do not appear to exhibit any significant thermoelectric effect.

The analysis which we have performed has put us in position to make a number of specific recommendations, which are treated in the following pages.

TABLE 1-4 COMPLIANCE WITH STUDY CONTRACT SPECIFICATION

	Required Performance	Estimated Performance
Zero Offset		
Sensor		0.3
Electronics		0.37
RSS Total	0.4γ	0.47
Noise		
Sensor		0.35
Electronics		0.01
RSS Total	1.0γ	0.35γ
Scale Factor		
Sensor		0.06
Electronics		1.1
RSS Total	4.1γ	1.1γ
Sensor Alignment	2.5 arc sec	0.6 arc sec
External Field	0.5γ	0.01γ

A complete error budget appears on Page 2-7. More detailed error breakdowns can be found on Page 4-51 for the sensor assembly and on Page 5-13 for the electronics.

PRINCIPAL CONCLUSIONS OF THE STUDY

The vector magnetometer should employ triaxial vector feedback to reduce misalignment sensitivity. By use of a strong feedback coil structure made from isotropic, stable material, and by use of suitable thermal shielding, the stability and alignment of the sensor can be made to exceed requirements. Either a single-range analog-to-digital converter (ADC) system or one with multiple offset ranges will provide the electronics stability required.

While the noise and offset requirements for the magnetometer have been met many times before, the scale factor and alignment stability and calibration are the most stringent ever required. The principal conclusions reached in our study of how these requirements can be attained are listed opposite.

The scale factor stability of the magnetometer is determined by the stability of the sensor feedback coils and the feedback electronics. The alignment can depend not only on the alignment of the feedback coil, but also on the difficult-to-control alignment of the magnetic sensor itself.

Sensor Design Study: The Need for Triaxial Vector Feedback - The recommended design approach employs fluxgate sensors because they are simple and meet the noise requirements. To attain the required scale factor stability and linearity, these sensors must be enclosed in an overall magnetic feedback loop, cancelling the earth's field with a feedback coil around the sensor so that the sensor operates in a null mode. Then, only the sensor noise and offset matter. In our analysis, we found that the sensitivity of the overall alignment to misalignment of the sensors themselves — in contrast to the feedback coils — could almost be eliminated by nulling all three components of the vector field at each sensor. Mathematically, this finding relates to the fact that the orientation of a null vector (of zero length) need not be specified. Thus, our specific design approach consists of a system in which three orthogonal sensors are surrounded by three orthogonal feedback coils.

In investigating this system, we found that the external field can be cancelled almost exactly (to $< 0.02\ \gamma$ at 60 cm) by use of external cancellation coils. By careful selection of the coil geometry and the use of a simple, rigid structure using isotropic graphite-epoxy materials, as well as by providing thermal shielding, we were able to obtain an estimated scale factor and alignment stability of 1.5γ and <5 seconds of arc, respectively. The weight and power requirements of the sensor are low: 1.82 kg and 300 mW, the power being almost entirely that of the thermal control heater. The feedback coil and sensor drive power is only 35 mW maximum.

Electronic Design Study - Because low sensor power input is required for thermal stability of the sensor housing, a reactive drive scheme is needed to eliminate the losses produced by conventional current or voltage drive methods. Except for the use of this technique (to be flown on MJS) the sensor drive and ac signal handling circuits can be conventional. The important problem is the design of the feedback system and the ADC. The study found that either a single-range ADC or a limited-range ADC with several offset ranges could meet the requirements; the design approach studied in detail was based on the multiple-range configuration.

To achieve the necessary stability of the feedback coil current, it is necessary to control the temperature of the feedback current source to $\pm 5^{\circ}C$.

Calibration Study - The study concluded that the absolute determination of the scale factor and alignment of the instrument is very difficult. The verification of axis and scale factor stability is much less difficult. There appears to be no difficulty in principle in determining the orientation of the magnetometer housing to the order of one second of arc by optical means. However, the real problem is to determine the actual physical orientation of the sensor magnetic axes. This cannot be done without knowledge of the absolute orientation of the calibration field — not of the field-producing coils, but the field itself. Only the relative orientation of the coils at the GSFC facility is known, and that only to about 10 seconds of arc. If this facility is to be used, it will have to be upgraded.

TABLE 1-5. CONCLUSION OF VECTOR MAGNETOMETER STUDY

Conclusions of Sensor Design Study

- Triaxial feedback is needed to reduce the misalignment sensitivity.
- Large external coils are needed to attain a low external field with low power and good field uniformity.
- Only a small coil structure is needed (less than allowed envelope) even if only two coils are used.
- By using spherical coil forms made with graphite-epoxy material, we can get a field stable to 1.5γ and <5 seconds of arc.
- Use sensor temperature control to $\pm 1^{\circ}C$.
- Require electronics temperature control to $\pm 5^{\circ}C$.

Conclusions of Electronics Design Study

- Reactive sensor drive required to reduce sensor dissipation.
- Either a single-range or multiple-offset-range ADC will work.
- Electronics temperature control required ($\pm 5^{\circ}C$).

Conclusion of Calibration Study

- Principal problem is absolute calibration.
- Upgrading of GSFC calibration facility is required.

RECOMMENDATIONS FOR HARDWARE DEVELOPMENT AND FURTHER STUDY

The flight instrument should definitely employ a triaxial feedback scheme using a graphite-epoxy structure for stability. The details of the design should be checked by measuring prototype fluxgates and feedback coils. The theory of the fluxgate performance should be developed further, and the calibration problem needs further work.

From the conclusions reached in the study, we have developed definite recommendations for the next steps in the development of the vector magnetometer. Some recommendations relate to the design of the hardware, while others relate to the attainment of better understanding of how to design and test such a device.

Hardware Recommendations - The principal conclusion of the study is that triaxial vector feedback should be used to attain low sensitivity to fluxgate sensor misalignment by using a three-axis coil system surrounding three orthogonal fluxgate sensors. This follows directly from a mathematical analysis of the sensitivity problem. The alternative – the use of three separate single-axis sensors mounted at right angles – does not provide the required low axis alignment sensitivity because the feedback loop for each single-axis sensor is closed in only one direction.

The size and detailed design of the triaxial feedback coils depends upon an engineering analysis in which the size of the fluxgate sensors, and hence the feedback coils, was selected by optimization of the fluxgate and coil dimension to minimize the size and weight while meeting a somewhat relaxed noise specification. Before committing the design to a hardware development phase, the assumptions should be checked by building and testing sensors and coils with the recommended characteristics to verify the analysis.

It is generally agreed, and confirmed by our work, that the structural and thermal stability required can be attained if a graphite-epoxy structure is used. This material has the combination of high rigidity, low thermal expansion, and high thermal conductivity characteristics necessary to provide the required structural and thermal stability. We have recommended the use of an isotropic material with random fiber orientation to avoid thermal distortion caused by anisotropic expansion. The use of this material should be investigated further with the fabrication and test of a prototype structure.

Although the electronics design required is conventional and straightforward, we do recommend that the critical subsystems such as the 17-bit ADC for the single-loop system as well as the DAC, OFG, and Feedback Current Generator for the two-loop system be studied further to verify the flight worthiness of the components used.

Recommendations for Further Study - Other than the excellent metallurgical work reported by NOL, the literature search performed for the study did not uncover any published analyses of the problem of obtaining optimum performance of the sensor – i.e., analyses of the signal-to-noise ratio as opposed to separate calculations of the signal sensitivity or the noise. Consequently, we developed analyses of this area ourselves.

Our analyses of sensor performance contradict some conventionally accepted ideas about fluxgate design (although we understand that results in agreement with our analyses have been obtained experimentally).

Because of their importance to further design work in fluxgate sensors, we recommended that our analyses be extended and published in the open, refereed literature to promote further discussion and investigation in this area.

Finally, study of the calibration problem emphasized a difficulty which was already realized; if one is to calibrate this magnetometer, more accurate facilities are needed to do it. Improvement of the existing facility and procedures is a high-priority problem which should receive prompt attention.

In the body of the report which follows, we first describe the recommended design and then show how the approach was selected and implemented. Analyses are provided to show that the required performance is attained, except for those uses in which the performance follows directly from the manner in which the design requirements are implemented.

TABLE 1-6. HARDWARE DEVELOPMENT RECOMMENDATIONS

- Develop and test prototypes of triaxial feedback fluxgate and feedback coil.
- Fabricate and test graphite-epoxy structure.
- Establish flight worthiness of single-loop and two-loop electronics system components.

TABLE 1-7. FURTHER STUDIES RECOMMENDED

- Extend sensor signal-to-noise ratio analysis.
- Extend calibration study to include plans for upgrading GSFC test facility.

SECTION 2
MAGNETOMETER DESIGN REQUIREMENTS

Review of Vector Magnetometer Performance Requirements 2-2
Components of the Vector Magnetometer 2-4
Allocation of the Errors to Sources 2-6

REVIEW OF VECTOR MAGNETOMETER PERFORMANCE REQUIREMENTS

The Vector Magnetometer for the Applications Explorer Mission (AEM) will be used to obtain a global map of the earth's magnetic field. To provide a significant improvement over existing maps, the magnetometer must be exceedingly stable, and its orientation precisely known.

In the following paragraphs we will discuss briefly the requirements for the Vector Magnetometer. The remainder of this study addresses the problem of how these requirements can be met. The requirements are summarized in the Table.

Need for Accurate Measurements - To make measurements which advance the state of the art it is necessary to measure the earth's field with an overall accuracy of 5Y (1Y = 10^{-9} Tesla). This requirement is difficult because there are a number of error sources which contribute to inaccuracy and because the earth's magnetic field can be as large as 64000Y, so that the required accuracy is better than 1 part in 10^4. The contribution to the inaccuracy from stability in the instrument offset must be less than ±0.4Y over the operating temperature range; the digital resolution must be ±1Y. Of these requirements, the one for offset stability is the most difficult to achieve, since the allowable drift is only six parts in 10^6.

Noise and Bandwidth Considerations - The bandwidth of the instrument is to be 25 Hz, with a capability of limiting the bandwidth to 1 Hz. Over the 25-Hz bandwidth, the noise is specified to be 0.1Y peak for a 10-second scan with a 25-Hz bandwidth (about ±0.038Y rms, or less). It has been agreed that this requirement is unnecessarily stringent in view of the fact that the quantizing error is 1Y peak. For the study, we have adopted the criterion that the peak noise should be at most equal to the peak quantizing error. In addition, the rms noise should be at most 0.38Y.

Physical Characteristics - The total weight of the magnetometer, including the sensor electronics and the signal and power cables in the boom, is to be less than 5 kg. The sensor volume is limited to a 30-cm diameter sphere, while the electronics volume is limited to 4500 cm^3 as shown in the table.

Importance of Alignment Stability - The overall accuracy of the field measurement is affected by the misalignments of the sensor axes. To provide the required accuracy the orientation of the axes must be known with an angular error of less than 78μ radians or 16 seconds of arc; this angular misalignment produces a signal of 5Y along the axis of the magnetometer normal to the full scale 64000-Y field. To measure the orientation of the sensor — mounted on a 3-6 meter flexible boom — an optical attitude determination system will be used. A number of error sources contribute to the total error in determining the attitude of the instrument. The budget for the errors internal to the instrument is shown in the table.

The orientation of sensor axes is to be repeatable over the temperature and environmental range to 5 arc-seconds repeatable. The magnetic axes shall be orthogonal to within ±0.1 degree. This requirement also seems unnecessarily stringent. Even with a maximum inaccuracy of 5Y, one could correct for lack of orthogonality as large as 1 degree with a worst-case error of only ±0.1Y.

The angular alignment between the sensor and the geometric axes of the sensor housing, as well as the alignment between the optical reference and the geometric axes of the housing, must be measurable to 1 arc-second. Since the error can presumably be in either direction, we interpret this specification to mean ±1 arc-second for each of the two error sources, for a worst-case error of ±2 arc-seconds.

External Field Cancellation - Because a scalar magnetometer is mounted nearby, the external field of the Vector Magnetometer must be small. We have adopted a value of 0.5γ at 60 cm (24 inches) from the center of the Vector Magnetometer sensor.

Environmental Constraints - The performance specifications of the magnetometer are to be met before and after exposure to the shock, vibration, and acceleration tests, as well as during exposure to the simulated or actual orbital thermal environment. The details are given in the instrument specification. In the table we have shown the temperature and the maximum accelerations experienced in test.

Meeting these difficult requirements necessitates careful systems analysis of the instrument design. We now proceed to discuss the implications of these requirements for the design of the magnetometer.

TABLE 2-1. PERFORMANCE REQUIREMENTS FOR VECTOR MAGNETIC FIELD MEASUREMENTS

The requirements for accuracy and alignment are particularly stringent.

Measurement	3 orthogonal components of earth's magnetic field
Orbit Characteristics	Near-polar, low altitude (325-550 km) Insolation: 60 min; eclipse 30 min.
Dynamic Range per Axis	±64000γ
Overall Accuracy	±5γ
Offset Stability	±0.4γ
Resolution	±1γ
Bandwidth	25 Hz (limiting to 1 Hz)
Noise	0.1γ peak for 10 second scan, with 25-Hz bandwidth (original specification); 1γ peak or 0.3γ rms (modified specification)
Axis Stability	5 arc-seconds
Axis Orthogonality	90 degrees ±0.1 degree
Axis Determination Accuracy	Sensor Elements to Sensor Axes: ±1 arc-second; Optical Reference to Sensor Axes: ±1 arc-second
External Field	0.5γ at 60 cm (24 inches)
Boom Characteristics	3-6 meter extensible
Total Weight	5 kg
Sensor Volume	30-cm diameter sphere
Electronics Volume	20 cm x 15 cm x 15 cm
Power Consumption	6 W
Temperature	Storage: -50°C to +85°C Thermal Shock: -50°C to +85°C Electronics Operating: -10°C to +50°C
Acceleration	Sinusoidal Vibration: 20 g (36-158 Hz) Random Vibration: 12.9 g-rms (200-400 Hz) Thrust Acceleration: 22.5 g

COMPONENTS OF THE VECTOR MAGNETOMETER

A vector fluxgate magnetometer has three separate sensor channels, one for each axis. The characteristics of the sensor, signal electronics, feedback circuits, and digitizing circuits must be appropriately selected to meet the overall performance requirements.

To design the Vector Magnetometer, it is necessary to translate the overall performance requirements just described into design requirements for each component of the magnetometer.

The requirements for MAGSAT can be met by use of either a vector helium or a three-axis fluxgate magnetometer. The vector helium magnetometer provides better low-frequency noise performance at the cost of greater complexity; because this particular low-noise characteristic is not needed for the MAGSAT application, a fluxgate magnetometer has been selected for study. The components which typically make up a fluxgate magnetometer are shown opposite, for one of three sensor channels; the central power supply, sequencing logic, and other housekeeping and support systems are not shown.

How the Fluxgate Operates - The fluxgate sensor consists of a magnetic core consisting of either a pair of long rods or a tape-wound toroid of a high permeability square-loop core material. It is driven into saturation at a high audio frequency (typically 10 kHz) by current in a drive winding. In the presence of an external field, an even-harmonic flux change is generated in the core as a result of a variation in the saturation time of the different parts of the core. This signal is amplified, synchronously demodulated, filtered, and fed back as a current input to a feedback coil which produces a field to null the external field. The sensor then functions only as a null-sensing device and does not have to meet high linearity or gain stability requirements. The signal which drives the feedback coil is digitized to provide the output data which is a number directly related to the value of the external field.

To implement the block diagram shown, it is necessary to decide on the organization and performance characteristics for each block.

Organization of the Feedback Arrangement - The field along each axis of the magnetometer is measured by a separate sensor with separate electronics as shown. Often, the sensors for each axis are physically separated, and use one coil both to sense the signal and to provide feedback to cancel one component of the applied field. Alternatively, a set of orthogonal coils can be used to null the field over an entire volume occupied by three sensors. In either case, the three sensor electronics channels function independently and have the same block diagram; but it is necessary to select the feedback arrangement which provides the best performance.

Organization of the Digitizing System - For some applications the dynamic range of the applied field is very large. For MAGSAT, the ratio of the total field variation to the quantizing interval is 128000Y/1Y, or slightly less than 2^{17}. Covering such a wide dynamic range with one analog-to-digital converter can be avoided by using a sampling conversion within the feedback loop or by offsetting the feedback current by a switched constant current to optimize the overall digitizer performance. The selection of the appropriate digitizing scheme is another question to be decided.

In addition to these two organizational questions (considered in detail in the remainder of this report), one must specify the performance requirements for each component of the magnetometer. This allocation of errors

can be done by identifying and specifying the error contributed by each component or each block in the block diagram. We now describe the allocation adopted for the present study.

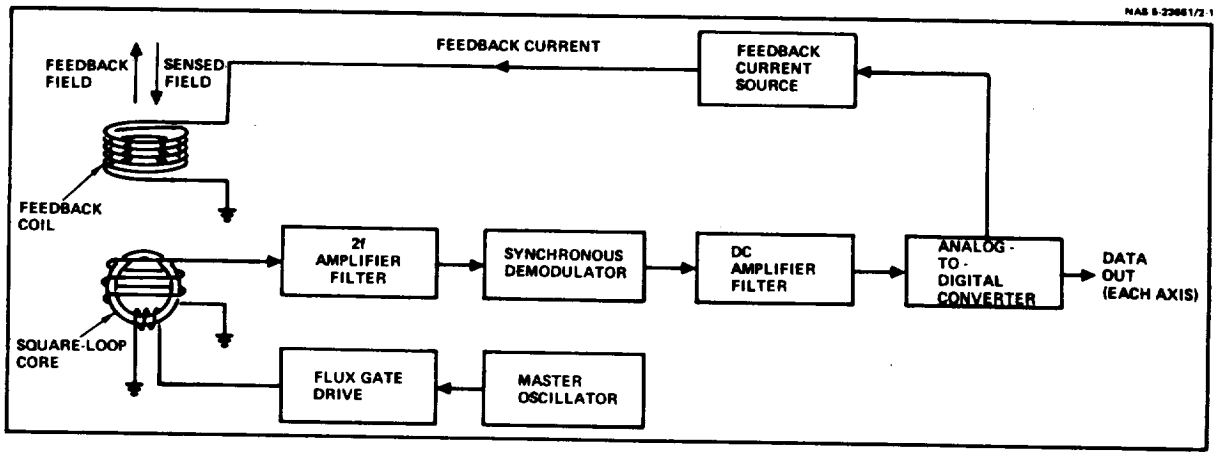

Figure 2-1. Block Diagram for One Axis of a Vector Magnetometer. Each of the three orthogonal sensors has the same block diagram. The feedback coils and the digitizing system may each be organized in several different ways.

ALLOCATION OF THE ERRORS TO SOURCES

A detailed error budget has been generated to control the design. Worst-case errors have been allocated to each error source, adding the effects of the separate errors by the root-square-sum method.

As indicated in the discussion on meeting the performance requirements, there are a number of error sources which contribute to each specified tolerance. To control our design, we have generated the error budget shown on the facing page. Because there are many error sources contributing, we have distributed the errors using the root-square-sum methods, taking the square root of the sum of the squares of the independent worst-case errors to arrive at the overall tolerance.

We now indicate briefly the rationale behind the allocation shown.

Absolute Accuracy - The specification allows an overall error from all sources of $\pm 5\gamma$ for each axis. The most significant sources of error that attribute to this are, scale factor drift, non-linearity, and misalignment of the sensor. For these we have allowed the largest sensor budgets. In addition to these measurement errors result from offset uncertainity, noise, and quantization. We estimate the RSS total resulting from these to be $\pm 4.7\gamma$. Several of the above errors originate in both the sensor and the electronics. These are discussed below.

Scale Factor - The contributions to the scale factor error attached to the sensor and the electronics are 1.5γ and 2.5γ for short term instability and 2.5γ for the long term drift of the electronics. Some of the sources causing this error are variations in the feedback coil constant; current source transimpedance, fluxgate translation error, forward loop amplification variations and feedback coil impedance variations.

Linearity - The sources of non-linearities are primarily within the sensor. Therefore of the allowed 1.5γ, most has been allotted to the sensor. Only 0.1γ has been allowed to errors caused by forward loop amplification waveforms.

Zero Offset - There are many factors that contribute to the offset error. Some of these are sensor magnetostrictive, current source amplifiers, drive harmonics and supply voltage variations. However these are controllable, therefore, only $\pm 0.4\gamma$ has been allotted, with $\pm 0.33\gamma$ being attributable to the electronics and $\pm 0.2\gamma$ to the sensor. Both for short term enviromental stabilities and long term drifts.

Given the allocation of allowable errors to the various sources in the sensor and the electronics we, now turn to a discussion of the overall magnetometer systems design.

TABLE 2-2 DESIGN ERROR BUDGET FOR THE VECTOR MAGNETOMETER

Absolute Accuracy	Error	Field Error (±γ)
Offset Uncertainty	±0.4γ	0.4
Offset Long Term Drift	±0.4γ	0.4
Scale Factor Drift	50 PPM	3.0
Scale Factor Long Term		2.5
Non-Linearity	50 PPM	1.5
Misalignment	5 arc-sec.	1.5
Noise	±1.0γ	1.0
Quantization Error	±1.0γ	1.0
RSS Total		4.7

Zero Offset	Instability (±γ)	Aging(±γ/year)
Sensor	0.20	0.20
Electronics	0.33	0.33
RSS Total	0.39	0.39

Scale Factor	Instability (±γ)	Aging (±γ)
Sensor Scale Factor	1.5	--
Electronics Scale Factor	2.5	2.5
	2.9	2.5

Non-Linearity	Instability (±γ)
Sensor Heating	1.5
Electronics	0.1
	1.5

SECTION 3
MAGNETOMETER SYSTEMS DESIGN

Meeting the Performance Requirements 3-2
Functional Description of the System Design 3-4
Physical and Interface Characteristics for the Recommended Sensor Design 3-6

MEETING THE PERFORMANCE REQUIREMENTS

The performance requirements can be met by the use of sensor feedback and thermally stable feedback circuits and coils. Both sensor and electronics will require temperature control; low thermal gradients in the sensor can be attained by use of superinsulation and low coil power.

Magnetometers with offset and noise performance equal to that required have been previously flown, but the requirements for absolute accuracy and alignment present new problems. The following qualitative discussion indicates what design approaches are necessary to meet the performance requirements.

Gain Stability and Linearity - The accurate measurement of the field along each axis of the magnetometer requires very high gain and offset stability and linearity. To achieve the required gain stability and linearity, the magnetic field sensors (of whatever kind) must be enclosed in feedback coils so that the sensor operates only as a null detector. Since the field produced by a coil is a function of its size, thermal expansion of the coil becomes a critical matter, requiring temperature control of the sensors as well as the use of thermally stable materials. To generate the feedback field, the feedback coils must be driven by a precision current source whose output impedance is much higher than the unstable coil impedance. The overall loop gain must be high.

Offset Stability - The attainment of the required offset stability requires low offsets in the sensor, the ac drive and signal circuits, the dc feedback system, and the analog-to-digital converter (ADC). Fluxgate sensors with offset stabilities and noise performance comparable to these required have been built by Time-Zero Laboratories and others using core materials with low magnetostriction. The recommended sensors use the 6-81.3 Mo-Permalloy recommended by the Naval Ordnance Laboratory. The electronic offsets arise from several sources, namely, generation of second harmonic signals in the drive circuit and signal amplifiers, and dc offsets in the demodulator-filter, current source, and ADC. These can be controlled by the precautions indicated in the table.

Axis Stability - Attainment of the required axis stability requires stability of the sensor mounting structure and internal orientation. To achieve such stability, the sensor subsystem must be kept at a constant temperature and must be designed for low thermal gradients in the structure, which in turn implies minimum power input to the sensor. To avoid thermoelectric or induced currents, the sensor housing must be made of relatively non-conducting materials which possess sufficient thermal stability to stay in alignment in spite of the internal thermal gradients produced by the sensor. Finally, it is important to arrange the feedback so that the alignment depends only on the feedback coil geometry. The conventional single-axis fluxgate sensor is feedback-stabilized along only one axis. Motion of the sensitive magnetic element normal to this axis produces a first-order misalignment error for fields normal to the feedback axis, even if the orientation of the feedback and pickup coil is stable.

This difficulty can be circumvented by enclosing all three sensors in a single volume in which the vector field is nulled, rather than nulling the three components separately at different locations. The only critical assembly is now the feedback coil structure — which is less critical than for a single-axis system because there are fewer parameters to be controlled and the structural and thermal design is easier. The external field

is larger, but very low external fields can be attained by the use of correction coils.

Stability of the sensor alone is of no use unless the location of the axes can be determined both in flight and during calibration. The transfer between the sensor coordinate system and the coordinate system of the optical reference mirrors must be stable as well, implying the use of a thermal design which minimizes thermal gradients.

Axis Determination - To calibrate the axis determination system, it is necessary to produce a magnetic field whose direction is known with the required accuracy. This problem is as difficult as the design of the sensor, but the facilities are to be made available at the Goddard Space Flight Center. It seems clear the final calibration should be done with the actual optical system to be used in flight, so there will be no inaccuracies resulting from cross-calibrations.

This discussion indicates that special care must be taken in designing the sensor structure and in assuring that the sensor is stable in the range of flight environments to be expected. The offset requirements are similar to those of instruments previously flown; the gain and alignment stability requirements are stringent but within the state-of-the-art. It is clear that unusual attention must be paid to the accuracy and to the experimental details of the calibration procedure.

TABLE 3-1. HOW THE PERFORMANCE REQUIREMENTS CAN BE MET

Each performance requirement leads to a number of critical design requirements.

• Scale factor stability and linearity	- Sensor feedback and sensor temperature control - Thermally stable feedback coils - Low sensor power input - Precision feedback current source - High feedback source impedance - High loop gain - Accurate ADC scale factor
• Offset stability	- Low magnetostriction fluxgate cores - High symmetry core drive - Narrowband second harmonic filters - High gain, linear AC amplifiers - Low offset current source - Low offset ADC
• Axis stability	- Triaxial feedback - Constant sensor temperature (1°C) - Low thermal gradients (1°C) - Minimum sensor power - Stable graphite-fiber materials - Stable optical reference
• Axis determination	- Optical access to sensor reference surface - Precision calibration system

FUNCTIONAL DESCRIPTION OF THE SYSTEM DESIGN

The vector magnetometer design consists of three orthogonal fluxgate sensors mounted inside triaxial feedback coils. The sensor is enclosed in a housing insulated with a thermal blanket; active temperature control is accomplished with a printed circuit heater. A conventional one-loop system or two-loop system with an offset generator may be employed for the electronics subsystem.

The design presented here is a result of analysis of the sensor and electronics design. The principal design decisions and their rationale are indicated in the table opposite, while the figure shows how the system is implemented.

Sensor Arrangement - As explained previously, it is necessary to enclose the sensor coils in the triaxial feedback coils to eliminate effects of sensor misalignment. This approach results in a true vector instrument. The alignment stability then depends almost entirely on the stability of the feedback coils. Analysis shows that the feedback coils can be built with the required stability. An extra set of coils is used to cancel the external field.

Alignment - The alignment of the sensor will be measured by use of an alignment mirror or other optical alignment surface mounted on the sensor base plate.

Thermal Control System - It is exceedingly important to inhibit gradients within the sensor assembly to avoid thermal expansion and distortions. To attain this uniformity, the sensor is insulated from the sun and from the cold of space by use of two multilayer super-insulated thermal blankets, separated by a graphite-epoxy housing which acts as a thermal shunt to the controlled baseplate.

Electronics - The circuitry required is conventional. The second harmonic signal from each fluxgate sensor is amplified by a tuned amplifier, synchronously demodulated, amplified and filtered. The amplified, filtered output is used to drive the feedback coil and is also converted to a digital signal in an ADC. An offset field generator (OFG) supplies discrete steps of additional feedback as determined by its logic controller. The entire process operates synchronously with signals from the spacecraft.

The critical problems in the design of this system are the mechanical and thermal design of the sensor and the design of the stable feedback system.

TABLE 3-2. MAIN FEATURES OF VECTOR MAGNETOMETER DESIGN

Feature	Rationale
Fluxgate sensor	- Low power, weight, volume
Triaxial feedback	- Insensitive to fluxgate alignment
Switched offset generator	- Stable offset over dynamic range
Spherical housing	- Reduced thermal radiation
Thermal blankets	- Reduced effect of insolation and radiative cooling
Printed Circuit Heater	- Distributed to reduce gradients from mirror heat losses

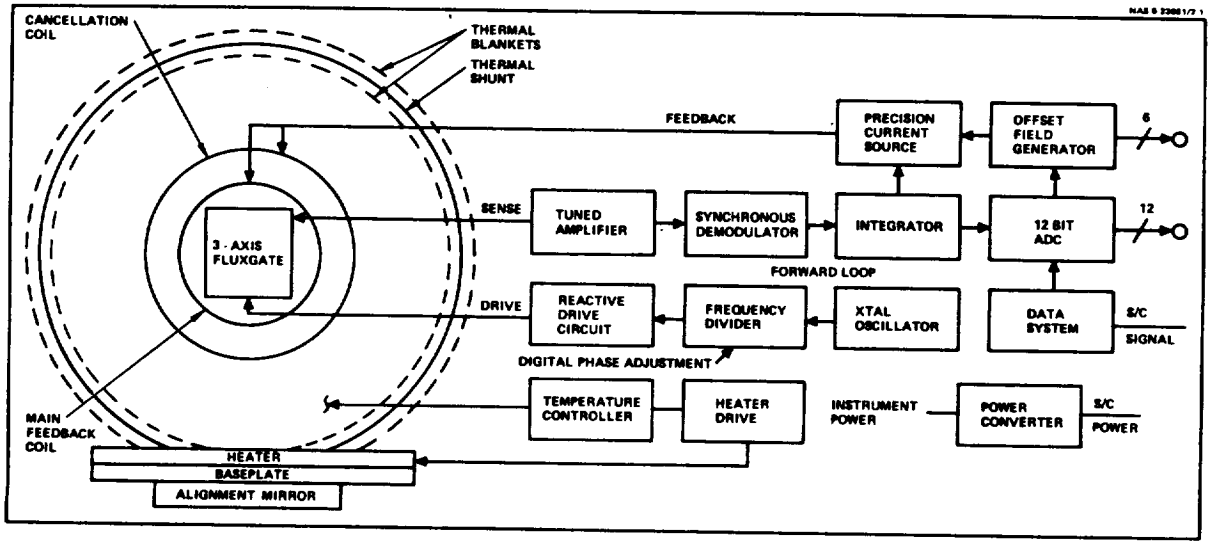

Figure 3-1. Block Diagram for Vector Magnetometer. Electronics for one of the three channels of a two-loop system are shown.

PHYSICAL AND INTERFACE CHARACTERISTICS FOR THE RECOMMENDED SENSOR DESIGN

The recommended triaxial feedback sensor is located at the end of a boom in a thermal enclosure mounted on a thermally shielded base plate carrying the alignment mirrors. The electronics package is mounted in the spacecraft and communicates with the sensor by means of a boom cable. The weight and power requirements are less than specified.

Here we briefly summarize the physical and interface characteristics of the design. The vector magnetometer sensor has been designed under the assumption that it will be carried on the same boom as a scaler magnetometer sensor mounted not closer than 24 inches away (center-to-center).

The envelope, weight, and power consumption characteristics are summarized in the table opposite. In general, we have tried to achieve the minimum weight by making the sensor as small as possible consistent with meeting the modified noise specification. (The noise determines the size because bigger fluxgate sensors have lower noise, and the size of the sensors directly impacts the size of the feedback coils and surrounding structural and thermal shield.) The power is kept as low as possible, and the solar heating has been reduced by use of a low-absorptive finish. This approach not only reduces gradients but minimizes the difference between the solar insolation and eclipse conditions. The heater size has been chosen to compensate for the losses through the superinsulations and from the surface of the alignment mirrors.

Electronics - The electronics characteristics are also tabulated. It appears that the electronics will fit in a housing approximately 15 cm x 13 cm x 8 cm, weighing 1.02 kg. Four printed wiring assemblies are required, including the power supply and logic required for sequencing. These numbers are estimates since a detailed electronics packing design was not attempted. The estimates are based on component counts and should be quite close.

Boom Cable - The recommended triaxial feedback scheme requires separate feedback and sensor coils, so that the number of wires per sensor axis is six, including the drive (three shielded pairs). In addition, a pair of heater sensor leads and a pair of power leads are required. A total of 22 wires, minimum, is required for the vector magnetometer.

Command Interface - Commands will be required to place the instrument in a calibration mode and to provide self-test modes for the ADC. These commanded modes and their operation were not considered in the study.

TABLE 3-3. OVERALL WEIGHT AND POWER

	Specified	Actual
Total Weight	5 kg	3.53 kg
Total Power	6 W	5.2 W
Sensor Characteristics		
• Envelope	20 cm dia sphere	
• Weight	1.82 kg	
• Heater Power	165 mW	
• Sensor Power	35 mW	
• Thermal Finish	- White on sun side - Gold or white on space side	
• Thermal Shield	- Gold kapton except over alignment mirrors – 200 mW peak	
Electronics Characteristics		
• Envelope	15 cm x 13 cm x 8 cm	
• Weight	1.02 kg	
• Power (total instrument)	5 W	
Boom Cabling Requirements		
• Total number of wires	22	
• Wire size	30 AWG shielded	

SECTION 4
SENSOR DESIGN

4.1 - CONFIGURATION ANALYSIS

Summary of Optimum Sensor Configuration Analysis 4-2

Dependence of Sensor and Feedback Configurations on Misalignment Sensitivity 4-4

Factors Influencing Magnetometer Alignment Stability 4-6

Calculation of the Misalignment Sensitivity of a Single-Axis Magnetometer 4-8

Use of Triaxial Feedback to Reduce Sensor Misalignment Sensitivity 4-10

Uniformity Requirements for the Triaxial Feedback Field..... 4-12

Dependence of Noise and Offset on Fluxgate Dimensions 4-14

Optimization of Fluxgate Geometry Under the Noise and Size Constraints 4-16

Finding the Simplest Arrangement for Generating a Uniform Feedback Field 4-18

Magnetic Field of Coil Pairs 4-20

Cancellation of the External Field..... 4-22

Modifying the Feedback Coil Spacing to Minimize Coil Size 4-24

Derivation of Structural Stability Requirements 4-26

4.2 - SENSOR DESIGN AND PERFORMANCE ANALYSIS

Design of the Sensor for High Stability 4-28

Detailed Design of the Fluxgate Sensors..... 4-30

Magnetic Configuration of the Feedback Coils 4-32

Electrical Design of the Feedback Coils 4-34

Mechanical and Thermal Design of the Sensor Assembly..... 4-36

Analysis of Structural Stability 4-38

Strategy for Controlling Thermal Effects 4-40

Analysis of Self-Heating Effects 4-42

Design of the Thermal Control System 4-44

Design of the Thermal Controller 4-46

Performance of the Thermal Shielding..... 4-48

Estimates of Sensor Stability 4-50

SUMMARY OF OPTIMUM SENSOR CONFIGURATION ANALYSIS

To meet the alignment stability requirement in an optimum way, the sensor should employ triaxial vector feedback. Helmholtz coil pairs produce adequate field uniformity, especially if the coil spacing is slightly modified. A concentric larger set of Helmholtz coils will provide almost complete cancellation of the external field.

Before plunging into the details of a specific sensor design and performance analysis, we will present the analysis which led to the selection of the design. In the following pages, the rationale for a design optimized for alignment stability is fully developed; here, we summarize the analysis briefly.

Selection of Feedback Configuration - To provide the required stability and linearity, the fluxgate sensors used must be used in the null mode. The earth's field is cancelled by a feedback field produced by coils whose coil constant and alignment must be stable. There are at least two ways to organize the feedback. Each orthogonal fluxgate sensor can have its own feedback coil — a single-axis system — or three fluxgates can be located inside three orthogonal feedback coils which provide a vector feedback field. We call this system triaxial feedback.

The analysis presented in this subsection shows that the sensitivity to misalignment of the fluxgate sensors is far less if triaxial feedback is used, not only because the feedback loop is closed in all three dimensions for each sensor, but also because of a simpler mechanical configuration. Because alignment stability is the most critical requirement for the MAGSAT Vector Magnetometer, the triaxial feedback system was selected.

Fluxgate Sensor Configuration - The noise of a fluxgate sensor depends on its size and shape; the sensors can be designed to attain a specified noise level. Accordingly, we have selected a sensor size which is compatible with a modified noise level requirement of 1γ peak, selecting the diameter-to-height ratio to give a minimum package size for the three orthogonal sensors mounted at the center of the triaxial feedback field.

Feedback Coil Configuration - The three sensors cannot be all at exactly the same place in the feedback field. The field therefore must meet certain uniformity requirements so that errors do not arise from instabilities of the sensor position or orientation.

Attainment of a sufficiently uniform field is simply a matter of using an appropriate number of feedback coils. The problem is to attain adequate uniformity with coils of minimum size, weight and complexity. In principle, the use of many coils allows the use of very small coils; but, in practice, the mechanical design to avoid interferences between coils prevents the coil system from being very small. Analysis shows that adequate field uniformity is attained with a single pair of coils per axis, with a coil spacing slightly less than their radius (modified Helmholtz configuration).

Cancellation of External Field - Because the leading term in the external field is a dipole field, the external field can be greatly reduced by cancelling the dipole moment of the main feedback coils with an outer pair of coils. Because Helmholtz coils have no quadrupole field, the outer coils should also be Helmholtz coils. Less power is required if the coils are large — at least twice the size of the inner coils.

Modification of the Field - A pair of Helmholtz coils with a spacing equal to their radius produces a field flat on the axis midway between the coils. Because the fluxgate sensors are offset from this central position, it would be better if the field were flat at the sensor. The radial position of the flat spot can be put at the offset sensor position by pushing the coils together slightly. Doing this allows the use of minimum-size feedback coils.

Structural and Thermal Design Requirements - From the equation for the field, one can obtain the sensitivity of the field to various dimensional changes. The values of the sensitivity parameters have been derived to specify the tolerances required in the structural and thermal design.

These matters are treated in detail in the following pages of this subsection.

TABLE 4-1. SENSOR CONFIGURATION ANALYSIS SUMMARY

The optimum configuration of the sensor was selected according to the rationale indicated.

Selection	Rationale
• Triaxial feedback	- Low misalignment sensitivity. - Structural advantages.
• Specific fluxgate size	- To meet noise requirement.
• Helmholtz inner feedback coil pair	- Adequate uniformity. - No external quadrupole moment.
• Large outer Helmholtz Cancellation coils	- Cancel dipole moment of inner coils. - Low power. - No external quadrupole moment.
• Modified Spacing of Helmholtz coils	- Make field flat at sensor. - Minimize required coil size.

DEPENDENCE OF SENSOR AND FEEDBACK CONFIGURATIONS ON MISALIGNMENT SENSITIVITY

To select the most promising sensor configuration for the Vector Magnetometer, it is necessary to use one of the three fluxgate geometries — parallel-rod, racetrack, or ring-core — in a feedback coil system which assures low sensitivity to sensor misalignment.

Fluxgate Sensor Characteristics - The fluxgate sensor is a remarkable device, capable of measurement of magnetic fields over a very wide dynamic range. Fluxgates have been flown to the moon and to all of the inner planets and Jupiter, and a fluxgate instrument is now en route to Saturn on Pioneer 11. Others will fly on the MJS (Mars-Jupiter-Saturn) spacecraft.

The fluxgate is basically a transformer with a square loop core so that it acts as a magnetic amplifier. The flux is made to saturate alternately in each direction by an alternating current in an ac drive winding. In the presence of an external field, a flux change at twice the drive frequency is generated in the core. This flux change can be detected by a sense winding and amplified to obtain a measure of the applied field. The sense winding is wound differentially to reject the drive; in practice, this means that the sense winding is simply wrapped around the core. The noise is essentially Barkhausen noise, while the offset appears to be produced by magnetostriction. The two effects are related: materials with low magnetostriction have low noise as well. The theory of the signal generation, noise, and offset is discussed in detail in Appendix A.

Several different core configurations are possible — a pair of straight rods, an elongated (racetrack) toroid, or a cylindrical ring core. Historically, the racetrack sensor evolved from the parallel rod sensor, while the ring core evolved from the magnetic amplifier, being simpler to manufacture because of its cylindrical shape. The principle of operation is the same for all three. Selection of the fluxgate geometry depends on the characteristics of the feedback coil system.

Feedback Characteristics - The important aspect of the sensor design approach is not so much the selection of the type of fluxgate to be used, but the way the fluxgate is used in an overall feedback loop. Feedback must be used to generate a magnetic field which nulls the ambient field to attain the required linearity and insensitivity to misalignment error. In this manner the sensor is used only as a null detector, so that the stability of its gain and linearity are not important. Such feedback is commonly used in flight magnetometers for precision measurements.

To minimize the effects of sensor misalignment, it is important to organize this feedback in the proper way. Historically, vector magnetometers have often been made by placing three single-axis fluxgates — either parallel-rod, racetrack, or ring-core — at right angles, with a separate feedback coil for each sensor, as shown in Figure 4-1. The Pioneer 10/11 Vector Helium Magnetometer, built for JPL by Time-Zero, is an exception: since the helium-gas sensor is inherently a vector device, the feedback was accomplished by a set of three Helmholtz coil pairs which produced a vector feedback field (see Figure 4-2). Ring cores appear to be the best kind of fluxgate sensor for this triaxial configuration because they allow a more compact structure, making it easier to produce a feedback field uniform over the sensor volume.

Misalignment Sensitivity - Comparing Figures 4-1 and 4-2, one might expect the single-axis and triaxial-feedback arrangements to have different sensitivities to sensor and structural misalignment. For example, the single-axis sensors are mounted apart from one another on an extended structure to avoid sensor crosstalk, while in the triaxial geometry the sensors can be mounted in a compact assembly. Because of the stringency of the alignment requirement, the configuration which has the lowest sensitivity to misalignment errors must be selected for MAGSAT. The selection of the most promising geometry thus requires an analysis of the misalignment sensitivity of each configuration. This analysis, which leads to the conclusion that the triaxial configuration is far less sensitive to misalignment error, is reported in the following topics.

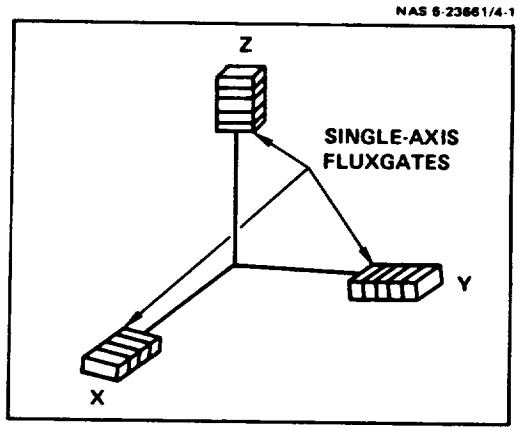

Figure 4-1. Single-Axis Vector Magnetometer Each fluxgate sensor is surrounded by an independent feedback coil which nulls one component of the ambient field. A vector field in an arbitrary direction is not nulled.

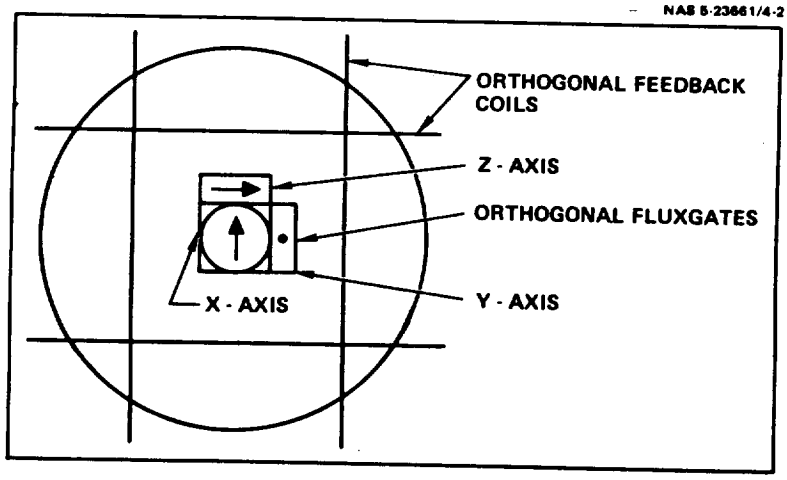

Figure 4-2. Triaxial-Feedback Vector Magnetometer. Three orthogonal fluxgate sensors are mounted within a triaxial coil structure which completely nulls the ambient field in the neighborhood of the sensors. Ring cores are preferred for symmetry.

FACTORS INFLUENCING MAGNETOMETER ALIGNMENT STABILITY

The vector magnetometer is sensitive to misalignments of the optical mount and sensor structure, feedback coils, and the sensitive magnetic cores.

To understand the alignment problem completely, it is necessary to understand how the instrument data must be reduced. The alignment as well as the calibration of the vector magnetometer is ultimately specified by giving the 9 components of a 3 x 3 matrix G^{-1} such that $\vec{B} = G^{-1}(\vec{N} - \vec{N}_o)$, where N is a vector whose components are the digitized output of the three signal channels, and $\vec{B}$ is the measured field relative to the coordinates of the optical attitude determination system. The vector $\vec{N}_o$ is the offset. The scale factor matrix depends not only on the orthogonality and scale factors of the individual sensors but also on the stability of the rotation between the sensor axes and the axes of the optical determination system.

Several alignment factors (formally described by rotation matrices) are involved in transferring between the coordinate systems. These factors are identified in the accompanying table and are discussed below.

Optical Reference Mount Alignment - The mirrors used by the optical reference system mount on a plane surface facing the spacecraft. This plane surface is part of the structure which also supports the sensor assembly. No matter what sensor arrangement is used, this structure must be rigid – for example, it must not deflect in the earth's gravitational field as a result of its own weight or that of the sensors, thermal shielding, or mirrors.

Sensor Structure Alignment - The structure on which the sensor feedback coils themselves are mounted must be structurally and thermally stable, because this structure defines the relationship between the sensor axes and the axes defined by the mirrors and their mounting plate. For a single-axis system, the sensors are well-separated so that the fields of their independent feedback coils do not interact. For such an arrangement, the stability of the intervening structure is particularly critical. For the triaxial arrangement, the sensors are closer together, but the feedback coil system is larger, so that close attention is required to make the mechanical and thermal feedback coil structure rigid. The structural rigidity requirement appears to be easier to meet for the highly symmetrical triaxial arrangement compared to the extended rod or plate structures used for single-axis magnetometers we know about.

Feedback Coil Alignment - The orientation of the feedback coils is evidently critical for either sensor geometry. The coils, which are wound on forms and potted, must be designed to maintain the required alignment stability relative to the mounting structure. To achieve a stability of 5 seconds of arc requires a mechanical stability of 25 microinches per inch. This is of the same order as the stability required of precision optical systems. It appears easier to define the coil orientation in the triaxial arrangement, because it is larger; if the structure is rigid, a small motion of the effective coil axis leads to a relatively smaller angular misalignment than does the same linear motion of the relatively small feedback coil used in the single-axis sensors.

Guaranteeing the relative alignment of the optical reference and feedback coils is a matter of adequate structural and thermal design, no matter what feedback configuration is adopted; this design problem is treated in a later section. The selection of the feedback configuration, which does have a major influence on the effects of magnetic core misalignment, is discussed in this subsection.

Magnetic Core Alignment - The actual magnetic sensing element is the magnetic core. If it moves relative to the feedback coil axis, there will in general be an error in the measured field, because the field sensed is not equal to the null field produced by the feedback coil. The single-axis system is quite sensitive to this effect, while the triaxial system is not, because all three components of the field are nulled instead of only one. This difference makes the single-axis system far more sensitive to core misalignment, as is shown in the next topic.

TABLE 4-2. ALIGNMENT STABILITY FACTORS

- Optical Reference Mount
  - must be rigid
- Sensor Structure
  - must be structurally and thermally stable
- Feedback Coil
  - must have mechanical stability of 25 microinches per inch
- Magnetic Core
  - must be relatively insensitive to core movement

CALCULATION OF THE MISALIGNMENT SENSITIVITY OF A SINGLE-AXIS MAGNETOMETER

The single-axis fluxgate sensor is sensitive to misalignment of both the magnetic core and the feedback coil.

One way to construct a vector magnetometer is to use three separate single-axis sensors at right angles. Consideration of this approach shows that the overall misalignment sensitivity is not determined only by the misalignment sensitivity of the feedback coil, as one might hope. The alignment of the fluxgate core itself is also an important factor and is, in fact, extremely critical.

Simplified Argument - To see that there is a problem with the single-axis sensor, consider the following simple example. Suppose a single-axis fluxgate is located inside a feedback coil. Suppose that the feedback coil produces a field precisely along the nominal magnetic axis, so that the feedback coil is not misaligned. Now suppose that the magnetic core itself is misaligned by an angle Δ in the x-y plane, and suppose that a field B_y is applied along the y axis, normal to the nominal magnetic axis. This field will have a component $B_y \sin \Delta$ along the magnetic axis. To null the field, the feedback loop will force the feedback coil to produce a field of strength $B \sec \Delta \sin \Delta$. This field appears as an error in the measurement of the x-component of the field. Thus, the feedback loop does not correct for magnetic core misalignments.

Complete Analysis - We can readily extend this analysis to include the effects of finite loop gain and feedback coil misalignment. The scalar field measured by the sensor (that is, the sensor output signal) is

$$B_S = \vec{R}_S \cdot (\vec{B} + \vec{B}_F) \tag{1}$$

where $\vec{R}_S$ is a unit vector along the actual magnetic axis, $\vec{B}$ is the ambient field to be measured, and $\vec{B}_F$ is the feedback field. Offsets are neglected (not relevant to the argument).

The feedback field is determined by the loop equation:

$$\vec{B}_F = -\vec{R}_F M B_S \tag{2}$$

The vector $\vec{R}_F$ is a unit vector in the direction of the field produced by the feedback coil, while M is the loop gain. The telemetered field is a scalar variable for each sensor axis; it has the value

$$B_T = M B_S \tag{3}$$

and is assumed to correspond to the component of the ambient field along the nominal direction specified by the unit vector $\vec{R}_N$.

We can now compute the deviation between the telemetered field component and the actual nominal value,

$$B_N = \vec{R}_N \cdot \vec{B} \tag{4}$$

Eliminate B_F from Equation (1) by use of Equation (2):

$$B_S = \vec{R}_S \cdot (\vec{B} - \vec{R}_F M B_S) \tag{5}$$

This leads to the result

$$B_S = \frac{\vec{R}_S \cdot \vec{B}}{1 + M(\vec{R}_S \cdot \vec{R}_F)} \tag{6}$$

The error in the telemetered component is then

$$\Delta B_T = \frac{[M\vec{R}_S - M(\vec{R}_S \cdot R_F)\vec{R}_N] \cdot \vec{B}}{1 + M(\vec{R}_S \cdot \vec{R}_F)} \tag{7}$$

This is the complete formula, showing the effect of finite loop gain and both sensor and feedback coil misalignment.

In the case in which $\vec{R}_F = \vec{R}_N$ (feedback coil aligned), while $\vec{R}$ is not parallel to the nominal axis $\vec{R}_N$, there is an error proportional to $[\vec{R}_S/(\vec{R}_S \cdot \vec{R}_N)] \cdot \vec{B}$. We can plug in the assumptions of the simple example above, by assuming $\vec{B} = \vec{B}_y$, $\vec{R}_y$, $\vec{R}_S = \vec{R}_x \cos\Delta + \vec{R}_y \sin\Delta$, $\vec{R}_N = \vec{R}_x$; the resulting error for infinite loop gain is, as before, $\vec{B}_y \sin\Delta \sec\Delta$.

Example - The accompanying figure shows the arrangement of a typical fluxgate sensor (ring core or racetrack — the problem is the same). The permalloy tape is mounted on the bobbin without excessive constraints to avoid stress-induced offsets. A motion of this tape by only 5 seconds of arc, or 25 microinches per inch, is enough to equal the error allowed for MAGSAT. This amounts to 0.12 μm/inch or 1200 Å — an optical tolerance exceedingly difficult to meet in an electrical device which is essentially a transformer whose core is concealed by windings.

The single-axis magnetometer thus does not benefit very much from the use of feedback, as far as core misalignment errors are concerned (it benefits greatly, of course, in linearity and stability). We can correct for these errors by using the sensors in a manner which closes the loop in all dimensions so that the sensor acts as a true null sensor.

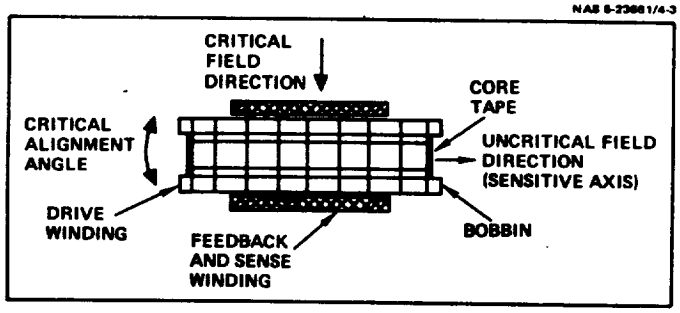

Figure 4-3. Typical Fluxgate Sensor. A motion of only 5 seconds of arc (25 microradians) of tape, bobbin, or feedback coil is sufficient to produce all the error allowable. Rotations about the sensitive axis are also equally critical for either the ring-core or racetrack sensor.

USE OF TRIAXIAL FEEDBACK TO REDUCE SENSOR MISALIGNMENT SENSITIVITY

By using a triaxial sensor within a triaxial feedback coil, the sensitivity to sensor misalignments is greatly reduced, so that the triaxial geometry is the best choice for the MAGSAT Vector Magnetometer.

The basic problem with the single-axis sensor is the fact that it has no feedback for field components perpendicular to its axis. It seems intuitively obvious that this difficulty can be corrected by use of a three dimensional feedback field, using three orthogonal sensors. This supposition is readily confirmed by analysis.

Consider now a vector equation for the three sensor outputs

$$\vec{B}_S = R_S(\vec{B} + \vec{B}_F) \tag{1}$$

As before, B is the ambient field and B_F is the feedback field, but R_S is now a 3 x 3 matrix (an orthogonal rotation matrix if all three sensor scale factors are equal).

As before, the feedback field is determined by an equation of the form

$$\vec{B}_F = -R_F\, M\, \vec{B}_S \tag{2}$$

except that R_F and M are now 3 x 3 matrices: R_F is an orthogonal rotation matrix, corresponding to the misalignment of the feedback coils, while M is a diagonal matrix, whose diagonal components are the three respective loop gains, which of course may differ somewhat. The telemetered field is

$$\vec{B}_T = M\, \vec{B}_S = -R_F^{-1}\, \vec{B}_F \tag{3}$$

while the error vector is $\vec{\Delta}B = \vec{B}_T - \vec{B}$.

This equation is solved by eliminating $\vec{B}_S$ and $\vec{B}_T$ to obtain the result

$$\vec{B}_T = (1 + M\, R_S R_F)^{-1}\, M\, R_S\, \vec{B} \tag{4}$$

The error in the telemetered field is then given by

$$\vec{\Delta}B = (1 + M\, R_S R_F)^{-1}\, [M\, R_S(1 - R_F) - 1]\, \vec{B} \tag{5}$$

For infinite loop gain along all three axes, the result is

$$\vec{\Delta}B = R_F^{-1}(1 - R_F)\, B = (R_F^{-1} - 1)\, \vec{B} \tag{6}$$

This error is proportional to the differences between the feedback coil rotation matrix and the unit matrix, which means that misalignments of the feedback coil by an angle Δ produce error signals in orthogonal channels of order B sin Δ.

The error is independent of sensor alignment (but not sensor offset and noise, of course). This arrangement then operates like a true feedback system in that only the properties of the feedback element are significant in determining the transfer function of the system.

Example - Suppose that one allows for reasonable, easily-inspected tolerances for the fluxgate sensor shown in the previous discussion. One can readily control the tape angular alignment to 1 milliradian or 200 seconds of arc — a tolerance 40 times less stringent than that for the single-axis sensor. Thus, it takes a feedback factor, M, of 40 or more to bring the effect of a worst-case misalignment within specification. However, a much larger feedback factor, on the order of 20,000, is needed to ensure linearity and gain stability, so that the result of using triaxial feedback is to make alignment of the fluxgate itself totally uncritical.

Summary - The analysis just presented has shown that:

- There is a serious problem in making stable fluxgate sensors for single axis system.
- This problem can be eliminated by using triaxial feedback — that is, by enclosing the sensors in a three-dimensional feedback field.

Naturally, the alignment and stability of the feedback coil structure itself is still critical, but this problem is not new — the single-axis system has the same problem.

Selection of Sensor Configuration - The analysis that has been presented shows that the MAGSAT Vector Magnetometer should employ triaxial feedback to reduce the sensitivity to fluxgate sensor misalignment. There are some minor new problems resulting from the fact that the sensors are not all at the same point, so that the field uniformity requirements are somewhat more stringent. But, as will be shown in the next topic, these problems are readily solved.

TABLE 4-3. HOW TRIAXIAL FEEDBACK REDUCES MISALIGNMENT SENSITIVITY

The mathematics in the text expresses the following physical facts:

- Each sensor responds to fields along its own axis.
- Each sensor produces a feedback field to null that axial field.
- This nulls the total (vector) field, even if sensors are not orthogonal.
- Since the total field is zero, its alignment is irrelevant.
- Therefore, the sensor misalignment is irrelevant to the first order of approximation.

UNIFORMITY REQUIREMENTS FOR THE TRIAXIAL FEEDBACK FIELD

Non-uniformity of the field and the physical separation of the sensors lead to a gain correction which must be held stable. For variations in sensor position and orientation of 0.001 inch and 0.001 radian, the feedback field must be flat to about 5 parts in 10^3 to reduce errors to the 0.5 γ level.

In actual practice, the three sensors enclosed in the triaxial feedback volume have finite dimension, so that the places at which they measure the field are different. If the feedback field is not uniform, the field measured by the sensors will not be the same. The sketch opposite shows the geometry. The three fluxgate ring-core sensors are mounted orthogonally inside the feedback coils. The arrows show the sensitive directions. The z-axis sensor is offset in the x direction, and so on in cyclic order.

We can see how this complication affects the analysis in the previous topic by adding a term in Equation (1) to represent an offset in the feedback field. Equation (1) of the previous topic now reads

$$\vec{B}_S = R_S(\vec{B} + \vec{B}_F + R_O\vec{B}_F) \tag{1A}$$

The added term involving the matrix R_O accounts for the difference between the feedback field at the center of the feedback coils and the average field sensed by each sensor.

Following through the analysis as before, we now obtain the following equation in place of Equation (6) of the previous topic

$$\Delta\vec{B} = \left(R_F^{-1} - R_O^{-1}\right)\vec{B} \tag{6A}$$

There is now a correction to the output proportional to the field, so that the added term $-R_O^{-1}B$ represents a gain or alignment variation from the ideal situation.

Translational Error - Instability of the sensor position in a non-uniform feedback field leads to an error which appears as a variation in the coil constant and hence the closed-loop scale factor. In keeping with a total error budget of 1.5 γ, we assign 0.5 γ to this error. The instability of the feedback field must be less than

$$\frac{\Delta B}{B} = 0.5\gamma/64{,}000\gamma = 7.8 \text{ ppm} \tag{7}$$

Referring to the accompanying figure, we see that the critical direction of motion for each sensor is along the direction of the offset (x-direction for the z-axis sensor). Motion along the other axes is far less critical by symmetry (the field has an extremum). We expect to be able to hold tolerances of 0.001 inch worst-case; therefore, the field should have a gradient of at most 8 ppm/mil.

Orientation Error - A field along the x axis is cancelled by feedback action at the location of the x sensor. Because of field non-uniformity there is a small residual field ΔB_x at the y and z sensors; the error in the measured z-axis field produced by a misalignment of the z-axis sensor by an angle $\Delta\theta$ is then

$$\Delta B_z = \Delta B_x \Delta\theta \tag{8}$$

a result which is, of course, a special case of the general result in Equation (6A). To ensure an overall error less than 5 seconds of arc, we assign a worst-case error of 2.5 seconds of arc to this source, corresponding to a field error of 0.8Y, or 12 ppm compared to 64,000Y. It is easy to hold the sensor orientation stable to 1 milliradian (200 seconds of arc), which requires that the field should vary by less than 1.2% between sensors, or about 770Y.

This analysis is very conservative. Precision single-axis sensors such as those used on MJS (in Project MAGNET) and in earthquake prediction exhibit axis stabilities in the 10-50 arc-second range, a number not good enough for MAGSAT but still consistent with dimensional stability in the 0.0001-inch range. We therefore expect that the actual errors will be smaller than allowed when a field meeting the above uniformity requirements is generated, using triaxial feedback coils compatible with the specific fluxgate sensors used. The determination of the fluxgate sensor configuration is considered next.

TABLE 4-4. REQUIREMENTS FOR FIELD UNIFORMITY

• Change in field resulting from 0.001-inch sensor motion	< 0.78Y
• Difference in axial field between sensors	< 770Y

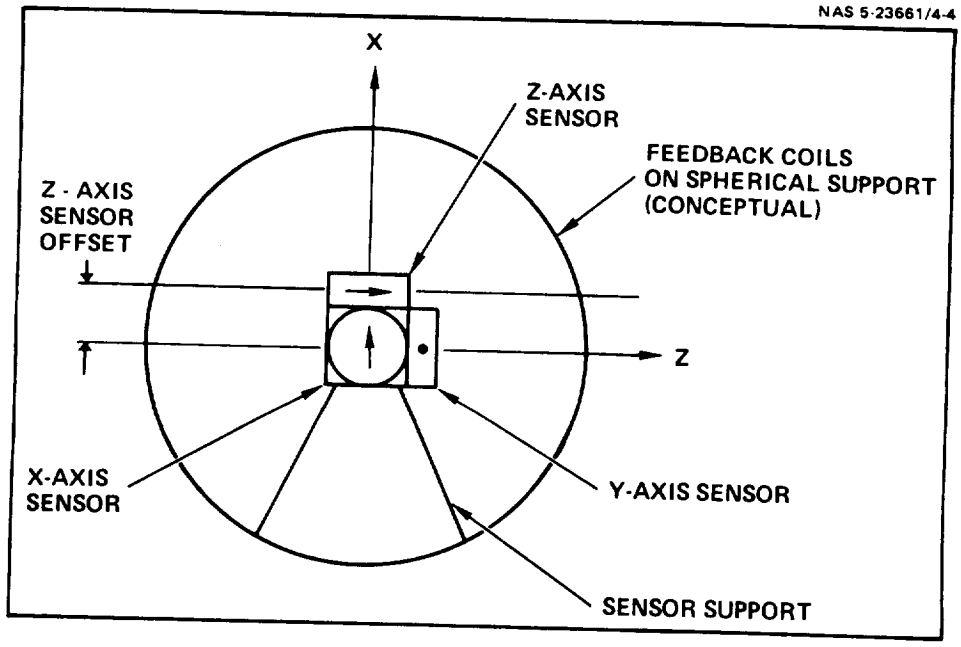

Figure 4-4. Arrangement of Fluxgate Sensors Inside Feedback Coils. The finite separation of the fluxgates leads to the requirements on feedback uniformity given in the text.

DEPENDENCE OF NOISE AND OFFSET ON FLUXGATE DIMENSIONS

The noise and offset of the fluxgate sensors depend on the sensor core dimensions. Larger sensors exhibit better offset and noise performance.

Now that the triaxial-feedback system has been selected, we need to establish the characteristics of the orthogonal fluxgate sensors and the corresponding feedback coils.

To decide how large the uniform-field region must be, we must decide how large the fluxgate sensor array must be. We can do this by relating the physical size of the sensors to the required offset and noise performance using the simplified theory presented in Appendix A, where the dependence of these parameters on the sensor dimensions is derived. The results of this theoretical analysis are summarized briefly here.

Signal Flux and Capture Cross Section - The field inside the iron is related to the field outside by a formula involving the demagnetizing factor, which depends on the geometrical shape of the sensor core. While it is conventional to discuss the behavior of the fluxgate in terms of the demagnetizing factor, this factor is not the relevant figure of merit. What matters is the "capture cross section" — the effective area which multiplies the external field to obtain the sensed flux. The voltage sensed by the pickup winding is proportional to the rate of change of flux in the core. This flux can be expressed as the product of the external (ambient) field and the capture cross section — the effective projected area of the core. For a long thin rod with high permeability, this cross section varies as the square of the rod length and is only very weakly dependent on rod diameter. For a ring-core of finite tape width, the capture cross section is approximately equal to the product of the sensor diameter and tape width, or to the projected area of the tape viewed along the sensitive axis. Thus, the second harmonic signal is essentially determined by the core dimensions.

However, it is not the signal level, but the signal-to-noise ratio — or noise-equivalent field — which matters.

Noise-Equivalent Field - The noise in magnetic amplifiers appears to be produced by domain reversal (Barkhausen noise). The mean-square voltage noise on the second harmonic output is directly proportional to the area of the core and inversely proportional to the effective length of the magnetic circuit. Combining the noise with the sensitivity, one can derive an expression for the noise-equivalent field of a ring-core (Table 4-5). It shows that the noise-equivalent field is proportional to $(t/wd^3)^{1/2}$, where t is the core tape thickness, w is the tape width, and d is the diameter of the ring core.

Offset-Equivalent Field - The offset appears to be produced by magnetostriction, which can be reduced by a proper selection of the core alloy, since permalloys with 81.3% nickel in iron have zero longitudinal magnetostriction. The estimate derived in Appendix A is shown in Table 4-6; the offset-equivalent field varies as t/d, the ratio of the tape thickness to tape diameter.

Both of these estimates assume that the demagnetizing factor for a ring core of finite height can be calculated using an infinite-cylinder approximation. This approximation should be good as long as the core tape width is much greater than the thickness.

Sensor Dimensional Tradeoff - Because the noise depends on both the diameter and width of the core, there is a dimensional tradeoff or

optimization involved when the sensors are required to fit within a specified volume. This optimization is considered in the next topic.

TABLE 4-5. NOISE EQUIVALENT FIELD OF A RING-CORE FLUXGATE

The noise appears to be generated by domain reversal.

$$\Delta B_n = \frac{1}{2}\sqrt{\frac{n_c v_d}{\pi f T}\frac{t}{d^3 w}}\, B_s$$

ΔB_n = noise-equivalent field
B_s = saturation field
n_c = number of elementary dipoles per domain
v_d = domain volume
f = drive frequency
T = signal integration time
t = tape thickness
d = core diameter
w = tape width

TABLE 4-6. OFFSET EQUIVALENT FIELD

The offset is generated by magnetostriction.

$$\Delta B_o = \frac{1}{4}\lambda_s B_s \frac{t}{d}$$

ΔB_o = offset-equivalent field
λ_s = saturation magnetostriction

OPTIMIZATION OF FLUXGATE GEOMETRY UNDER THE NOISE AND SIZE CONSTRAINTS

To minimize the noise-equivalent field with a specified sensor offset, the ring-core tape width should be one-third of the tape diameter. With this shape, one-centimeter diameter sensors should be large enough to meet the noise specification.

To apply the triaxial feedback concept, it is necessary to place three orthogonal fluxgate sensors at the center of a field-free region generated by action of the feedback coils. To simplify the feedback coil design and minimize the overall weight and volume, it is desirable to minimize the sensor size consistent with the noise and offset requirements.

Fluxgate Mounting - The general arrangement of the three orthogonal sensors is shown in the sketch opposite. The field at the location of the sensor will depend mainly on the offset, R, between the center of the fluxgate tape and the center of the feedback field, which is at the center of a cube on which three orthogonal fluxgates are mounted.

The radial offset, R, can be expressed in terms of the diameter and height of the core as well as the buildup in diameter, d_o, and height, w_o, resulting from the finite dimensions of the bobbin and sense winding. (The sense winding can be wound directly on the bobbin to minimize the height buildup w_o.) The radial offset is given by

$$R = \frac{1}{2}(d + d_o + w + w_o) \tag{1}$$

Optimization - The noise equivalent field is inversely proportional to $d^{3/2}w^{1/2}$. To minimize this noise subject to the constraint that the radial offset be constant, we maximize the quantity

$$s^2 = d^3w - \lambda R \tag{2}$$

where λ is a constraint parameter (Lagrange multiplier).

By setting the derivatives of this expression with respect to d and w equal to zero, and eliminating the constraint parameter λ from the two equations which result, one obtains the optimum condition

$$w = \frac{d}{3} \tag{3}$$

For optimum noise performance, the tape width should be one-third of the diameter.

Determination of Core Size - Now that this geometric optimization has been performed, one can estimate the sensor size needed to meet the noise requirement. The MAGSAT study specification requires a 0.1 zero-to-peak noise for a 10-second scan with a 25 Hz bandwidth. But, as discussed earlier, it has been agreed that this specification is unnecessarily stringent. Because the digitizing resolution is 2γ, a peak-to-peak noise of 2γ should be acceptable — a factor of 10 greater than the specified value.

Now, we know that NOL-type one-inch ring cores, with a smaller width-to-diameter ratio, exhibit peak noise levels of better than 0.1γ. Since the noise-equivalent field, by our optimizing constraint, varies as d^2, we should be able to reduce the diameter of the sensor by a factor of $\sqrt{10}$ and still obtain adequate performance. A further safety margin is obtained by using the optimum width. Thus, a core whose diameter is 0.3 inch or greater should provide more than adequate performance.

We have selected a diameter of about 1 cm — actually 0.375 inch, with a tape width of 0.125 inch. We expect that the rms noise will be about 0.1γ.

Offset Performance - Will this sensor exhibit adequate offset stability? The offset drift because the core is smaller will be larger than that of a one-inch NOL sensor. However, the typical sensor exhibits offset stability of a few tenths of a gamma over a very large temperature range, while the MAGSAT Vector Magnetometer Sensor will be temperature-controlled. Offset drift is thus not perceived as a problem.

Now, having selected the appropriate fluxgate size, we need to select the simplest feedback coil configuration which provides the desired feedback field uniformity and yet provides low power and ease of assembly. This selection is discussed in the following topic.

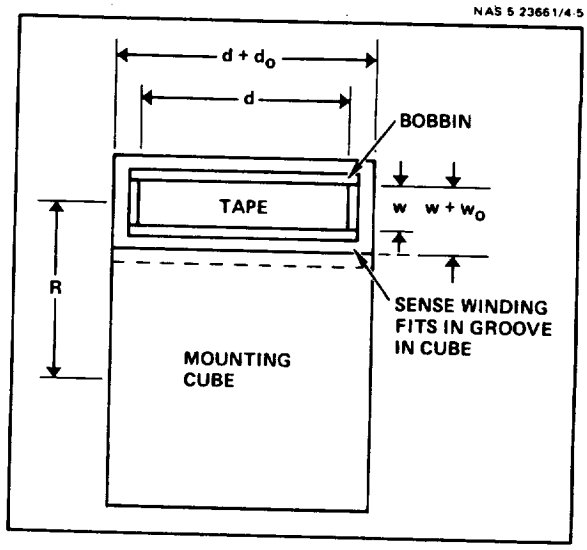

Figure 4-5. Fluxgate Sensor Mounting. To minimize the height buildup, the sense winding is wound directly on the bobbin without a form.

FINDING THE SIMPLEST ARRANGEMENT FOR GENERATING A UNIFORM FEEDBACK FIELD

Because of requirements for structural stability and ease of assembly, the simplest feedback coil configuration which provides acceptable uniformity should be used. A system of Helmholtz coils appears best.

Theoretically a perfectly uniform field can be generated by spacing a large number of windings uniformly along the polar axis of a sphere (or, in fact, a spheroid, either prolate or oblate). Good approximations can be produced by using a finite number of windings ... the more the better, from the standpoint of theoretical uniformity. Yet, there are other requirements. Overkilling the uniformity problem can result in a difficult assembly, with a great many critical windings whose relative alignment must be stable. Then, too, one can show that the uniformly wound sphere requires more drive power than a simpler configuration. A disproportionate amount of coil power is required to assure the ultimate in field uniformity. Minimizing coil power is important to reduce misalignments caused by self-heating, and concomitant thermal expansion of the feedback coils.

Increases in uniformity are attained by increasing the number of windings, spacing them nearly uniformly along the polar axis. The simplest configuration is of course a single coil; the next simplest is a pair of coils separated by their radius (Helmholtz coils). As is shown in elementary textbooks, even this simple configuration already provides a fairly remarkable degree of uniformity, because the first three derivatives of the axial field vanish at the center of the coil system.

The problem with adding more coils is that coils of increasingly smaller diameter are needed near the poles of its sphere. Yet, access along the polar axis is needed to insert the orthogonal fluxgate assembly and to provide a mounting flange of adequate diameter. (See Figure 4. 6.) It is also important to use the minimum number of coils, in view of the need for a simple, rigid structure with a larger number of coils. If many coils are used, the mechanical interferences between coils becomes a real problem; (four coils interfere in 48 places), so that a larger structure must be used to handle the interference problem. One might as well use a simpler configuration of larger diameter to get the same degree of uniformity.

Thus, although the use of four or more coils can theoretically produce a field of spectacular uniformity, mechanical considerations motivate the search for the simplest acceptable coil configuration. The analysis presented subsequently shows that one pair of feedback coils is sufficient to meet the uniformity requirements.

This Helmholtz coil configuration is sketched opposite. Each pair of coils is separated by the mutual radius. While the sketch shows that the coils have the same diameter, the coils for different axes must in fact have slightly different diameters to avoid the mechanical interference between the coils. This complication is neglected in the conceptual discussion which follows but is addressed later.

Another complication is introduced by the need to have a small external field at the scalar magnetometer (0. 5 at 24 inches). If the proposed coil system does not provide the required far-field characteristics it will be necessary to add cancellation coils. The best cancellation system appears to be another set of larger Helmholtz coils, as shown in the Figure.

Having initially selected this design for investigation (for the reasons summarized in the list below) we need to determine the uniformity of the field to see if such a design will produce a sufficiently uniform field with coils of acceptable size, weight, and power. As we shall see, the Helmholtz coil design appears to provide the required performance, especially if the coil separation is adjusted slightly to make the field flatter at the location of the offset sensor.

TABLE 4-7. REASONS FOR DESIRING THE SIMPLEST POSSIBLE CONFIGURATION

- Maximize access to sensor volume.
- Provide strongest possible mounting flange.
- Provide simplest possible structure.
- Reduce coil power.
- Reduce number of critical tolerances.
- Reduce number of mechanical interferences.

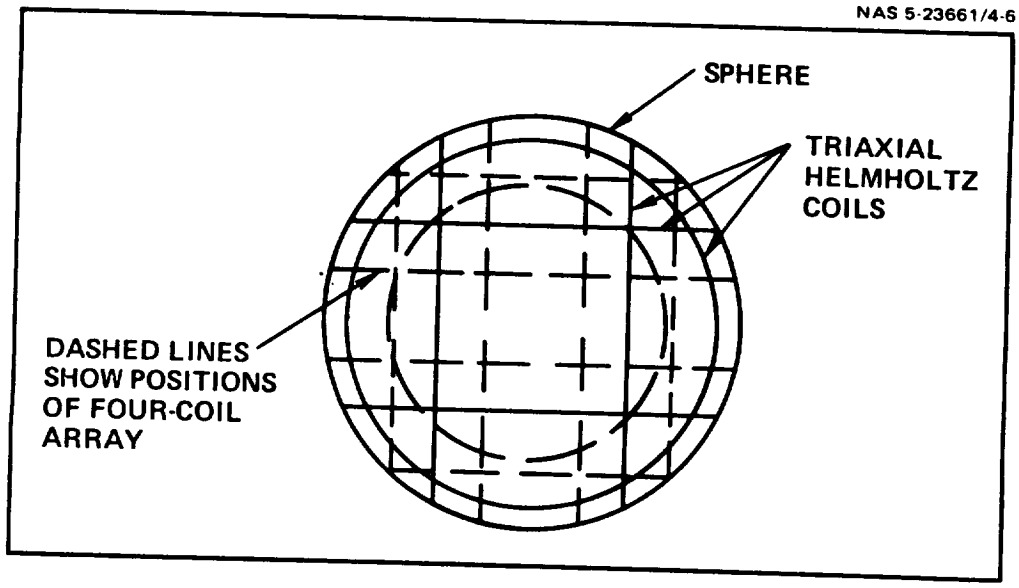

Figure 4-6. Complexity and Access. If many coils are used (the dashed lines show the location of a four-coil array), the mechanical complexity increases and the size of the access port along the coil axis is reduced.

MAGNETIC FIELD OF COIL PAIRS

For purposes of analysis, the magnetic field of a pair of coils can be calculated from a spherical harmonic expansion. If the spacing of the coil is equal to the coil radius, the field between the coils becomes quite uniform.

Having tentatively selected the two-coil Helmholtz configuration for the feedback coils, we must determine the coil size which produces acceptable field uniformity according to the sensor position stability requirements already established. For analytical purposes, the most convenient form for the field seems to be a spherical harmonic expansion. By using this expansion, one can readily estimate the field for coils of small cross section and select the arrangement most likely to work. The selection can then be verified for an actual coil of finite cross section by computing the field directly by numerical quadrature of the integral for the vector field; this procedure is described later.

Spherical Harmonic Expansion for Coil Fields - To keep things simple, we first give the formulas for a single pair of coils. The complication resulting from the addition of cancellation coils will be treated later.

The expressions given opposite are obtained from the single-coil field given by W. R. Smythe (Static and Dynamic Electricity, 3rd edition, McGraw Hill).* All formulas assume the use of SI units, although conventional English units have been used to describe mechanical dimensions. The formulas give the radial and polar components of the field, B_r and B_θ in terms of the field point as shown in Figure 4-7. The coils are symmetrically placed along the polar axis of a sphere of radius a at polar angles α and $\pi - \alpha$, as shown.

The first term in the internal field expansion represents a uniform field along the polar axis (z-direction), which has the radial and polar components $B_r = B_o \cos\theta$, $B_\theta = B_o \sin\theta$. Externally, this term produces a dipole field. The axial field at the center of the coil pair is: $B_o = \mu_o NI/a \sin^2\alpha$ (see footnote), while the external diple moment is: $m = \pi NIa^2 \sin^2\alpha$.

Helmholtz Coils - If we select the coil spacing so that the second term in the expansion vanishes, we have the so-called Helmholtz configuration. The vanishing of the second term requires that $P_3(\cos\alpha) = 1/2(5\cos^2\alpha - 1)\sin\alpha = 0$, or that $\cos\alpha = 1/\sqrt{5}$. The radius of the coils is then $\sin\alpha = a\sqrt{4/5}$; the spacing is equal to the radius.

Since the second term in both the internal and external field expansions vanishes, the Helmholtz coil configuration has an internal field flat to order r^4 at the center of the field, and also no external quadrupole (r^{-5}) field. This fact suggests that cancellation of the dipole moment of an inner pair of coils with an outer pair which are also Helmholtz coils will lead to a very rapid falloff of the external field (as r^{-7}). Thus, larger coils may be used to obtain internal field uniformity and — at the same time — a low external field at the nearby scalar magnetometer.

---

*These formulas can be used to show directly that the field inside a sphere wound uniformly along the polar axis is uniform. The current density of uniformly spaced coils has only one term in a spherical harmonic expansion, proportional to $P_o(\cos\alpha) = 1$. Integrating over this current density leads to a uniform field because all the higher-order turns in the expression to the right drop out because they are orthogonal to $P_o(\cos\alpha)$.

We shall now see how this works and then address the problem of selecting the minimum coil size.

TABLE 4-8. SPHERICAL HARMONIC EXPANSION FOR FIELD OF A COIL PAIR

The field is given in spherical polar coordinates for N turn coils of infinitesimal cross section wound in the azimuthal direction on a sphere of radius a and carrying a current I. The position of the coils along the axis is specified by an angle α (see Figure). The functions $P_n^m(x)$ are associated Legendre functions. The value of μ_o is $4\pi \times 10^{-7}$ H/m.

Field Inside Sphere

$$B_r = \frac{\mu_o NI}{a} \sum_{n=0}^{\infty} \left(\frac{r}{a}\right)^{2n} P^1_{2n+1}(\cos\alpha)\, P_{2n+1}(\cos\theta) \sin\alpha$$

$$B_\theta = -\frac{\mu_o NI}{a} \sum_{n=0}^{\infty} \frac{1}{2n+1} \left(\frac{r}{a}\right)^{2n} P^1_{2n+1}(\cos\alpha)\, P^1_{2n+1}(\cos\theta) \sin\alpha$$

Field Outside Sphere

$$B_r = \frac{\mu_o NI}{a} \sum_{n=0}^{\infty} \left(\frac{a}{r}\right)^{2n+3} P^1_{2n+1}(\cos\alpha)\, P_{2n+1}(\cos\theta) \sin\alpha$$

$$B_\theta = \frac{\mu_o NI}{a} \sum_{n=0}^{\infty} \frac{1}{2n+2} \left(\frac{a}{r}\right)^{2n+3} P^1_{2n+1}(\cos\alpha)\, P^1_{2n+1}(\cos\theta) \sin\alpha$$

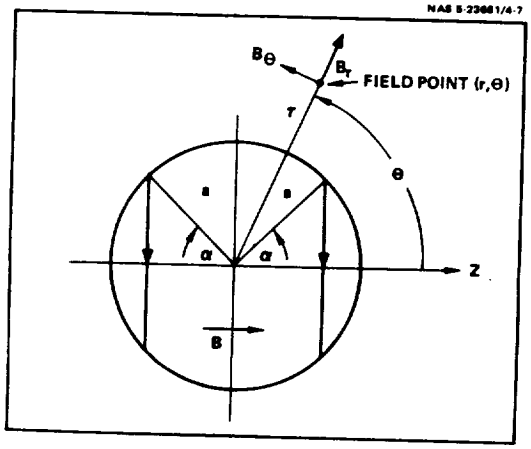

Figure 4-7. Symmetrical Coil Pair. The coils are symmetrically located along the polar axis of a sphere of radius a.

CANCELLATION OF THE EXTERNAL FIELD

Cancelling the dipole field by use of an external pair of coils with twice the radius of the inner pair leads to a very low external field, less than 0.18γ at a distance of 24 inches for eight-inch diameter outer coils, or 0.007 γ for 5-inch coils.

As presently conceived, the MAGSAT has a single boom, which supports a magnetometer mounting shelf carrying a scalar magnetometer as well as the vector magnetometer described in the present study. The external field from the vector magnetometer should not disturb the scalar magnetometer which may be placed close to the vector instrument. Various specifications for the external field have been discussed: we settled on a 0.5 γ requirement at a distance of 24 inches, or 60 cm from the center of the vector magnetometer.

Since the main term in the external field is a dipole term, the obvious thing to do is to provide external coils which cancel the dipole moment of the inner coils. If the inner and outer coils have radii R_1 and R_2 and ampere-turns N_1I_1 and N_1I_2, the dipole moment cancellation requirement is

$$\pi N_1 I_1 R_1^2 = \pi N_2 I_2 R_2^2 \tag{1}$$

The coils are wound so that the fields oppose one another. It is desirable that the coil pairs be connected in series, so that $I_1 = I_2$; then,

$$\frac{N_2}{N_1} = \frac{R_1^2}{R_2^2} \tag{2}$$

The field inside the coils is inversely proportional to the radius. If both coils are Helmholtz,

$$B = \mu_o \left(\frac{4}{5}\right)^{\frac{3}{2}} \left(\frac{N_1 I_1}{R_1} - \frac{N_2 I_2}{R_2}\right) = \mu_o \left(\frac{4}{5}\right)^{\frac{3}{2}} \frac{N_1 I_1}{R_1} \left(1 - \frac{R_1^3}{R_2^3}\right) \tag{3}$$

Thus, even if the ratio of the coil radius R_2/R_1 is only 2, the internal field is only reduced by one-eighth, a reduction easily compensated for by increasing the drive current by the factor 8/7.

Suppose that the external coils have the maximum diameter permitted by the study specification (about 8 inches or 20 cm, allowing something for thermal shielding). Assuming that the inner coils have half that diameter, we can estimate the external field from the next term in the external field expansion. The dipole and quadrupole field are both zero; the octupole field, calculated from the formulas given opposite is only 0.18γ, much less than the 0.5 γ requirement. The external field decreases very rapidly if the coils are made smaller (as the seventh power of the diameter). For the five-inch outer coils actually recommended, the external field at 24 inches is only 0.007γ.

Notice that the dipole moments must cancel to within about 1 percent, since the dipole field of the inner coil is 51.8 γ and the field is to be reduced to 0.5γ. That level of cancellation accuracy is consistent with the required accuracy with which the absolute value of the coil constant must be

controlled. While this cancellation accuracy requirement can be met, it would be easier if the coils and the external field were smaller. Thus, for this reason as well as to minimize the weight and thermal gradients, we wish to make the coils as small as possible consistent with the required uniformity of the inner field. We look into this next.

TABLE 4-9. STRENGTH OF EXTERNAL FIELD FOR HELMHOLTZ COILS

The radial component of the external field along the polar axis is given in terms of the internal field at the center of the coils. The expansion is carried out to order r^{-7} (octupole term). Numerical values apply for four-inch diameter inner coils, eight-inch diameter outer coils, and a 64000 γ central field.

Field of a Single Helmholtz Coil Pair

$$B_r = B_o\left[\frac{a^3}{r^3} - \frac{9}{5}\frac{a^7}{r^7}\right] = B_o\left(\frac{5}{4}\right)^{\frac{3}{2}}\left[\frac{R^3}{r^3} - \frac{45}{16}\frac{R^7}{r^7}\right]$$

Residual Field of Two Helmholtz Coil Pairs of Opposite Dipole Moment

$$B_r = B_o\frac{8}{7}\frac{9}{5}\left[\frac{N_2 a_2^7}{N_1 r^7} - \frac{a_1^7}{r^7}\right] = B_o\frac{45}{14}\frac{R_1^2}{r^2}\left[\frac{R_2^5}{r^5} - \frac{R_1^5}{r^5}\right]$$

Numerical Values for Field at 24 Inches

- Dipole field of uncorrected inner coil 51.8 γ
- Total residual field after correction 0.18 γ

MODIFYING THE FEEDBACK COIL SPACING TO MINIMIZE COIL SIZE

The uniformity of the field at the offset fluxgate sensor can be improved by decreasing the coil spacing, making the axial field flatter at the location of the sensor.

All of the conventional arrangements of coils used to produce uniform fields, including the Helmholtz arrangement, produce the greatest uniformity at the center of the coil system. However, in the triaxial feedback arrangement the sensors must be offset. It makes sense to modify the coil arrangement to flatten the field at the location of the sensor rather than at the center of the coils. Then smaller coils can be used and a lower weight can be attained.

As noted previously, the critical direction for translation is in the direction of the existing sensor offset. In the other directions the sensor is symmetrically located, and translational motions give rise only to very small second-order changes in the average field. Single-axis sensors symmetrically located in fields of much poorer uniformity provide adequate performance with respect to sensor translation, so we expect no problems with motion along the directions in which the field is symmetric. Thus, we wish to make the field more or less symmetric in the offset direction as well.

The actual way in which the sensor responds to the details of the field is very complicated. To solve the problem in detail, it would be necessary to obtain a numerical solution of the magnetic boundary value problem in a non-uniform field — a very respectable exercise in numerical analysis, even if one assumes constant permeability in the sensor. A more practical approach is to adjust the field for a maximum at the center of the sensor for a first approximation and then to optimize the coil separation experimentally to yield zero first-order tolerance to sensor position. The design to be presented has so much margin such that further optimization is probably unnecessary.

We wish first to establish the spacing which provides a suitable extremum in the field at the offset position of the sensor. If the variation of the field averaged over the sensor is then small enough so that sensor motion gives rise to an acceptably small change in the average field, we can expect that the actual performance will also be acceptable.

Field Calculation - To evaluate the variation of the field as a function of coil spacing, it is more convenient to solve for the field directly by numerical integration than to use the spherical harmonic expansion. The axial and radial field components of the field for a single coil are given in cylindrical coordinates (ρ, z) by the integrals opposite (Table 4-11) for a coil of radius a and axial distance z_o. These integrals can be shown to be expressible in terms of elliptic integrals, which have known numerical approximations. For practical purposes it is easier, if somewhat slower, to do the integrals by numerical quadrature. We used Simpson's rule to obtain the plot opposite (Figure 4-8), which shows the radial dependence of the axial field on the central plane for various inner coil spacings with two outer cancellation coils of twice the radius and separation.

From these curves, we can estimate the sensitivity to sensor translation and select the diameter of the inner coils.

To make the coil size selection, we selected one of the curves in the plot, located the sensor on the peak of the field curve, and calculated the corresponding coil radius and location of the sensor tape edges. The

slope of the field at the edge of the sensor is taken as a very conservative measure of the sensitivity to sensor translation.

Following this procedure, one finds that if 2.5-inch diameter coils are wound on a sphere, spaced by 93.5 percent of their radius, the field error per mil of translational sensor motion will be less than 0.7γ. This design is adopted as the study baseline.

Since we have pushed the inner coils together so that the configuration is no longer exactly Helmholtz, the quadrupole moment of the inner coils is now non-zero. In principle, the outer coils can be slightly pushed together also, but by a smaller amount, to compensate for the added field. However, a calculation shows that the added field at 24 inches is only 0.0013γ, so that one might as well leave the outer coils in the Helmholtz configuration.

TABLE 4-10. GENERAL EXPRESSION FOR THE FIELD PRODUCED BY A CURRENT

The following integral must be performed for each current-carrying element of length ds at a distance r from the field output:

$$\vec{B} = \frac{\mu_o}{4\pi} \int I \frac{\vec{ds} \times \vec{r}}{r^3}$$

TABLE 4-11. COMPONENTS OF THE FIELD OF A CIRCULAR COIL

The radial and axial components, B_ρ and B_z, are given in terms of the coil radius a axial position z_o at the field point (ρ, z).

$$B_\rho(\rho, z) = \frac{\mu_o NI}{4\pi} \int_o^{2\pi} \frac{(z - z_o)\, a \cos\varphi}{(a^2 + \rho^2 + (z - z_o)^2 - 2a\rho\cos\varphi)^{3/2}}\, d\varphi$$

$$B_z(\rho, z) = \frac{\mu_o NI}{4\pi} \int_o^{2\pi} \frac{a\,(a - \rho\cos\varphi)}{(a^2 + \rho^2 + (z - z_o)^2 - 2a\rho\cos\varphi)^{3/2}}\, d\varphi$$

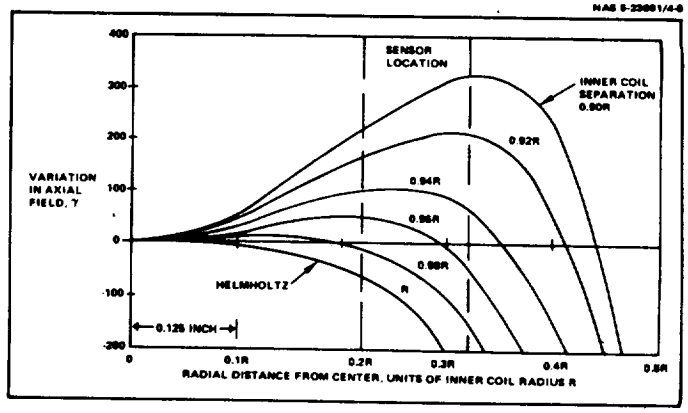

Figure 4-8. Variation in Axial Field for Various Radial Offsets in Central Plane. The field variations apply for a 64000 γ central field. For the sensor position indicated the field can be flattened by using 2.5-inch diameter inner coils separated by 93.5 percent of the radius so that variation of the field resulting from sensor radial motion is negligible.

DERIVATION OF STRUCTURAL STABILITY REQUIREMENTS

The requirements for structural stability follow from the field equations. The most critical parameter is the coil alignment. The dimensional stability required to ensure scale factor stability is equally critical.

To do the structural and thermal design, it is necessary to know the sensitivity of the field to the coil parameters. These sensitivities can be readily calculated from the field equations or from geometrical considerations.

Coil Alignment Stability - Misalignment of the magnetometer can arise from structural or thermal instability of the feedback coil orientations with respect to each other or with respect to the alignment surfaces; the total angular instability from either of these sources is not to exceed 5 seconds of arc. This requirement is very stringent, since it corresponds to a dimensional change of 25 ppm (25 microinches per inch). Note that if one coil of a pair tilts with respect to the other, the net misalignment is half the tilt. Pincushion or other axially symmetric distortion of the coil will cause a scale factor error but not a misalignment.

Scale Factor Stability - The required scale factor stability is equally difficult to attain. On the opposite page (Table 4-12), the central field has been expressed in terms of the diameters and spacings of the inner and outer cancellation coil pairs. By differentiating this formula, one obtains the sensitivity of the central field to changes in the dimensions. For the nominal design in which both the inner and outer cancellation coils are Helmholtz coil pairs, with the outer coils having twice the diameter of the inner coils, the numerical values shown are obtained. The most sensitive parameter is the inner coil spacing, which produces a fractional field variation which is 24/35 the fractional variation in the spacing. The absolute sensitivity is 35Y/mil for a 1. 25-inch spacing. A tolerance of 1. 5Y was assigned to the feedback coil constants in the error allocation presented earlier, or 23 ppm in terms of the 64000Y full-scale field. Assuming that the structure expands uniformly, the overall sensitivity to thermal expansion can be calculated by adding the coefficients opposite algebraically. The result is unity (35/35) so that the regional structural dimensional stability is 23 ppm — about equal to the requirement for alignment stability.

Fluxgate Translation and Orientation - Errors from these sources are controlled by triaxial feedback with proper shaping of the feedback field, as explained in detail previously. The field has been designed to produce acceptable scale factor stability and alignment if the fluxgate position is stable to 0. 001 inch and the orientation is stable to 1 milliradian. These requirements are summarized in Table 4-13. Only the overall requirements are given in the table; the mechanical design must consider other details, since the coil system may very well expand non-uniformly (distort).

TABLE 4-12. SENSITIVITY OF THE FIELD TO DIMENSIONAL VARIATIONS

These formulas give the tolerances which must be met by the structural and thermal design. Numerical values assume both coil pairs have a spacing equal to their radius, and that the outer cancellation coils are twice the diameter of the inner coils.

Expression For the Central Field (SI Units)

$$B = \mu_o N_1 I \left[\frac{d_1^2}{\left(d_1^2 + s_1^2\right)^{3/2}} - \left(\frac{N_2}{N_1}\right) \frac{d_2^2}{\left(d_2^2 + s_2^2\right)^{3/2}} \right] = \frac{\mu_o N_1 I Q}{d_1}$$

Symbols

d_1 = inner coil diameter

s_1 = inner coil spacing

d_2 = outer coil diameter

s_2 = outer coil spacing

(N_2/N_1) = outer/inner coil turns ratio = 0.25

Q = shape factor = $7/8\ (4/5)^{3/2}$

Sensitivity Formulas In Terms Of Central Field

$$\frac{d_1}{B_o}\frac{\partial B}{\partial d_1} = \frac{1}{Q}\frac{2\,d_1^3\left(s_1^2 - \frac{1}{2}d_1^2\right)}{\left(d_1^2 + s_1^2\right)^{5/2}} = \frac{-16}{35}$$

$$\frac{s_1}{B_o}\frac{\partial B}{\partial s_1} = \frac{1}{Q}\frac{s_1}{d_1}\frac{3\,d_1^4\,s_1}{\left(d_1^2 + s_1^2\right)^{5/2}} = \frac{-24}{35}$$

$$\frac{d_2}{B_o}\frac{\partial B}{\partial d_2} = \left(\frac{N_2}{N_1}\right)\frac{d_1}{d_2}\frac{2\,d_2^3\left(s_2^2 - \frac{1}{2}d_2^2\right)}{\left(d_2^2 + s_2^2\right)^{5/2}} = \frac{2}{35}$$

$$\frac{s_2}{B_o}\frac{\partial B}{\partial d_2} = \frac{1}{Q}\left(\frac{N_2}{N_1}\right)\frac{s_2}{d_1}\frac{d_1^2}{d_2^2}\frac{3\,d_2^4\,s_2}{\left(d_2^2 + s_2^2\right)^{5/2}} = \frac{3}{35}$$

TABLE 4-13. DIMENSIONAL TOLERANCES

These are the tolerances on overall dimensional changes. The structural and thermal design must guarantee stability consistent with these values.

• Alignment Stability	~5 ppm
• Scale Factor	~5 ppm
• Sensor Translation	0.001 inch
• Sensor Orientation	0.001 radian

DESIGN OF THE SENSOR FOR HIGH STABILITY

The sensor stability requirements can be exceeded by winding the triaxial-feedback coils on the spherical graphite epoxy forms and by keeping the coil power low enough to reduce the thermal effects.

The design of the sensor depends on a combination of magnetic, thermal, and mechanical factors. After so much analysis it may be helpful to review the overall design approach by way of a summary. As indicated previously, our analysis and that of others shows that high axial stability is much more easily attained if the three fluxgate sensors are enclosed in a single triaxial (vector) feedback field, rather than being enclosed in three separate single-axis feedback solenoids. A detailed analysis of the triaxial feedback scheme and a comparison of triaxial and single axis feedback has been presented. The principal error source in the single-axis system is the instability of alignment of the sensitive core; this sensitivity is reduced by a large factor by triaxial feedback. Other errors, such as the axial instability of the feedback coils, are comparable for either system.

Design of Feedback Coil/Sensor System - If the field inside the triaxial feedback coils were perfectly uniform, the position and orientation of the sensors would be almost irrelevant. We have selected the simplest feedback coil system which produces adequate uniformity for ring-core sensors large enough (3/8 inch, or about 1 cm, in diameter) to meet the noise specification — namely, a Helmholtz coil pair along each axis. A larger pair is used to cancel the external field, as discussed previously and shown in the figure opposite.

The ring-core fluxgate sensors are mounted orthogonally on a cube. They are made as small as possible consistent with meeting the noise specification. Their dimensions were adjusted to minimize the noise-equivalent field subject to the geometric size constraint. The inner feedback coils are pushed together slightly to make the field flat at the sensors rather than at the geometric center of the coils.

Mechanical and Thermal Design of the Sensor Assembly - The primary consideration in the design of the sensor assembly is mechanical and thermal stability of the feedback coils, which is the main factor in determining the gain, linearity, and alignment stability of the instrument. It has been determined that a graphite-fiber epoxy-resin material will provide the required mechanical and thermal stability.

The sensor assembly is composed of a base, a sensor tower, and two spheres of graphite-epoxy on which the coils are wound. In order to achieve thermal stability, a thermal resistance and coil power must be selected that will result in an acceptable thermally induced variation in the feedback field. The proposed design produces a thermal variation of the field of less than 0.1γ with a coil power of 20 mW.

Rejection of Thermal Gradients - The sensor enclosure should be isothermal, since gradients of 1°C lead to field variations in the 0.1γ region (because of imperfect cancellation of the copper coil thermal expansion).

A thermal shield is required to reduce the internal temperature gradients. We use a shield which is a "tee attenuator" — it consists of two layers of multilayer low-emissivity superinsulation separated by a graphite-epoxy housing which performs the dual functions of thermal shunt and cover.

We will now describe the design in more detail, starting with the fluxgate assembly.

TABLE 4-14. FEATURES OF THE RECOMMENDED SENSOR DESIGN

Design Feature	Motivation
• Triaxial Feedback	- Greatly improves axial stability.
• Small Ring Cores (3/8 inch, ~1 cm)	- Meet noise specification. - Reduced alignment sensitivity.
• Helmholtz Coils	- Adequate uniformity; even better if adjusted to optimize flatness.
• Large Helmholtz Cancellation Coils	- Exactly cancel dipole field. - Very low internal gradients. - No quadrupole field. - Lower power.
• Spherical Coil Supports	- Single rigid structure. - High thermal conductivity. - Acceptable weight.
• Thermal shield	- Isothermal enclosure.

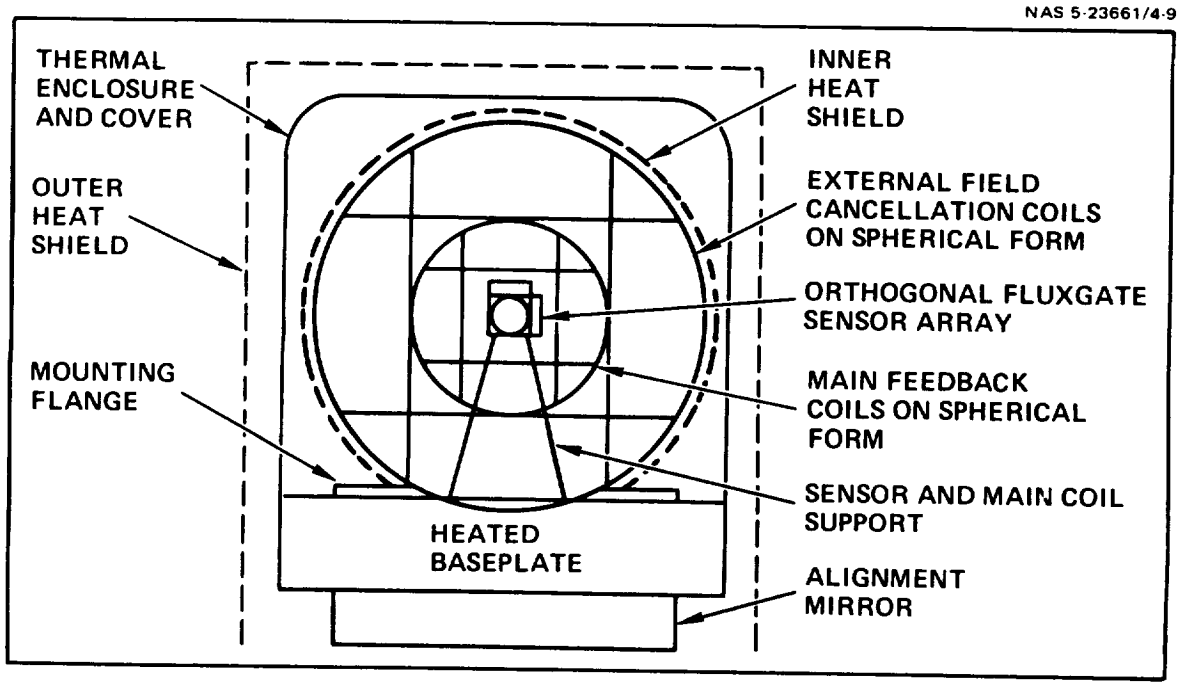

Figure 4-9. Conceptual Sensor Arrangement. The three orthogonal fluxgates are mounted at the center of two coil systems: one to produce the feedback field, and one to cancel the external field.

DETAILED DESIGN OF THE FLUXGATE SENSORS

The 3/8-inch ring-core fluxgates use half-mil 6-81.3 Mo-Permalloy tape wound on an Inconel bobbin. The tape height is 1/8 inch. The sensors are mounted orthogonally on a cubic mount.

A specific design for the fluxgate sensor to be used has been developed as a baseline for the study. The sensor described here has been made as small as possible consistent with the budgeted noise.

The fluxgate sensor is essentially a magnetic amplifier. It consists of a square loop core which is made to saturate alternately in each direction by an alternating current in an ac drive winding. In the presence of an external field, the two halves of the core saturate at slightly different times, giving rise to a flux change at twice the drive frequency which is sensed and amplified to obtain a measure of the external field.

The sensor exhibits both noise and offset; the theory of these effects is discussed in Appendix A. The considerations required to obtain low noise and offset are somewhat different than for a magnetic amplifier because the signal field is external; it is important to design the sensor to intercept as much of the external flux as possible using a minimum amount of noisy core material.

Design Considerations - To achieve a high signal-to-noise ratio with low drive power one must use a core material with a high permeability and square hysteresis loop such as molybdenum Permalloy. The best results have been obtained with an alloy consisting of 6% Mo, 81.3% Ni, and 13.7% Fe; this alloy has zero longitudinal magnetostriction. The method by which the material is prepared and annealed is important.

Because the Permalloys are very sensitive to stress, extreme care must be taken in mounting the core to avoid offsets. The procedure used at NOL and TZL employs a single spot-weld to hold the tape on an Inconel bobbin whose thermal expansion matches that of the tape. It is not a good idea to clamp or pot the tape, so it is difficult to guarantee second-of-arc alignment stability by design — hence, the use of triaxial feedback.

Specific Design for MAGSAT - One-inch ring-core sensors built in the above fashion exhibit typical noise levels of 0.1γ peak for a 25-Hz bandwidth (about 0.01γ rms). The theory in Appendix A shows that the noise-equivalent field scales as the 3/2 power of the diameter and the square root of the tape height. Thus, the diameter can be reduced by a factor up to $10^{2/3}$ if the noise can be as large as 1γ peak — or to about 0.3 inch. The allowable size of the fluxgate is set by the size of the flat-field volume in the triaxial feedback coils (see following discussion); a diameter of about 1 cm, or 3/8 inch, is acceptable.* We predict a noise level of about 0.8γ peak for this size sensor, within the 1γ specification. The offset variation will be close to the ±0.4γ specification, so one would not want to make the sensors any smaller.

The tape is mounted on a thin-walled Inconel bobbin. A thin bobbin wall thickness is desirable to reduce the drive-circuit leakage inductance and also to reduce the eddy currents in the Inconel.

*Because tape and other mechanical dimensions are still specified in industry in English units, we have used these units rather than SI units in what follows.

The drive winding is then wound on the toroidal bobbin and the sense winding is wound over it without a form to minimize the height. A plug is used to fill the bobbin to provide support using a flexible epoxy to avoid stressing the bobbin and tape.

The electrical characteristics of the sensor are shown in Figure 4-10.

Mounting of the Sensors - The sensors are mounted on the surface of a cube. The height-to-diameter ratio of the sensor core tape has been selected to minimize the signal-to-noise ratio with a specified size constraint; this optimization leads to the conclusion that the tape height should be 1/3 of the tape winding diameter.

Sensor Manufacture - TZL has fabricated such sensors in-house using a released manufacturing procedure based on the NOL procedure, and has also recently purchased similar sensors. The procedure is not difficult providing the material and the assembled sensor are annealed properly.

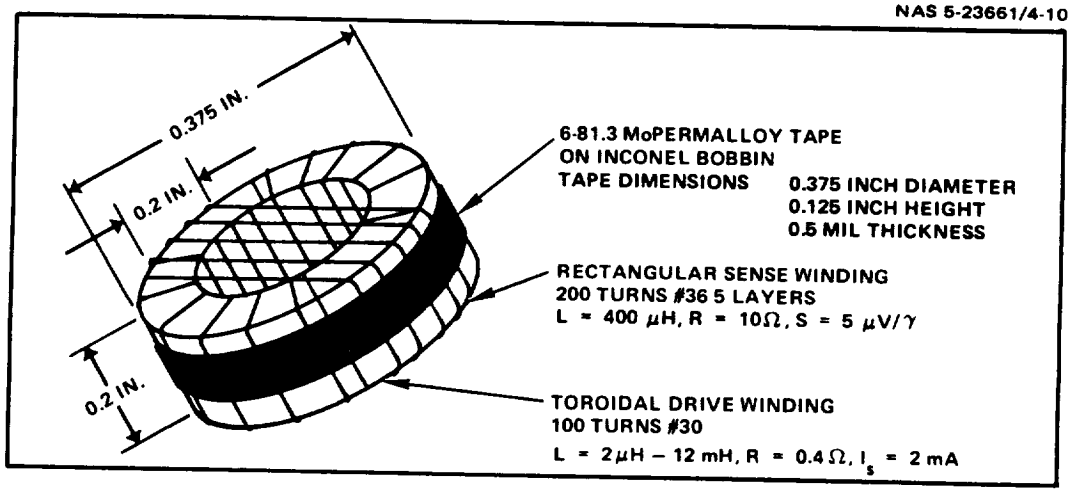

Figure 4-10. Fluxgate Sensor. The inductance and resistance are given for each winding as well as the sense winding sensitivity, S, and the drive winding saturation current, I_s.

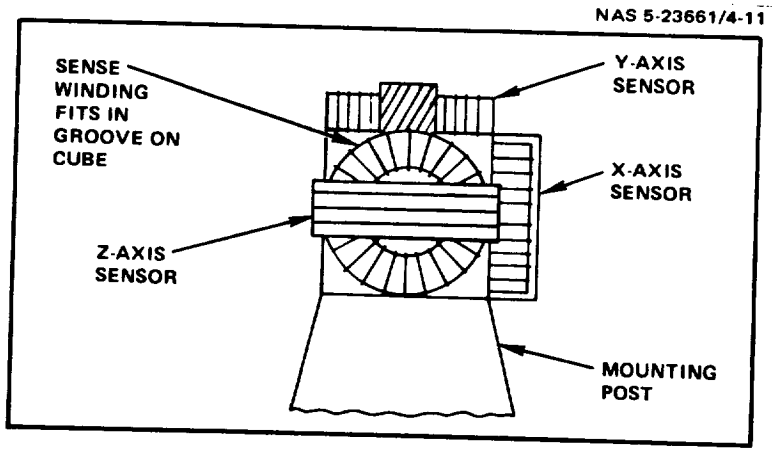

Figure 4-11. Sensor Mounting on a Plastic Cube. The sensors have been designed to provide maximum signal to noise ratio with this mounting configuration. The sensors are spot-bonded to the cube. Need for a high degree of mounting precision is eliminated by use of triaxial feedback.

MAGNETIC CONFIGURATION OF THE FEEDBACK COILS

The simplest feedback coil system which provides the required uniformity and external field cancellation consists of two pairs of Helmholtz coils per axis with a slight modification of spacing to flatten the field at the sensor.

As explained previously, the problem in designing the feedback coils is to provide a sufficiently uniform feedback field with a simple, mechanically stable configuration. The previously presented configuration analysis is reviewed briefly here.

Requirements for Field Uniformity - According to the adopted error budget, translation of the sensor should give rise to repeatability of less than 0.5γ, while rotation of the sensor should give rise to worst-case repeatability of less than 2.5 seconds of arc or 0.78γ; both values apply for a full-scale feedback field strength of 64000γ.

Methods for Generating the Field - As we have indicated previously, an almost perfectly uniform field can be generated by distributing many windings in the surface of a sphere uniformly spaced along the polar axis; the question is simply how many windings to use to achieve a given uniformity. If the number of windings used is 2N, the field inside varies near the center as r^{2N} when the windings are positioned correctly. One can do even better by adjusting the radius of each coil as well as the spacing. The simplest configuration is the so-called Helmholtz coil pair, consisting of two coils separated by their radius. For this spacing, the field at the center of the coils is flat to the fourth order in the distance from the axis (that is, the first three derivatives of the field strength vanish at the center of the field). A consequence of this constraint is that the quadrupole moment of the coils vanishes; there is no term in the far field varying as r^{-5}, a consideration important in meeting the external field specification. The external field has an r^{-3} dipole term, but the next (octupole) term varies as r^{-7}.

Cancellation of the External Field - By the arguments presented previously, the outer coils must be designed to cancel the external dipole field of the inner coils, which means that the dipole moments must be equal and opposite. The dipole moment of a coil is equal to the product of the ampere-turns and area of the coil. Thus, if the outer coils are twice as large as the inner coils, they need only have one-fourth the number of turns. The internal field of the outer coils is then one-eighth the field of the inner main coils. The external field is then essentially an octupole field, which is only 0.016γ at a distance of 60 cm (24 inches) from the center of the coils when the central field is 64000γ.

Adjusting the Field for Flatness at the Sensor - The sensors are not located at the center of the field but are offset from it. Motion in the direction of this offset is important but motion in the other directions is negligible by symmetry.

One can adjust the coil spacing to reduce the gradients in the neighborhood of the sensor. Figure 4-12 shows the variation of the axial component of the field, in γ, as a function of radius in the offset radial direction along the central plane. The calculation assumes that the outer cancellation coils have twice the radius of the inner coils and have a fixed spacing equal to their radius. The calculation was performed by a numerical quadrature of the vector field integral. The sensor location is indicated.

The field gradient can clearly be eliminated by making the inner coil spacing slightly less than 0.94 times the radius so that the field is symmetrical across the sensor. An uncertainty of 0.004R (0.005 inch) in the feedback coil spacing leads to a sensor gradient of about 20Y/0.04R, or 400Y per inch. This gradient implies a sensor position repeatability of about 0.001 inch which is an easily met tolerance.

Sensor Alignment Requirement - If the sensor normal to the field is cocked by a small angle $\Delta\theta$, the sensor output will be in error by the amount $\Delta B \Delta\theta$, where ΔB is the difference in the field seen by the sensor parallel to the field and the one perpendicular to it. Figure 4-13 shows the field as a function of the coil spacing. If the spacing is chosen to minimize the translational error (the larger effect) the field difference is only 120Y, which leads to a sensor core alignment repeatability requirement of 0.3 degree, a requirement which is 200 times easier to meet than 5 seconds of arc.

This analysis shows that the performance of a Helmholtz coil system is more than adequate to provide a feedback field allowing good margins for alignment stability of the fluxgate sensors.

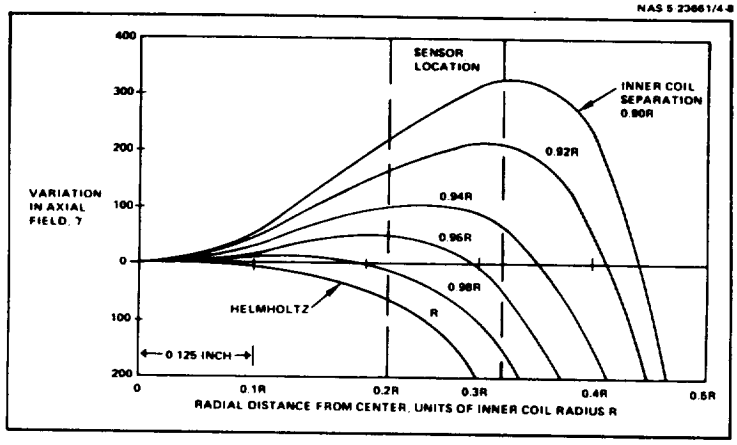

Figure 4-12. Variation in Axial Field for Various Radial Offsets in Central Plane. The sensor position is indicated. The field variations apply for an axial field of 64,000Y. The field can be flattened by making the inner coil separation about 0.935R. The field of the cancellation coil is included.

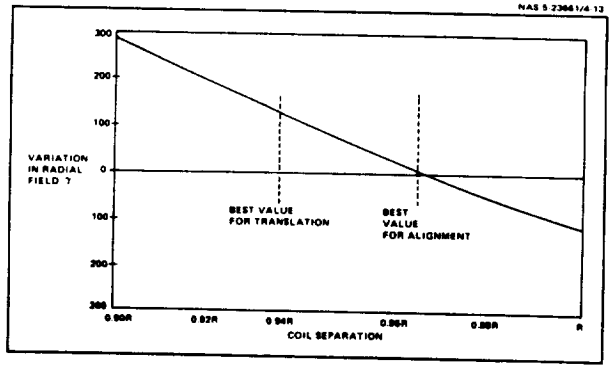

Figure 4-13. Radial Field Difference Between Parallel and Perpendicular Sensors as a Function of Coil Separation. The difference of about 120Y means that the sensor alignment need only be stable to about 0.3^{o}.

ELECTRICAL DESIGN OF THE FEEDBACK COILS

The main feedback coils will be about 2.5 inches in diameter with a 2 mm cross section. The outer coils will be slightly larger than 5 inches in diameter to allow for mechanical clearances. The total coil power will vary from 5 to 20 mW.

Having selected the basic coil geometry, we must now determine the coil power, winding cross section, and winding requirements. The design objectives are to minimize the coil power to reduce self-heating, and to minimize the coil cross section so that mechanical interferences will be reduced. The values calculated here are nominal, because in practice the coil diameters have to be adjusted slightly for mechanical clearance of coils on the three axes.

Coil Power - The power allowable in the coils was estimated by a thermal calculation. The thermal expansion of the coils due to self-heating effect produces a non-linearity which must be less than 1.5Y/64000Y, or 23 ppm. One would like to see something a good deal smaller, to avoid thermal lags. We took 0.5Y as a design goal, and the temperature coefficient of copper (17 ppm/^{o}C) as the relevant sensitivity parameter, implying that the temperature rise should be less than 0.5^{o}C. A simple thermal model for the coil support was used to select a design goal of 5 mW for each inner coil, neglecting the complication of the outer coil.

Determination of Coil Cross Section - For a given field-filled volume, the coil power depends only on the copper cross section. For a Helmholtz coil pair, the power is given in terms of the internal field by the following equation, in which ρ is winding resistivity, A_w is winding cross section, R is coil radius, and μ_o is $4\pi \times 10^{-7}$ H/m:

$$P = \left(\frac{5}{4}\right)^2 \left(\frac{3\rho}{A_w \mu_o}\right)\left(\frac{\frac{4}{3}\pi R^3 B^2}{2\mu_o}\right) \qquad (1)$$

The formula is writen this way for a reason: the second expression involving B^2 is proportional to the magnetic energy in the field, while the term involving ρ is dimensionally a frequency which depends only on the ratio of resistivity to the winding cross section. From this formula, one finds that for P = 5 mW per coil, A_w should be 3.46 mm^2, corresponding to 273 turns of No. 36 wire on each coil with a resistance of 71.4Ω, and an inductance of about 8 mH per coil.

Drive Current - The drive current can be calculated from the formula for the field of a Helmholtz coil, which is

$$B = \left(\frac{4}{5}\right)^{\frac{3}{2}} \frac{\mu_o NI}{R} \qquad (2)$$

For B = 64,000Y and R = 1.25 inches (0.03125 m), the value of NI is 2.26 A-turns, giving a value for the current of 8.27 mA. Smaller wire can be used to raise the coil resistance and reduce the drive current, keeping NI constant.

Correction for Cancellation Coil - The cancellation coil reduces the internal field by one-eighth, so that the drive current must be increased by a factor 8/7 to 9.45 mA. The cancellation coil power is half the inner coil power; the total power is

$$P = (2 \times 5 + 2 \times 2.5)\left(\frac{8}{7}\right)^2 = 19.6 \text{ mW} \quad (3)$$

The coil constant is thus 6.77Y/μA if #36 wire is used. The coil winding parameters are summarized in the schematic opposite.

Power Variation in Orbit - The power input to the triaxial coil assembly never goes to zero in orbit as it does for a single-axis sensor. Since the power is proportional to the squared magnitude of the vector field, one may use the dipole equations to estimate that the power for an orbit crossing the magnetic pole varies as

$$P \sim \frac{P_o}{4}(1 + 3\sin^2\lambda)$$

where λ is the magnetic latitude, and P_o = 19.6 mW. The maximum rate of change of power input occurs for a magnetic latitude of 45 degrees, when it is 5 μW/second. This result can be used to estimate the self-heating lag.

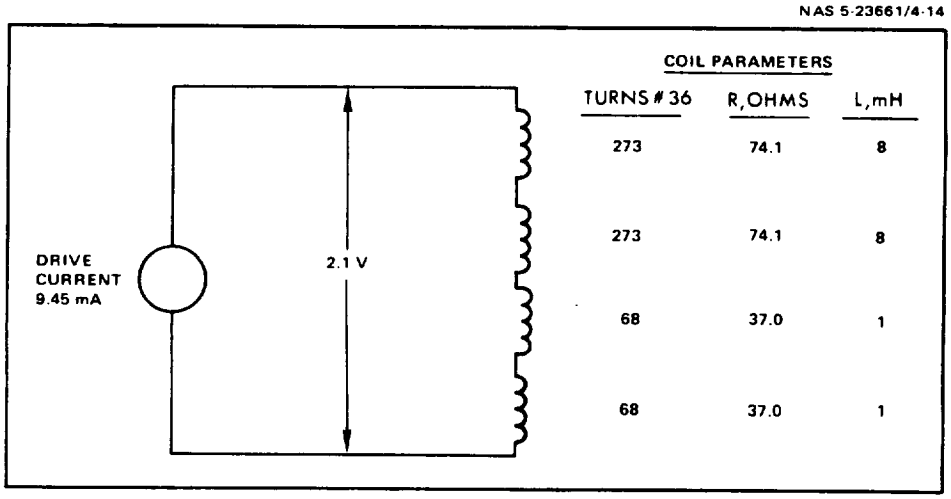

Figure 4-14. Coil Schematic. The inner and outer coil diameters are 2.5 inches and 5 inches respectively. This design is nominal, since it does not allow for the slight differences in coil sizes needed to allow for mechanical clearance between coils.

MECHANICAL AND THERMAL DESIGN OF THE SENSOR ASSEMBLY

Designing with graphite-fiber epoxy-resin material produces a mechanically rigid and thermally stable structure.

Mechanical and thermal stability of the feedback coils is a principal factor in determining the gain, linearity, and alignment stability of the instrument. The coil supports should also be light and easily assembled.

The design must be rigid enough so that no permanent deformation is experienced after environmental testing. The thermal deformation resulting from operating temperature change, self-heating, or external gradients must be small enough to produce acceptable errors in the magnetic field.

To meet these requirements, the structure must be designed with a minimum number of pieces, so that tolerance buildup at mechanical joints is reduced.

The structure must be made with adequate cross section to provide the desired rigidity, and the pieces must be made from a light, thermally and structurally stable material with a close-tolerance construction.

The design which meets these requirements is shown opposite; the table summarizes how each of the design requirements is met.

Mechanical Design - The structure is composed of four pieces: base, sensor tower, and two spheres. Assembly of each sphere to the tower, and the tower to the base employs an interference fit. An adhesive is used as an additional retaining feature to provide a backup during dynamic environments.

Each element of the structure is designed to optimize its individual requirements. The base plate provides a flat surface for mirror mounts on one side and a platform for the sensors, feedback coils, and field cancellation coils.

The sensors are mounted on a stepped cylindrical tower which is machine-finished to provide the necessary flatness for axis alignment. The feedback and cancellation coils are molded on spherical forms which provide a significantly higher degree of structural stability than could be attained by attempting to assemble individual coil forms into a triaxial arrangement. The spherical form also provides an inherent structural symmetry which provides resistance against the tendency to warp or twist.

Selection of Material - An investigation of the nonmetallic materials capable of meeting design requirements leads to use of a graphite-fiber epoxy-resin system such as the GY-70 fiber-reinforced epoxy. When properly fabricated (proper fiber orientation), the material exhibits properties such as:

- Temperature coefficient less than 1 ppm/°C.
- Tensile modulus >40 x 10^6 pounds per square inch.
- Tensile strength >100,000 pounds per square inch.
- Thermal conductivity ≥most metals.

Thermal Considerations - The feedback coils require high stability with regard to thermal effects. By using a thick-walled sphere as the coil form, three positive thermal benefits are obtained: first, the thermal conducting path is good, minimizing gradients; second, a large surface area is available for radiative heat transfer; and third, thermal stresses can be more uniformly distributed within the structure.

To further minimize inputs to the feedback coils, an active/passive thermal control system is provided. The system contains multilayer

insulation, a heating element, and a thermal shunt. Design of the thermal shield and controller is discussed in another topic.

This design has been analyzed to determine its mechanical and thermal performance; an analysis of the structural stability is next presented.

In addition, a detailed evaluation of the recommended structure and material selection was performed. The results of this evaluation appear in Appendix B.

TABLE 4-15. DESIGN REQUIREMENTS AND APPROACHES

Requirement	Approach
• Lightness	- Simple, rigid structure. - Graphite fiber material.
• Ease of Assembly	- Four-piece assembly.
• Rigidity	- Adequate cross sections. - Graphite fiber material. - Close tolerances. - Press-fit construction.
• Thermal Stability	- Thick-walled spherical forms - Graphite fiber material. - Thermal control system.

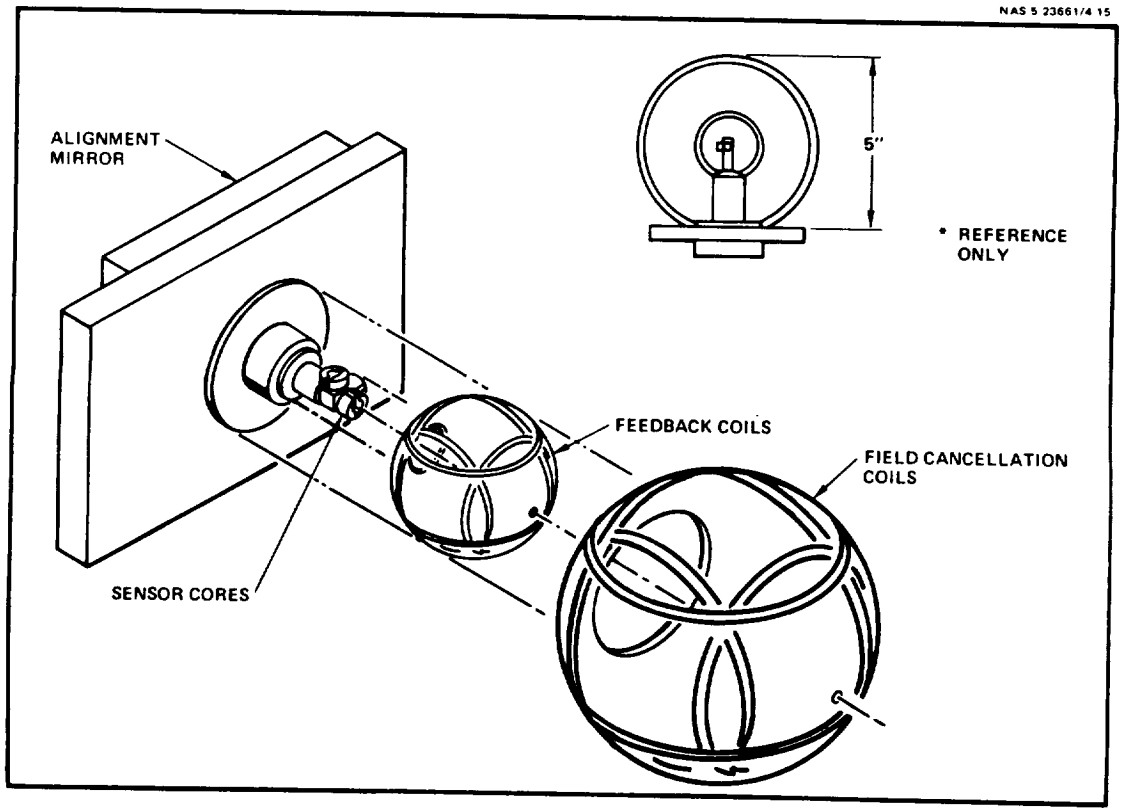

Figure 4-15. Sensor Mechanical Design. A high degree of stability is attained through the use of a simple spherical form and graphite-fiber epoxy-resin material.

ANALYSIS OF STRUCTURAL STABILITY

Analysis of static one-g loads and dynamically induced deflections and stress shows that the sensor will exhibit excellent repeatability and very low static misalignments.

The analysis was performed to evaluate the effect of all mechanical and thermal factors which could have an impact on sensor stability. Emphasis was placed on factors affecting the alignment of the field inside the triaxial feedback coils, as these are the principal factors affecting sensor stability. The details of the analyses presented here appear in Appendix C.

The analysis examines two areas: stability in zero- to one-g fields requiring stability of ±0.5 arc-second per degree Celsius, and dynamic loads of thermal cycling, shock, acceleration and vibration which require cumulative stability of ±2.5 arc-seconds (repeatability). The stability figures are those assigned by the error budget discussed previously. The analysis also considers effects of the use of adhesives and creep, a troublesome property of viscoelastic materials.

Static Analysis - Static feedback coil stability is affected by mechanical deflection of the spherical coil form. The coil form nominal diameter is 2.5 inches with 0.2-inch thick walls and weighs 0.43 pounds. Assuming a tensile modulus of 10×10^6 pounds per square inch, the maximum static deflection which occurs in test at 1 g (in space it is 0 g) is less than 4.0×10^{-7} inches/inch (corresponding to 0.01 arc-second). This value is better than the requirement value by more than an order of magnitude.

Another effect on static feedback coil stability is deflection of the coil with respect to the mirror mount. This value is 1.0×10^{-7} inches/inch, more than an order of magnitude better than the required value.

Dynamic Analysis - The design approach used for the structure produces low stresses during maximum dynamic inputs. The low stresses, coupled with the high tensile modulus (42×10^{-6} psi parallel to the fibers) permit repeatability within ±0.2 arc-second (the mechanical budget is ±2.5 arc-seconds). The lowest resonant frequency of the structure exceeds 4000 Hertz, precluding amplification of dynamic inputs during vibration (maximum vibration test is 2000 Hz).

The maximum dynamic deflection (assuming a 28 g input) within the structure occurs at the location of the 3 axis sensors, and is 9.52×10^{-6} inches per inch. This maximum deflection is far less than even the allowable static deflection of 0.001 inch. All other deflections contribute less than 0.2 arc-second error. The maximum dynamic stress of the assembly which occurs in the graphite-epoxy baseplate, is 189 pounds per square inch, which is insignificant when compared with the baseplate material yield strength of about 50,000 pounds per square inch.

Dynamic Thermal Stress - The temperature coefficient of the graphite-epoxy coil form is negligible compared to that of the copper winding. Because the coils will be wound at room temperature (~21°C), the coil form diameter will try to contract or expand about 0.005 inch when exposed to the specification temperature extremes of -50°C and +85°C. Analysis shows that at -50°C, stress in the coil wires will exceed the wire yield stress (~10,000 psi) and actually exceed the maximum allowable tensile stress (35,000 psi) if the coil diameter is prevented from shrinking. This condition can be avoided by providing a thin flexible elastomeric layer as a base for the coil windings, allowing diametral changes without exceeding the yield stress. Elastomeric adhesives will be used to hold the individual

coil wires in place at temperatures above 21°C so that the wires will return to the same relative positions at the normal operating temperature of the sensor. By design, the ±2.5 arc-second repeatability is met.

Adhesives. - Adhesives are used only as a backup to the assembly, which utilizes interference fits. The adhesives do not contribute to stresses or deflections.

Creep Effects - Creep can be expressed as continuous deformation of a viscoelastic material under load beyond the initial deformation, measured immediately after the load is applied. Because creep rate is proportional to elastic modulus, a material with a high modulus exhibits a minimum tendency toward this effect. By comparing the graphite-fiber epoxy-resin system with other viscoelastic materials, a conservative estimate of the maximum creep rate can be determined. Using a value of creep rate equal to 0.002, we can equate this to a decay in the elastic modulus of 2% in a 5-year period. It follows that the effect on stability will be 2% additional error. Because stability is well within acceptable limits, a 2% additional error is negligible.

This analysis shows that the structure is far stronger than required to withstand the environmental stress and to exhibit negligible differences in alignment between 0 and 1 g.

TABLE 4-16. ANALYSIS OF CRITICAL ELEMENTS

Element	Analysis Type	Maximum Deflection or Stress	Spec.	Result
Feedback Coils	Static 1 g	0.02 arc-second	±0.5	Meets spec.
Feedback Coils	Dynamic (28 g)	0.56 arc-second	N/A*	Meets spec.
Sensor Cores	Dynamic (28 g)	1.63 arc-seconds	N/A*	Meets spec.
Baseplate	Dynamic (28 g)	189 pounds/ square inch	—	Does not yield
Feedback Coil Wires	Thermal	≪2.5 arc-seconds	—	Meets spec.
Feedback Coil Mount	Static 1 g	0.34 arc-second	±0.5	Meets spec.

*The instrument does not have to operate in vibration, but note that the dynamic misalignments during vibration test are less than the specified misalignment tolerance of 2.5 seconds of arc.

STRATEGY FOR CONTROLLING THERMAL EFFECTS

Mean temperature variations are reduced by use of active temperature control, while the effects of gradients are eliminated by the use of isotropic structural material, thermal insulation, and a thermally conductive structure with low internal power dissipation.

To provide the absolute accuracy and alignment stability required for MAGSAT, it is necessary to avoid thermal expansion of the feedback coils, particularly distortions arising from unequal expansion of different parts of the structure. Even if the structure is monolithic, so that all parts of it have the same expansion coefficient, such differential expansions can result from temperature gradients in the structure.

Need for Active Temperature Control - Even when thermally stable structural materials are used, there is still a requirement for temperature control. The overall temperature coefficient of the coil structure will have a non-zero thermal expansion coefficient because of an imperfect match between the thermal expansion of the copper and that of the coil forms; we estimate that the coefficient could be as large as 2 ppm/^{o}C, leading to a field temperature coefficient somewhere between 1 and 2 ppm/^{o}C by our previous sensitivity analysis. Because an overall stability of about 20 ppm is needed, with errors arising from several additional sources, mean temperature control to about $\pm 1^{o}$C is desirable. Several methods of achieving this control were considered; as discussed later, it appears that an electrical heating scheme fits the requirements best.

Material Selection - The graphite-epoxy material recommended has two virtues: very high elastic modulus and hence high rigidity, and high thermal conductivity – much higher than that of most plastics and at best comparable to such metals as titanium. However, this material is often furnished as a laminate having high elastic and thermal conductivity only in the plane of the laminations. Use of such an anisotropic material for the coil forms and supports might lead to trouble as a result of unequal thermal expansion in different directions. For this reason, the recommended material is isotropic with randomly-oriented graphite fibers.

Shielding for Elimination of Temperature Gradients - Temperature gradients arise from the heating of the magnetometer by the sun on one side and by cooling to space on the other side, as well as from self-heating of the coils and sensors.

The elimination of gradients implies that the thermal model of the important parts of the instrument – namely the feedback coil structure and baseplate – should be represented to a high degree of accuracy as a single thermal node. This requirement implies careful insulation of this node from external influences, the use of a highly conductive structure, and the avoidance of self-heating by keeping the coil power input low. All of these requirements are met by the design.

Solar Heating Effect - The orientation of the instrument and satellite in orbit is indicated in Figure 4-16. In the nominal near polar orbit, one side of the instrument will be continuously illuminated by the sun, while the other side will be continuously exposed to space (the eclipse case is discussed later). By using a surface coating with a low solar absorptivity and high emissivity on the sun side (e.g., white paint), and (if possible) a surface with a low emissivity on the space side, the temperature gradient across the instrument can be minimized. Then, a superinsulation and a conductive housing and coil structure can provide the rest of the isolation required.

The main effects then become heat losses from the first-surface alignment mirrors mounted on the baseplate and losses to the uncontrolled instrument mounting shelf. Gradients produced by this cooling effect can be reduced by applying heat behind the mirrors using an appropriate printed-circuit heater, and by isolating the baseplate from the instrument mount. This thermal design is discussed in more detail later.

Self-Heating - The coil and sensor power was selected to provide acceptable gradients from self-heating effects. The analysis presented later shows that in the recommended design such effects produce negligible changes in the measured field.

We now turn to the details of the thermal design and performance analysis.

TABLE 4-17. THERMAL CONTROL STRATEGY

Effect	Control
• Mean Temperature Variation	- Active thermal control with electric heater.
• Solar Heating Gradients	- White surface coating. - Superinsulation. - Conductive housing, structure, and baseplate.
• Backplate Gradients	- Heater location. - Housing insulation.
• Self-Heating Gradients	- Low coil power. - Conductive coil structure and baseplate.

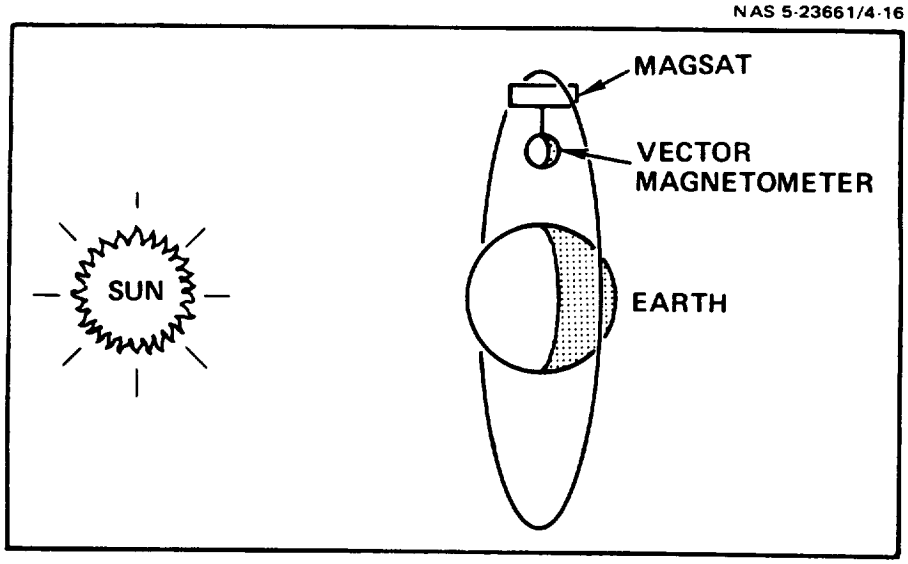

Figure 4-16. Orbital Heating. In a dawn-dusk orbit, one side of the instrument will be continuously illuminated.

ANALYSIS OF SELF-HEATING EFFECTS

Analysis shows that self-heating errors are negligible, being less than 5×10^{-3} γ for the largest effect, due to the use of high thermal conductivity graphite composite structural materials.

We now try to estimate the thermally induced errors for the most critical sensor component, the feedback coils and the supporting structures. Since 7/8 of the feedback field is produced by the inner set of Helmholtz coils, their behavior is seven times more critical than that of the outer cancellation coils, and primary consideration is given to the inner coils. Operating temperature, gradients, and self-heating can affect the gain, linearity, and alignment through geometric changes due to thermal expansion.

Temperature Rise Due to Self-Heating - An approximate thermal model shown opposite has been analyzed by linearizing the radiation conduction equations between the three major components of the sensor: flux gate cores, feedback coils, and field cancellation coils. The cores, which generate 15 mW, maximum, are conductively coupled through their support to the baseplate reference with a resistance of 40°C/W and radiatively coupled to the surrounding feedback coil sphere with 224°C/W. The feedback coils, generating 13 mW maximum, are conductively coupled to the reference via 4°C/W and radiatively to the field cancellation coils by 13°C/W. The field cancellation coils with 6.5 mW also in turn conduct through 4°C/W, and we neglect for the moment any radiation terms to the outside. The solutions for this network are $T_1 = 0.5°C$, $T_2 = 0.06°C$, and $T_3 = 0.04°C$ due to maximum self-heating.[1]

Thermal Expansions - We use an effective coefficient of thermal expansion of 1 ppm/°C for the support structure calculated from the coefficients for copper and graphite-epoxy and their relative tensile strengths. Translation of the sensor cores, with a sensitivity of 0.5 γ/mil, changes in feedback coil constant (gain and linearity) with $\Delta B/B \approx 1$ ppm/°C, and alignment sensitivity of 1 ppm/°C yield errors as summarized in the table for the maximum internal field of 6.4×10^4 γ. The effects of self-heating are seen to be well within the budgeted errors and are in fact negligible.

Thermal Lag and Other Effects - The heat capacity of the structural material used is high and results in an estimated thermal time constant of 300 seconds. Since the total self-heating errors are so small, errors due to thermal lag in a changing field are also negligible. Also, with an electrical resistivity of ~3000 μ ohm-cm, yielding a surface resistance of 6×10^{-3} ohms/square, both eddy current heating in the spherical shell of the coil supports and field screening from the interior are negligible for rates of 250 γ/sec.

With virtually no self-heating errors as determined by the above analysis, we next consider design of the thermal control system.

TABLE 4-18. THERMAL ERROR SUMMARY

Source	Self-Heat Error	Temperature Sensitivity	Budgeted Error
Sensor Core Translation	$2.5 \times 10^{-4}\gamma$	$5 \times 10^{-4}\ \gamma/^{\circ}C\ T_1$	$\pm 0.5\gamma$
Gain and Linearity	$5.1 \times 10^{-3}\gamma$	$6.4 \times 10^{-2}\ \gamma/^{\circ}C\ T_2$	$\pm 0.5\gamma$
Feedback Axis Alignment	$5.1 \times 10^{-3}\gamma$	$0.2''/^{\circ}C$ gradient	± 0.5 arc-seconds

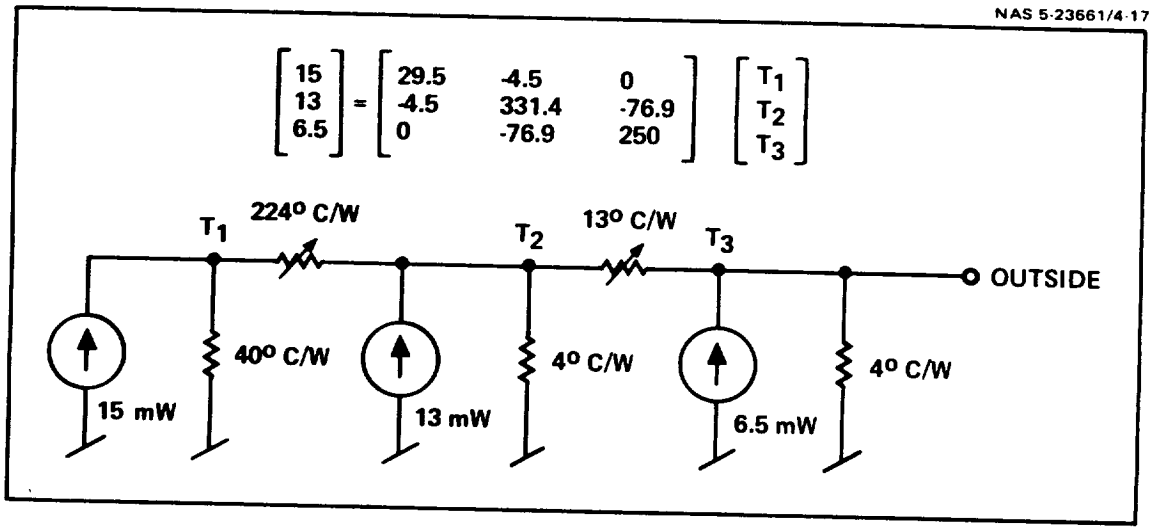

Figure 4-17. Approximate Thermal Model. T_1, T_2, T_3 are the temperatures of the fluxgate cores, feedback coils, and field cancellation coils, respectively. In the matrix equation resistances have been converted to conductances with units of milliwatts and degrees Celsius.

DESIGN OF THE THERMAL CONTROL SYSTEM

A combination active/passive thermal control system prevents excessive heat interchange with the sensor feedback coils.

The thermal interchange between the sensor and its external environment must be minimized to keep misalignment and gain errors within limits. The major problem is heating by the sun on one side and cooling to space on the other side. To stay within the errorallocations specified, the design must include the following features:

Superinsulation - This recommended insulation is actually multilayer aluminized or goldized mylar or kapton. The purpose of the insulation is to provide a very high thermal resistance path from the external environment inputs (solar and space shadow) to the sensor field cancellation coils and feedback coils. The insulation is about 0.5 inch thick and will be placed on the outside of the sensor and in the space between the field cancellation coil and the thermal shunt. The insulation is specially designed for spherical shape to avoid the wrinkling effect obtained if a flat shape is wrapped around a sphere. The outer surface, on the sun side, is painted white to reduce the temperature difference across the instrument. If the orientation can be guaranteed, the finish on the space side should be gold or aluminum. If no such guarantee is possible, painting th entire outside surface white is acceptable.

Thermal Shunt - The thermal shunt is a graphite-fiber epoxy-resin sphere. The principal purpose of the shunt is to equalize thermal inputs to the coil portions of the sensor. This is possible because the shunt provides a good heat conduction path so that the temperature gradient across the shunt is minimized. A thermal control finish is applied to the exterior of the shunt.

Base and Mirror Shield - The mirror and part of the sensor base should not be covered by the superinsulation for obvious reasons. The mirrors must be exposed for alignment by a spacecraft light source and the base must interface with the boom. The rest of the base plate is covered by superinsulation. To minmize sun and shadow radiative heat transfer, a shield is provided to limit the field of view to primarily the spacecraft. Thermal insulation between the sensor and boom interface will minimize conduction heat transfer. It is recommended that the portion of the boom interface with the sensor also be insulated and that the boom thermal conductive area be small.

Base Heating - Because the passive thermal protection provided by the superinsulation and thermal shunt is only partially available at the base, active thermal control is used (see next topic for design of thermal controller). The mirrors will lose heat by radiation and hence an active heating element is necessary. A printed circuit type film heater and temperature sensors attached to the sensor base can provide the required base temperature. (Other heaters attached to the thermal shunt can be used to reduce the gradients even further.)

Performance - The multiple-layer approach attenuates the solar flux so that the direct effect on the feedback coils is negligible. The main source of temperature gradients then results from heat flux on the highly conductive base plate, as we will now see.

The first-surface mirror losses are a potentially serious source of loss even though its emissivity is low — 100 mW for a 10 cm x 10 cm mirror with an emissivity of 0.02. By placing the heater behind the mirror, the unbalanced heat flux due to this concentrated source of heat flux are reduced to levels of about 1 mW/cm^2, leading to low baseplate gradients.

TABLE 4-19. THERMAL PROBLEMS AND CONTROL APPROACH

Problem	Control Approach
• Radiation to Sensor Coils	- Passive, Wrap with Superinsulation
• Sun/Shadow Gradients	- Passive, Use a thermal shunt with thermal control finishes.
• Exposed Base and Mirror	- Passive, Shield Base and mirror to minimize thermal inputs.
	- Active, Provide heating element to keep base at required operating temperature.

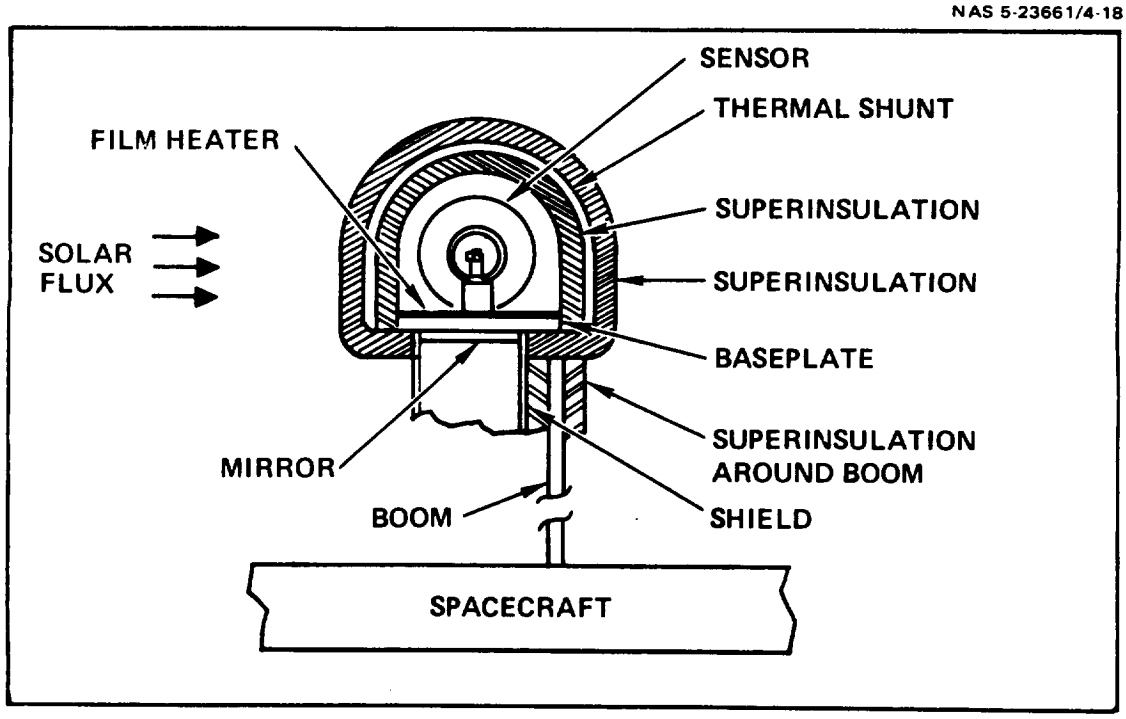

Figure 4-18. Thermal Control System. A thermal shield protects the sensor from external thermal effects.

DESIGN OF THE THERMAL CONTROLLER

Use of a printed circuit heater is recommended to warm the instrument baseplate. The heater should be designed for low stray fields and driven by an ac current, using a thermistor sensor and control amplifier to provide mean temperature control to ±1°C.

Temperature control of the sensor is needed to prevent variation of the scale factor as well as instability of the sensor axis alignment. The control requirement is about ±1°C, although one should be able to do better than that without much trouble.

Selection of Temperature Control Scheme - Three different control schemes were considered — gas flow, passive control by a moving louver, and electrical heating. The gas flow method, using cooling and heating of gas piped up the boom, was rejected because it was difficult to insulate the gas-carrying tubes. The use of a thermostatic mechanism to control a moving louver is an attractive alternative, but the best place to locate such a mechanism is on the baseplate, which is reserved for alignment mirrors.

As discussed previously, a principal mode of heat loss is radiation from the alignment mirror surfaces. It makes sense to distribute heat behind the mirrors, in effect guarding them and eliminating the gradients which the concentrated load would otherwise produce in the baseplate. This uniform heat distribution can most effectively be provided by use of a printed circuit heater.

Avoiding Magnetic Fields - Use of a dc heater drive would obviously be asking for trouble, because of the stray fields that might be produced. An ac drive should be used, at a frequency which is midway (geometric mean) between the 25-Hz low frequency response and the 10-kHz drive frequency — or about 1 kHz.

Use of such an ac drive does not guarantee lack of stray field effects, because the sensor is after all a highly non-linear device and cross-modulation products may result if the stray field is too large, whether it is ac or not. To reduce the stray field of the heater, it should be laid out using a bifilar pattern with high spatial frequencies in two dimensions.

The formula opposite gives the spatial dependence of the vector potential produced by a current distribution periodic in the x-y plane. To satisfy the vector Laplace equation, the fall-off of the z direction must be exponential. One readily estimates from this formula that if the printed circuit conductor spacing is periodic with a typical easily-attained spacing $s/2 = 0.050$ inch, the field at the sensor location (2.5 inches away) will be less than the field near the heater by a very large factor (10^{77}). The field produced by such a periodic conductor layout will thus be very small. The primary source of stray field will be the dipole field produced by unavoidable current loops occurring where connections are made; estimates of these stray fields lead to field strengths of 0.2 γ at the sensors. Such a field strength is acceptable, especially for ac fields, so we conclude that a bifilar pattern heater will indeed work.

Controller Design - The design of the control circuit is straightforward and so has not been worked out in detail. Use of a GSFC PPL thermistor is proposed for the sensor.

It is recommended that the controller be a variable duty-cycle type to achieve efficient operation at constant frequency. The heater can be switched directly across the spacecraft supply with a switch conduction interval determined by the controller error signal. Chokes in series with

the line and load can be used to eliminate harmonic currents which might enter the signal band. A maximum power of 200 mW can be delivered by switching a current of 12.5 mA with a 16 V power supply.

This design appears to offer no difficulties in implementation.

TABLE 4-20. SPATIAL DEPENDENCE OF VECTOR POTENTIAL FROM PERIODIC CURRENT DISTRIBUTION

If the current distribution is periodic in the x-y plane with periods, the two components of the vector potential fall off exponentially in the z direction, perpendicular to the heater plane.

$$A_x \sim A_y \sim \Sigma e^{-k_z z} \sin k_x x \sin k_x y$$

$$k_z^2 = k_x^2 + k_y^2 = \left(\frac{2\pi m}{s}\right)^2 + \left(\frac{2\pi n}{s}\right)^2, \quad m, n = 1, 2, \ldots.$$

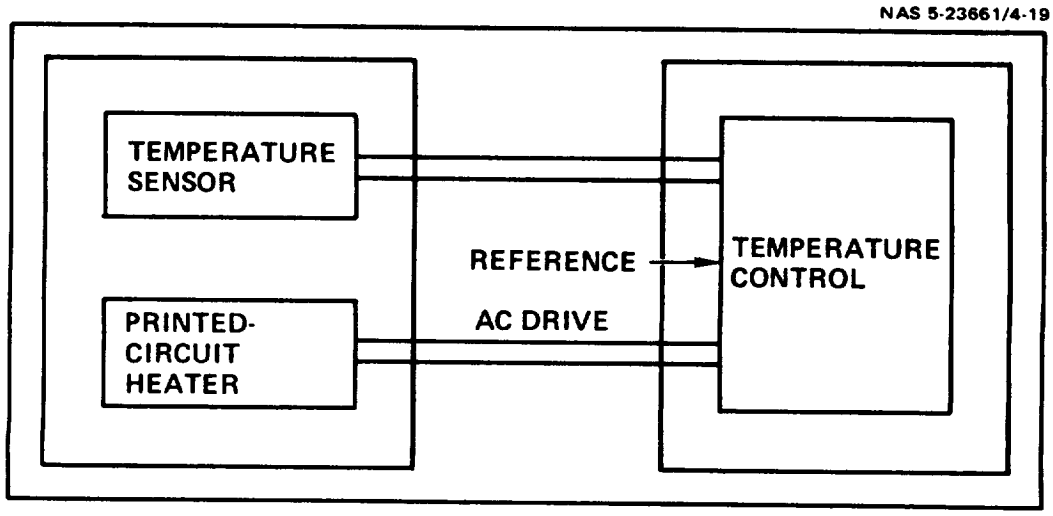

Figure 4-19. Temperature Controller Block Diagram. The heater is driven by an ac current to avoid dc fields.

PERFORMANCE OF THE THERMAL SHIELDING

The successive layers of radiative and conductive shields eliminate temperature gradients across the feedback coils. Temperature variations across the baseplate must be controlled by appropriate thermal design of the heaters and the boom-baseplate interface.

We can estimate the performance of the thermal shield by a simple successive-approximations calculation.

Assume that the thermal shunt is controlled to 300°K, and that the effective emissivity of the surrounding thermal blanket is 0.005 -- equivalent to an ideal 4-layer blanket with surface emissivity 0.02. The outer surface of the blanket is painted white, with a solar absorptivity 0.10 and a thermal emissivity of 0.60.

The temperature T_1 at a point on the illuminated surface at an angle θ from the subsolar point can then be found from the equation

$$\sigma\epsilon_s T_1^4 + \sigma\epsilon_b(T_1^4 - T_2^4) = \alpha_s F_s \cos\theta$$

which expresses the radiation balance on the outer blanket surfaces, neglecting conduction parallel to the blanket. In this equation, σ is the Stefan-Boltzmann constant, ϵ_s is the surface emissivity, ϵ_b is the effective blanket emissivity, T_2 is the inner (shunt) temperature, α_s is the solar absorptivity, and F_s is the solar flux (137 mW/cm^2). Numerical evaluation yields a value of T_1 equal to 253°K at the subsolar point and 90.5°K on the shadowed side.

The flux into the shunt (assumed spherical for purposes of the estimate) can then be estimated by assuming that the heat transfer is essentially radial and that the shunt is nearly isothermal (it is designed, of course, to make that assumption valid). The net heat transfer on the shadowed side is, for an average blanket radius a = 7.5 cm (3 inches).

$$\int F dA = 2\pi a^2 \sigma \epsilon_b (T_2^4 - T_1^4) = 80.5 \text{ mW}$$

On the sun side, one must perform an integral:

$$\int F dA = \int \sigma \epsilon_b [T_2^4 - T_1^4(\theta)] 2\pi a^2 \sin\theta \, d\theta$$

Using Simpson's rule with interval $\theta = 45°$, one obtains the result

$$\int F dA = 57.3 \text{ mW}$$

The flux on both sides is outward, so that the net flux across the shunt is 23.2 mW.

Feedback Coil Gradient - We can then estimate the temperature gradient across the shunt and the inner and outer coils using the thermal model shown opposite. The values of the thermal resistances in the model were estimated from the dimensions and thermal conductivity of the graphite-epoxy shunt and coil forms. If the shunt has series and shunt resistances of 100°C/W, as shown (obtained with a thickness of about 1 mm and a thermal conductivity of 0.02 W/cm^2 - °C), the net gradient across the shunt will only be about 7°C. Then, the high thermal resistance of the inner radiation shield and low thermal resistance of the outer coil form combined to attenuate this gradient to 0.1°C, assuming only a single-layer inner radiation shield. This difference is so small that the gradients must be dominated by gradients in the baseplate.

Baseplate Gradients - Since the thermal control strategy is to shunt heat to the baseplate, there will inevitably be gradients in the baseplate. However, since the component must be thick and heavy for structural reasons, the thermal flux will not lead to large temperature gradients. The estimated temperature gradient is on the order of 2°C across the entire baseplate, or perhaps 0.5°C across the feedback coil mounting flange. Assuming that this gradient is translated directly into a coil misalignment error with a temperature coefficient of 2 ppm/°C, the corresponding misalignment would be 0.2 second of arc.

To summarize, there appears to be no difficulty in shielding the critical components of the vector magnetometer so that the effect of gradients produced by sunshine are negligible. Careful attention must be paid to control of baseplate gradients and design of the boom interface. The interface must be designed to produce low gradients in the baseplate.

Because of the high degree of thermal isolation provided, the performance on an orbit with a partial degree of shadowing (eclipse) will be similar -- better, in fact, because of greater symmetry.

Although the calculations presented are based on a simple model and simplified estimates of thermal resistance, the estimated performance exceeds requirements by a large enough margin so that no difficulties are to be expected when the calculation is refined to improve its accuracy.

TABLE 4-21 ESTIMATED TEMPERATURE GRADIENTS ACROSS COMPONENTS

These values assume the use of a distributed heater on the mirror but not on the thermal shield.

o Outer surface	162°C
o Shunt	7°C
o Outer coil form	0.1°C
o Inner coil form	0.02°C
o Baseplate	1-2°C

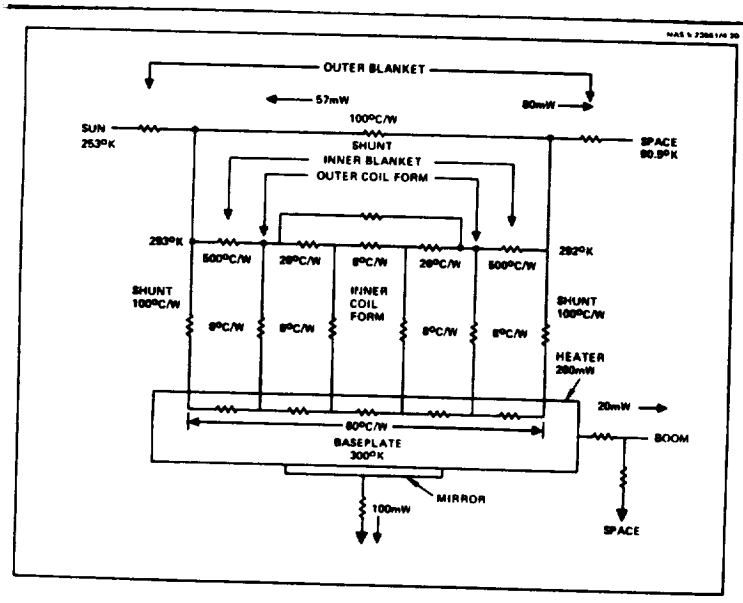

Figure 4-20. Thermal Model for Temperature Gradient Analysis. Successive radiative and conductive layers suppress temperature gradients. To reduce the gradients to the maximum extent, the mirror losses and surface losses should be supplied by distributed heaters.

ESTIMATES OF SENSOR STABILITY

The estimated scale factor stability of the sensor is ±0.06γ, with an alignment stability of ±0.6 arc-seconds. The sensor offset is expected to exceed the ±0.2γ budget slightly.

For convenience in comparing the estimated and specified performance, we have collected the results of our analysis here.

Our performance estimates are based on simple mechanical and thermal models using typical values for the thermal and mechanical parameters of the material used. The estimates will need to be refined in a hardware development program using more sophisticated calculational tools. However, the estimates presented show that the predicted performance is far better than required. We then expect the triaxial feedback sensor to exceed the MAGSAT requirements.

The various specifications are compared with the estimated performance in the table to the right (Table 4-22).

Offset - The fraction of the budgeted offset drift ascribable to the sensor is ±0.2γ. As noted earlier, smaller sensors have larger offset drifts. We did not build and test a sensor of the appropriate size, but do not believe that meeting the offset requirement will be difficult in spite of the fact that the sensor is smaller.

This judgement is based on the NOL test results, in which offset variations of ±0.1γ at constant temperature for a one inch sensor were reported. We predict ±0.3γ for our sensor. This level of offset drift should not be too significant; it is less than the noise, and an insignificant contributor to the overall inaccuracy.

Scale Factor - The scale factor error caused by thermal and structural effects is quite small, even though the estimates are very much worst-case.

The principal source of sensor non-linearity, assuming adequate loop gain in the electronics (treated elsewhere), is self-heating. The use of thick walled graphite-epoxy coil forms makes this effect almost negligible.

Alignment Instability - Alignment instabilities arise from structural and thermal distortions which are not easily calculated. The estimates shown are again very much worst-case assuming that a given thermal or structural expansion translates directly into a misalignment with unit efficiency. The most important effects appear to be baseplate deflections from thermal distortion and, as a result of the finite weight, of the alignment mirrors, but the reduced finite effects are well within the allotted error budget.

Summary - The design appears to yield performance as follows:

- Offset - ±0.3γ
- Scale Factor and Linearity - ±0.06γ
- Alignment Stability - ±0.6 arc-seconds

TABLE 4-22 COMPARISON OF ESTIMATED AND REQUIRED PERFORMANCE

Parameter	Effect	Estimated Performance	Required Performance
Offset	Fluxgate Offset	±0.3γ	±0.3γ
Scale Factor and Linearity	Coil Mean Temperature	±0.06γ	
	Solar Heating	±0.001γ	
	Self-Heating	±0.005γ	
	RSS	±0.06γ	±1.5γ
Alignment	Coil Mean Temperature	±0.2 arc-sec	
	Solar Heating	±0.004	
	Self-Heating	±0.01	
	Baseplate Thermal Distortion	±0.4	
	1-g Deflection	±0.4	
	RSS	±0.6 arc-sec	±2.5 arc-sec.

SECTION 5
ELECTRONICS DESIGN

Summary of Electronics Analysis 5-2

5.1 - CONFIGURATION ANALYSIS

Characteristics of the Single-Loop System 5-4

Characteristics of the Two-Loop System 5-6

Frequency Analysis of the Single-Loop System and Inner Loop of Two-Loop System 5-8

Error Analysis of the Single-Loop System and Inner Loop of Two-Loop System 5-10

5.2 - ELECTRONICS DESIGN AND PERFORMANCE ANALYSIS

Summary of Two-Loop System Design Parameters 5-12

Design of the Reference Generator and the Probe Drive 5-14

Design of the Second Harmonic Amplifier 5-16

Design of the Demodulator and Integrator 5-18

Design of the 12-Bit ADC 5-20

Design of the Feedback Current Generator 5-22

Design of the Digital-to-Analog Converter (DAC) 5-24

Alternative DAC Configurations 5-26

Auxiliary Subsystems and Power Analysis 5-28

Packaging and Thermal Control of the Electronics 5-30

SUMMARY OF ELECTRONICS ANALYSIS

When implemented with carefully selected available components, a two-loop system employing a 12-bit analog-to-digital converter in the inner loop and an offset field generator in the outer loop enables meeting the MASAT Vector Magnetometer performance specifications.

Two topologies were analyzed — a single-loop system employing a 17-bit analog-to-digital converter (ADC) and a two-loop system employing an inner loop with a 12-bit ADC and an offset field generator (OFG) in the outer loop. The inner loop of the two-loop system is similar in many respects to the single loop system.

Because of their similarities, initial performance analyses were performed on both systems. However, after the frequency and non-steady state field error analyses had been completed, and the two systems had been compared with respect to implementation difficulties and systemic characteristics, it was determined that the two-loop system was the best candidate for detail design and performance analysis.

Study Tasks - The electronic study tasks fell into four general areas:

- Analyzing the system characteristics of the single-loop and the two-loop system, as well as their frequency response and stability.
- Selection of one system for detail design.
- Selecting suitable components and topologies for the critical subsystems, which include the ADC, a digital-to-analog converter (DAC), and the feedback current source.
- Synthesizing a complete system to enable a complete weight and power analysis.

A summary of the study results in each of the above areas follows:

System Tradeoff Considerations - Simplified block diagrams of these two systems are shown in Figures 5-1 and 5-2. The single-loop system is simple in concept, but difficult to mechanize as a result of the need for a 17-bit ADC (16 bits plus sign). The two-loop system is somewhat more complex functionally than the single loop because it requires an offset field generator (OFG) with its control circuitry. However, it has the offsetting advantages of putting the critical components in the low bandwidth OFG, which minimizes the effects of systemic noise and enables the use of less telemetry bandwidth. It also has better overload recovery characteristics due to a much shorter integrator time constant.

Frequency Analysis - The frequency characteristics of the two-loop system are stable and easily mechanized.

Critical Components - Both the two-loop system and the single-loop system require ultra-stable components (primarily resistors and operational-amplifiers) which additionally require active thermal control.

System Implementation - An estimate of the weight and power of a totally implemented system shows that the specific weight, volume, and power requirements can all be met.

The general conclusion of the results of each of the above areas is that the critical MAGSAT specifications are achievable. The analyses supporting this conclusion are presented in the following pages.

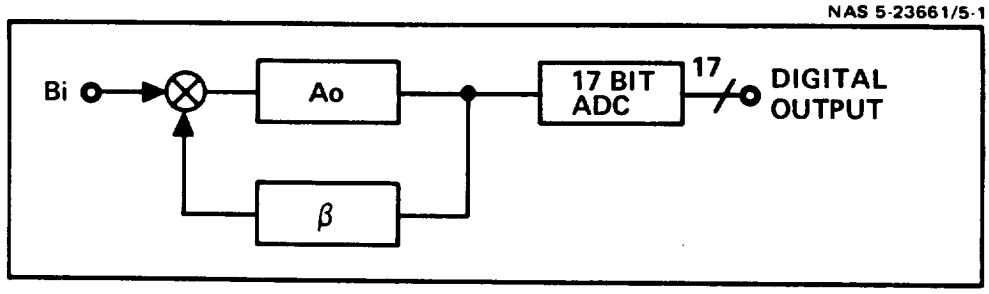

Figure 5-1. Single-Loop System. The single-loop system requires a difficult to mechanize 17-bit ADC which is susceptible to systemic noise.

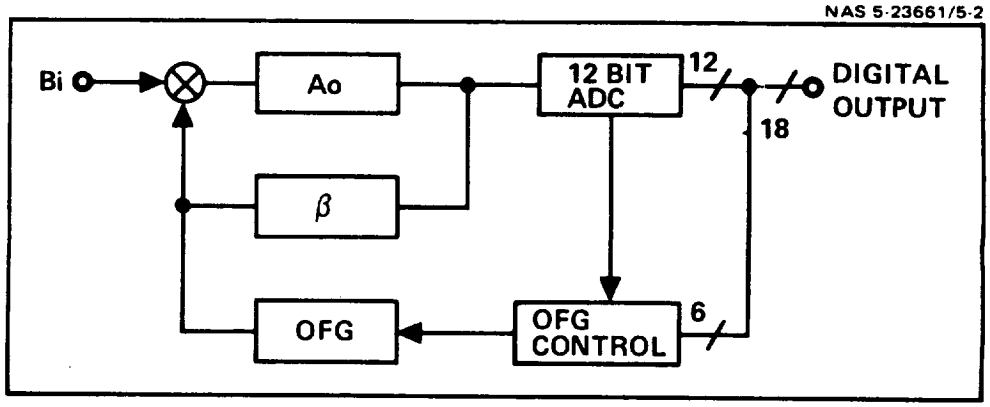

Bi = INPUT MAGNETIC FIELD
Ao = FORWARD LOOP GAIN
β = FEEDBACK GAIN
ADC = ANALOG TO DIGITAL CONVERTER
OFG = OFFSET FIELD GENERATOR

Figure 5-2. Two-Loop System. The two-loop system has advantages overriding its additional complexity.

CHARACTERISTICS OF THE SINGLE-LOOP SYSTEM

Analysis shows that the single-loop system can achieve the required performance, but the wide bandwidth of the critical ADC and current source cause it to be susceptible to systemic errors (pickup, cross coupling, EMI, impedances, etc.). These errors are difficult to analyze but are present in all systems.

The block diagram of the single-loop system is shown in Figure 5-3. The transfer function of each block is defined in the following.

Fluxgate Sensor - The nominal gain and expected uncertainty of the fluxgate sensor (which has been previously described) is

$$K_s = 3.9 \times 10^{-6} \pm 0.2 \times 10^{-6} \frac{\text{volts}}{\text{gamma}} \quad (1)$$

Tuned Bandpass Amplifier - The minimum gain of the bandpass amplifier is determined by the allocated offset error from the total equivalent input drift of the demodulator and the integrator. Assuming that this drift is less than 2×10^{-3}V, and using an error allocation of 0.07Y, then

$$K_a > \frac{1 \times 10^{-3} V}{0.07 Y K_s} = 3.66 \times 10^3 \frac{V}{V} \quad (2)$$

The actual design value for K_a was chosen to be

$$K_a = \frac{4.07 \times 10^3}{(1 + 0.5 \times 10^{-3} s)} \frac{V}{V} \quad (3)$$

Since the amplifier is tuned to the second harmonic of the drive signal, the equivalent pole must be included in its response. The anticipated worst-case variation in K_a and in its associated time constant are both five percent.

Demodulator - The output of the ac amplifier is converted to a dc signal by use of a synchronous demodulator. The dc transfer function of this circuit is

$$K_d = 0.63 \cos\phi,$$

where ϕ is nominally 90 degrees.

Some variation in phase will exist primarily due to variations in the tuned circuits of the ac amplifier. There is also a pole associated with the demodulator, whose value is selected to trim the closed loop frequency response, giving an overall nominal transfer function of

$$k_d = \frac{0.63}{(1 + 1.84 \times 10^{-3} s)} \frac{V\ dc}{V\ peak}$$

The gain stability of the demodulator (including phase variations) will be better than two percent and its time constant will be stable to less than three percent.

Integrator - The output stage of the forward loop is an integrator which provides the required high loop gain and also conveniently stabilizes the loop frequency response. The approximate response for the integrator is

$$K_I = \frac{1}{T_i s} \frac{V}{V} \tag{5}$$

where T_i is selected to be 0.582 second with an uncertainty of one percent. This time constant was selected to provide the desired closed loop response as described in the following section.

Feedback Network - The feedback network contains the feedback coil previously described and a current source for driving each coil. The bandwidth of the current source was made as wide as practicable. One pole, however, does exist which is due to the coil time constant. The transfer function is given by

$$K_g = \frac{1.17 \times 10^{-3}}{(1 + 1.1 \times 10^{-4} s)} \frac{a}{V} \tag{6}$$

The dc errors of the current source are discussed in a following section. For the purpose of the frequency analysis of a following section, it is assumed that the dc scale factor is constant and that the worst-case drift in the time constant is one percent. When combined with the coil constant, the feedback factor becomes

$$\beta = K_g K_c$$

$$= 6.67 \times 10^3 \frac{\gamma}{V} \tag{7}$$

which is the reciprocal of the assumed scale factor of 150×10^{-6} volts per gamma.

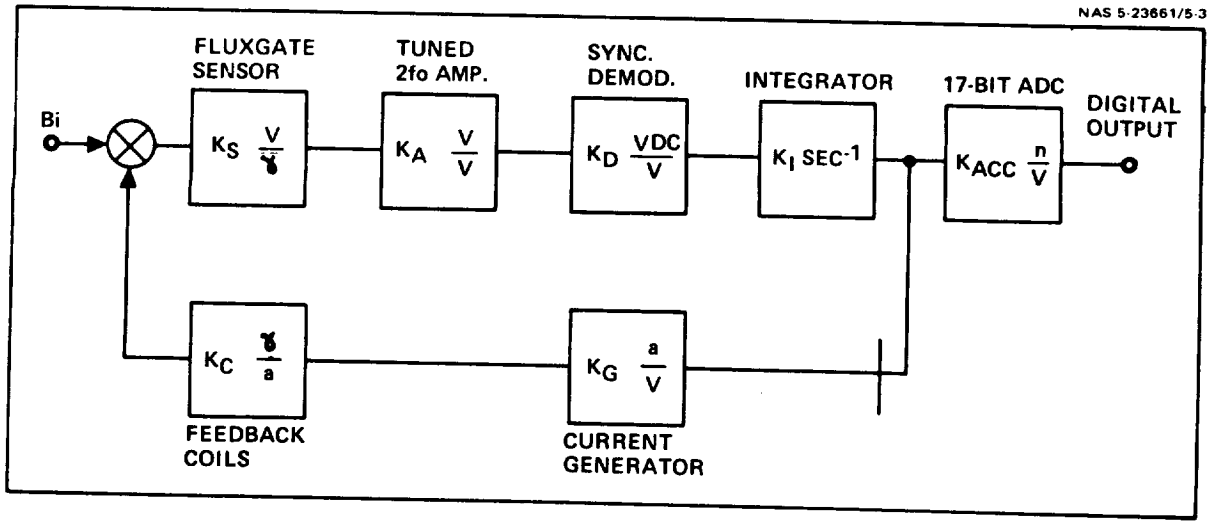

Figure 5-3. The single-loop system is characterized by the need for wide bandwidth in the critical 17-bit ADC and the current generator.

CHARACTERISTICS OF THE TWO-LOOP SYSTEM

In the two-loop system the inner loop provides the high resolution and bandwidth required, while the outer loop — with its offset field generator — reduces susceptibility to systemic errors.

The two-loop system is characterized by an inner loop, which is similar to the single-loop system, and an outer loop or offset field generator (OFG). The block diagram of the two-loop system is shown in Figure 5-4.

Inner Loop - Table 5-1 shows the overall characteristics of the inner loop compared to that of the single-loop system. The most significant parameter variation is that of the output voltage resolution, which is 16 times greater for the two-loop system.

Noise Considerations - The two-loop system can accept systemic noise in the wide bandwidth loop of more than ten times that of the single-loop system. This is a distinct advantage during implementation when dealing with digital transients, power supply noise, spacecraft interference, and all the other sources of noise which are always present and not usually amenable to analysis.

Outer Loop - The outer loop, or OFG, must provide the additional dynamic range to allow the two-loop system to operate over the specified range of ±64,000Y. It accomplishes this by sampling the converted digital output of the inner loop to determine whether it is within either the bottom or top one-eighth of full scale (or in between) at a sample rate of approximately 0.5 Hz. If within either of the outer octants, the sample pulse either increments or decrements a six-bit reversible counter in the OFG logic. If within the interior 75 percent of the ADC range, the counter state is not changed.

The output of the reversible counter is input to a six-bit DAC where the output is converted to a feedback current in the current generator.

The system parameters are selected so that each step of the OFG is equivalent to 2500Y. Thus, after each increment, a hysteresis of approximately 500Y exists to ensure that the occurrence of OFG step changes is minimized.

Typical input/output curves for increasing and decreasing inputs are shown in Figure 5-5. An obvious secondary advantage of this two-loop system is that a cross calibration between the ADC and the OFG is provided.

Operating Range - With the selected parameters, this system is capable of operating over a range of -80,000Y to +81,500Y; however, if desired, the logic could limit the up/down counter range to a limit of approximately ±64,000Y.

Summary - We have now described the general characteristics of the single and the two-loop systems, which show that each has its advantages and disadvantages. Further analysis of frequency characteristics and errors for a non-steady state field follow in order to select a system for detail design.

TABLE 5-1. COMPARISON OF INNER-LOOP OF TWO-LOOP SYSTEM WITH SINGLE-LOOP SYSTEM

Parameter	Two-Loop Inner Loop	Single-Loop System
Input Range	0 to 4000Y	±64,000Y
Output Range	0 to 9.6V	±9.6V
Input Resolution	±1.0Y	±1.0Y
Output Resolution	$\pm 2.4 \times 10^{-3}$ V	$\pm 0.15 \times 10^{-3}$ V
Bandwidth	25 Hz	25 Hz
Feedback Gain	4.167×10^{2} Y/V	6.67×10^{3} Y/V

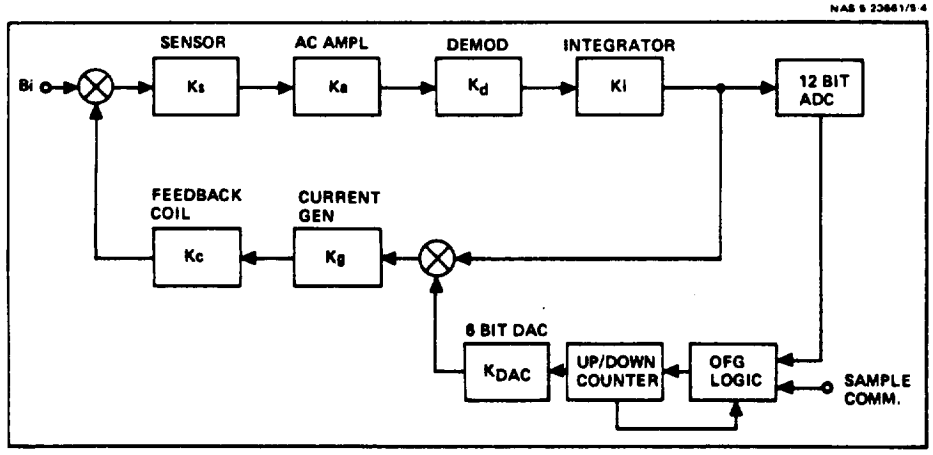

Figure 5-4. Two-Loop System. The two-loop system requires a 12-bit ADC with a 6-bit DAC in the outer feedback path.

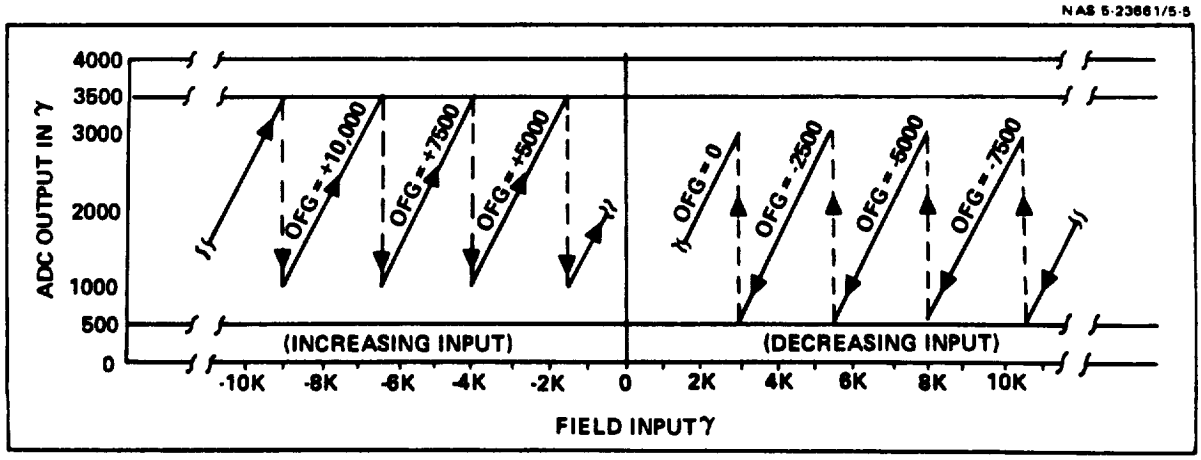

Figure 5-5. Typical Input/Output Curves for Increasing and Decreasing Inputs. The OFG has switching levels of 500 and 3500Y and hysteresis of 500Y.

FREQUENCY ANALYSIS OF THE SINGLE-LOOP SYSTEM AND INNER LOOP OF TWO-LOOP SYSTEM

Although the single-loop system transfer function is similar to that of the inner loop of the two-loop system, because of a shorter integrator time constant the two-loop system recovers more quickly from overload conditions.

The frequency analysis of the single-loop system is also applicable to the inner loop of the two-loop system. Its response is critically damped and is -3 dB at 25 Hz. The overload recovery time of the single-loop system is much longer than that of the two-loop system.

The equations expressing the frequency response characteristics of the single-loop system are shown in Table 5-2. Equation (8) expresses the basic transfer function of any closed-loop system, while Equations (9) and (10) relate the forward and feedback gains to the specific blocks described in the previous topic.

After making the notational simplifications shown, Equation (11) gives the exact closed-loop response of the system. At this point in the analysis a simplifying assumption was made based on the assumed values of the time constants shown. The selected value gives a ratio of this inequality of approximately one to 1600, which certainly justifies its use.

The resulting Equation (12) can be factored, giving the final result shown in (13).

Analysis Methodology - It should be noted that the actual sequence of synthesizing the loop parameters was approximately the reverse of the order of the equations. The system response was selected for critical damping with a -3 dB frequency response at 25 Hz, giving Equation (13). The topology (shown previously) was selected based primarily on experience with other similar systems. The values of K_s, K_a, K_d, and τ_a were set by considerations described previously. The factors β and τ_c were dictated by the required dc response and coil design, respectively.

The two free parameters left were the integrator and the demodulator filter time constants. The final exercise left was to calculate these values.

Inner Loop of Two-Loop System - The transfer function of the inner loop of the two-loop system is exactly the same form as that of Equation (13). The only difference in values is of K_f, the dc feedback gain, which, in turn, gives a different value of τ_i, the integrator time constant, since τ_x and K_x are constants for both systems.

Comparison of Loop Time Constants - Based upon the preceding paragraph and using values of 8.73×10^{-3} seconds for τ_x and 10^{-2} for K_x, the calculated value of τ_i for the single-loop system is 0.582 second. Using a feedback gain of 417 V/V for the two-loop system, its integrator time constant is 0.036 second.

These values indicate that the two-loop system with its much shorter integrator time constant will recover from overload conditions much more quickly than the single-loop system.

We now analyze the errors of the described system for non-steady state input fields.

TABLE 5-2. EQUATIONS FOR EXPRESSING THE FREQUENCY RESPONSE CHARACTERISTICS OF THE SINGLE-LOOP SYSTEM

The loop parameters are selected from the desired closed-loop response of Equation (13).

$$A_c = \frac{A_o}{1 + \beta A_o} \tag{8}$$

$$A_o = \frac{K_s K_a K_d}{\tau_i s (1 + \tau_a s)(1 + \tau_d s)} \tag{9}$$

$$\beta = \frac{K_g K_c}{(1 + \tau_c s)} \tag{10}$$

K_d = demodulator gain
τ_d = demodulator time constant
K_g = current generator gain
A_c = closed-loop gain
A_o = forward open-loop gain
β = feedback gain
K_s = sensor gain
K_a = ac amplifier gain
τ_a = ac amplifier time constant
τ_i = integrator time constant
τ_c = coil time constant
K_c = feedback coil gain

Letting: $K_f = K_g K_c$, $K_x = K_s K_a K_d$, $\tau_x = \frac{\tau_i}{K_x K_f}$

$$A_c = \frac{1}{K_f}\left[\frac{(1 + \tau_c s)}{1 + \tau_x s + \tau_x(\tau_a + \tau_d + \tau_c)s^2 + \tau_x(\tau_a\tau_d + \tau_a\tau_c + \tau_d\tau_c)s^3 + \tau_x\tau_a\tau_d\tau_c s^4}\right] \tag{11}$$

Under the conditions that: $\tau_c^2 << \tau_x(\tau_a + \tau_d)$

$$A_c \approx \frac{1}{K_f}\left[\frac{1}{1 + (\tau_x - \tau_c)s + \tau_x(\tau_a + \tau_d)s^2 + \tau_x\tau_a\tau_d s^3}\right] \tag{12}$$

$$\approx \frac{1}{K_f}\left[\frac{1}{(1 + \tau_1 s)^2 (1 + \tau_2 s)}\right] \tag{13}$$

Where $\tau_1 = 4.07 \times 10^{-3}$ sec and $\tau_2 = 0.48 \times 10^{-3}$ sec.

ERROR ANALYSIS OF THE SINGLE-LOOP SYSTEM AND INNER LOOP OF TWO-LOOP SYSTEM

The errors for non-steady state fields were not specified but were considered worthy of analysis. These errors were the same for both systems.

Errors for non-steady state fields dominate the dc error for frequencies above 3 Hz. The lag for ramp inputs is also analyzed. Both errors are applicable to the single-loop system and the inner-loop of the two-loop system.

As the frequency of the input field increses, the loop gain (βA_o) decreases, giving rise to increasing errors due to uncertainties in the open-loop parameters.

Equation (12) from the previous topic was used for the error analysis. The magnitude of the gain ($|A|$) was calculated, from which the partial derivatives of Equations (14) were derived.

$$\frac{d|A|}{|A|} = \left[\frac{1}{|A|}\left[\left(\frac{\partial|A|}{\partial\tau x}\,d\tau x\right)^2 + \left(\frac{\partial|A|}{\partial\tau_a}\,d\tau_a\right)^2 + \left(\frac{\partial|A|}{\partial\tau_d}\,d\tau_d\right)^2 + \left(\frac{\partial|A|}{\partial\tau_c}\,d\tau_c\right)^2 + \left(\frac{\partial|A|}{\partial K_f}\,ddK_f\right)\right]\right]^{1/2} \tag{14}$$

The RSS error was then calculated as a function of frequency. Equation (15) was required to relate $d\tau_X$ to the circuit parameters from which it was derived.

$$d\tau_x = \left[\left[\frac{\partial\tau_x}{\partial\tau i}\,d\tau i\right]^2 + \left(\frac{\partial\tau_x}{Ks}\,dK_s\right)^2 + \left(\frac{\partial\tau_x}{\partial K_a}\,dK_a\right)^2 + \left(\frac{\partial\tau_x}{\partial K_a}\,dK_a\right)^2 + \left(\frac{\partial\tau_x}{\partial K_f}\,dK_f\right)\right]^{1/2} \tag{15}$$

Each of the partial derivatives, which are all functions of powers of ω, were calculated for the frequencies shown in Table 5-3. The individual error terms were then derived and RSS'd to give the ac error terms shown in the table.

The dc error term is simply the expected error in K_f, the dc component of the feedback gain, β. The derivation of this error is discussed in a later topic describing the current feedback amplifier.

It can be seen from the data in Table 5-3 that the dc error term dominates the total error through a frequency of $\omega = 1.0$. The ac error term then becomes predominant and increases to about 6 percent at 25 Hz ($\omega = 157$) and to almost 10 percent for higher frequencies.

The largest factors in the ac error terms are those caused by the estimated 5 percent uncertainties in the sensor and ac amplifier gains.

Ramp Input Error - Using Equation (13) from the previous topic and letting the field input be in the form of a ramp ($Bi(s) = B/s^2$), one can calculate the offset error for any ramp input. The result is that

$$B(\text{offset})\gamma = 8.6 \times 10^{-3} \times Bi\left(\frac{\gamma}{\text{sec}}\right) \tag{16}$$

Using this equation, the offset error due to the maximum expected ramp input of 250 γ/sec is 2.15γ.

The frequency and ramp errors described above also apply to the inner loop of the two-loop system.

TABLE 5-3. PARTIAL DERIVATIVES FOR VARIOUS FREQUENCIES

The ac error dominates for frequencies above 3.0 radians/sec.

Frequency Radians Per Sec	AC Gain Error	DC Gain Error	Total RSS Error
10^{-2}	4.2×10^{-10}	2×10^{-5}	2.0×10^{-5}
10^{-1}	4.2×10^{-8}	2×10^{-5}	2.0×10^{-5}
1.0	4.2×10^{-6}	2×10^{-5}	2.0×10^{-5}
3.0	3.8×10^{-5}	2×10^{-5}	4.3×10^{-5}
10	4.2×10^{-4}	2×10^{-5}	4.2×10^{-4}
30	3.7×10^{-3}	2×10^{-5}	3.7×10^{-3}
10^{2}	3.3×10^{-2}	2×10^{-5}	3.3×10^{-2}
157	5.8×10^{-2}	2×10^{-5}	5.8×10^{-2}
300	8.7×10^{-2}	2×10^{-5}	8.7×10^{-2}
103	8.4×10^{-2}	2×10^{-5}	8.4×10^{-2}
3×10^{3}	8.9×10^{-2}	2×10^{-5}	8.9×10^{-2}
104	9.5×10^{-2}	2×10^{-5}	9.5×10^{-2}
3×10^{4}	9.6×10^{-2}	2×10^{-5}	9.6×10^{-2}

SUMMARY OF TWO-LOOP SYSTEM DESIGN PARAMETERS

The two-loop system design parameters are established to enable allocation of errors. The estimated steady-state errors from the resulting analyses meet the requirements.

The frequency stability of the two-loop system has been discussed along with its general topology and operation. The ability to meet the specified performance must now be established.

Electronic Error Budget - Table 5-4(a) shows the overall budget of errors allocated to the electronics subsystem. The following topics of this subsection will address the sources of these errors and estimate their magnitude. The analysis will be performed assuming steady-state (or dc) conditions, since the unspecified frequency-dependent instabilities were addressed previously.

Summary of the Error Analysis - The summary of the following error analyses is shown in Table 5-4(b). As indicated, the errors were calculated for long-term (one year) drifts and for temperature drifts assuming both no control (±30°C) and for a controlled environment of ±5°C for critical components.

Comparison of the results versus the requirements shows that the overall electronics system is capable — but just barely — of meeting the requirements without a temperature controlled environment for the critical components. Therefore, it is strongly recommended that a thermal controller be used. This will provide a margin of safety and will also ensure that moisture is not alllowed to affect the Vishay resistors, which could cause an additional 20 ppm per year of long-term drift.

Data Requirements - It might appear that the data requirements of the two-loop system (12 + 6 bits) are greater than that required for a single-loop system with the same resolution (17 bits); however, the six-bit DAC need only be sampled for incrementing and read out approximately once every two seconds, assuming a maximum input rate of 200 γ/second. Thus, if the desired sampling rate were 8 samples per second, the single-loop system would require 8 x 17 = 136 BPS while the two-loop system would need only 8 x 12 + 6/2 = 99 BPS. This is a significant saving in telemetry space and an additional argument for the two-loop system.

TABLE 5-4. SUMMARY OF TWO-LOOP SYSTEM ERROR BUDGET

All error budgets can be met with temperature control except for a slight overcondition on long-term zero offset.

(a) Error Budget

Source	Long-Term	Temperature	Total
Zero Offset	0.33 γ/year	0.33γ	0.47
Linearity	–	0.1γ	0.10
Scale Factor	2.5 γ/year	2.5γ	3.54
RSS Total	2.52γ	2.52γ	3.57γ

(b) Error Analysis (Errors in γ)

Source	Long Term	Temperature ±30°C	Temperature ±5°C	Total ±30°C	Total ±5°C
Zero Offset					
Demod/Int	0.05	0.05	0.05(1)	0.07	0.07(1)
DAC	0.25	0.30	0.05	0.39	0.26
Current Gen.	0.24	0.27	0.05	0.36	0.25
Zero Offset Total	0.35	0.41	0.09	0.54	0.37
Scale Factor					
Loop Non-lin.	0.001	0.001	0.001(1)	0.002	0.002(1)
Loop Gain	0.008	0.003	0.003(1)	0.009	0.009(1)
ADC	0.15	0.08	0.08(1)	0.17	0.17(1)
DAC	0.9	2.1	0.35	2.3	0.97
Current Gen	0.26	2.1	0.35	2.1	0.44
Scale Factor Total	0.95	2.97	0.50	3.0	1.1
Total Accuracy	1.0	3.0	0.51	3.0	1.2

(1) These circuits not temperature controlled.

DESIGN OF THE REFERENCE GENERATOR AND THE PROBE DRIVE

The recommended probe drive circuit uses a crystal oscillator with a digital count-down chain and reference phase adjustment. The probe drive provides high efficiency operation.

The probe drive circuit and reference generator were determined to be areas where high confidence in many proven solutions existed. The probe design calls for an excitation frequency of 10 kHz, which is comparable to many existing designs.

Requirements - The general requirements of this subsystem include good frequency stability, easy phase adjustment between the probe drive and the demodulator, 2fo, reference signal, and an efficient probe drive with good symmetry to minimize even harmonics.

A Solution - The schematic of Figure 5-6 shows one method for generating the probe drive signal and the demodulator reference voltage which meets these requirements.

As shown, a 2-MHz crystal oscillator is used to generate a stable frequency. Its output is counted down in devices which provide decoded decimal outputs. Proper selection of one of the R lines and one of the C lines enables setting the relative phases of drive and reference signals to about two degrees. The properly phased signals from the countdown chain are divided once more to generate the probe drive reference.

The circuit used to generate the probe drive current is one which has been used with the MJS Spacecraft Magnetometer System described by M. Acuna*, and is frequently used to drive magnetic amplifiers. This circuit has the advantage of providing a large ratio of peak-to-average current resulting from the discharge of the capacitor into the core when it saturates; it exhibits high efficiency because the drive circuit supplies only circuit losses. The nonlinear resonant circuit provides energy storage. The digital drive generator has the advantage that the required odd symmetry of the square wave voltage is easily accomplished at these frequencies with CMOS logic elements.

Redundancy - It is planned that each of the three axes will have identical circuit boards, including the reference generators. Additional studies should be performed on the total system reliability to determine the best way of using the available redundancy of the three oscillators.

Next we describe the second harmonic amplifiers of the inner loop.

*M. H. Acuna, IEEE Transactions on Magnetics, Vol. MAG-10, 519 (1974).

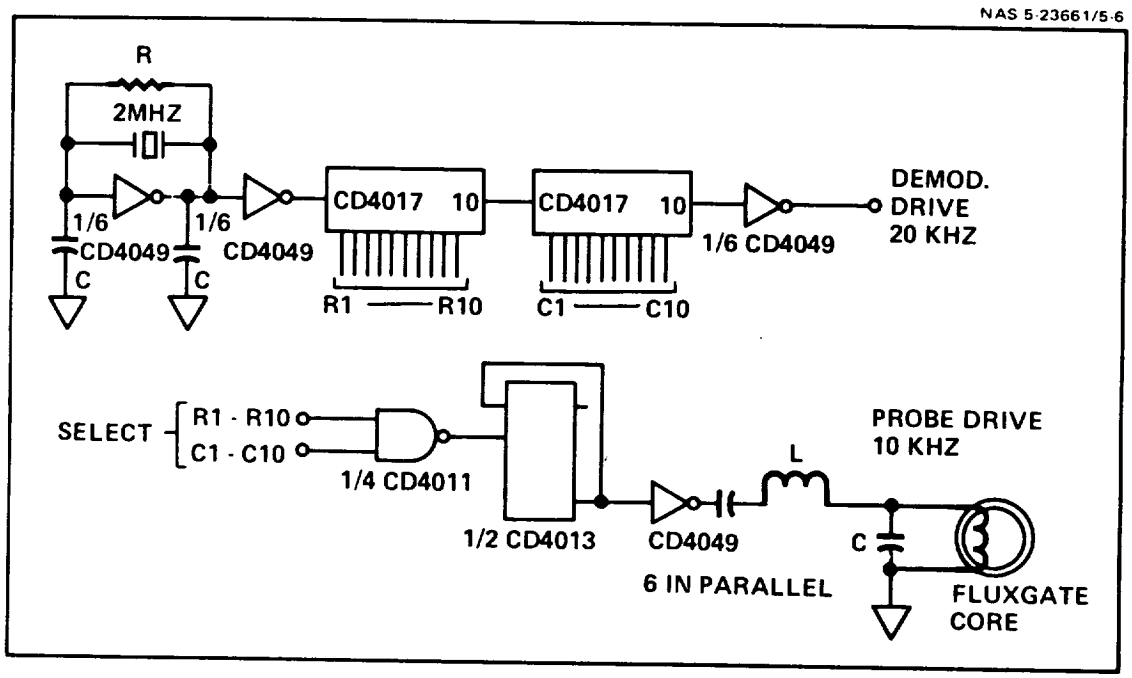

Figure 5-6. Reference Generator and Probe Drive. This design uses a crystal oscillator for stability and a high-efficiency drive circuit.

DESIGN OF THE SECOND HARMONIC AMPLIFIER

As with the probe drive circuit, the implementation of the second harmonic amplifier is amenable to proven solutions.

The second harmonic signal generated in the fluxgate probe contains the magnetic field information and must be amplified in the presence of large odd harmonic components which are coupled across the core.

Requirements - The amplifier must be tuned to the second harmonic signal, providing a gain of about 4×10^3 and a high rejection of the fundamental and third harmonics; it must not create significant noise relative to that generated in the probe (less than 0.03 γ rms); and it must be designed so that overload conditions (which will certainly exist at turn-on) do not cause excessive phase shifts due to hard limiting.

A Solution - As might be expected, a large number of solutions to these requirements have been implemented for previous space programs (including those designed at TZL). A recommended solution is shown in the simplified schematic of Figure 5-7. This circuit provides passive gain and tuning in the input circuit. C1 is selected to provide series resonance with the probe secondary winding inductance. The values shown provide a Q of about 5 for this resonant circuit and are large enough to swamp the stray cable capacity.

The input transformer is selected to provide a voltage gain of about 20. This value was selected on the basis that the secondary capacitance, C2, should not be less than 30 pF to ensure minimum changes due to stray capacities, including the amplifier input capacity. The capacity reflected into the primary is therefore about 0.012 μF. The transformer inductance is tuned for parallel resonance with the total secondary capacitance.

Having achieved a passive gain of 20, the additional gain required is about 200. This can easily be provided by two stages of gain with a tuned filter coupling them.

Both amplifiers should contain controlled limiting characteristics to ensure, under overload conditions, that the phase shift through the amplifier does not become excessive.

Noise - A reasonable estimate of noise at the input of the amplifier is about 30 $nV/\sqrt{Hz}$. Assuming a bandwidth of about 600 Hz, this represents an input noise of approximately 0.73 μV which, when reflected through the input transformer and the sensor scale factor, results in an equivalent magnetic field noise of somewhat less than 0.01 γ rms, which meets the system requirements.

Next we describe the demodulator and integrator which convert the second harmonic signal to dc and provide additional gain.

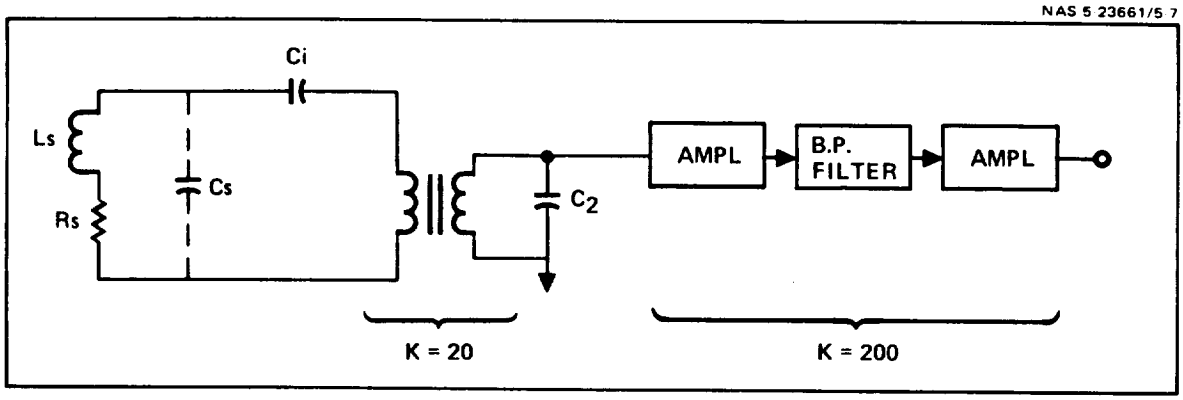

Ls = SENSOR INDUCTANCE ($\approx 376 \times 10^{-6}$)
Rs = SENSOR RESISTANCE ($\approx 9.2\ \Omega$)
Cs = CABLE CAPACITANCE (≈ 300 pf)
C1 = CAPACITANCE TO RESONAT WITH Ls ($\approx 0.168\ \mu$f)
C2 = SECONDARY TUNING CAPACITOR (≈ 30 pf)

Figure 5-7. Second Harmonic Amplifier. Provides passive gain and tuning in the input circuit.

DESIGN OF THE DEMODULATOR AND INTEGRATOR

The demodulator synchronously converts the second harmonic output to a dc signal which is amplified by an operational amplifier configured as an integrator.

The simplified schematic of Figure 5-8 shows the basic configuration of a demodulator and integrator which meet the system requirements.

Demodulator Configuration - The demodulator configuration shown, although utilizing only one switch, has a gain given by

$$\frac{e_o \text{ dc}}{e_i \text{ peak}} \approx \frac{2}{\pi} \times \frac{R_2}{R_1 + R_2} \tag{1}$$

under the conditions that

$$R_1 C_1 \gg t$$

and

$$R_2 C_2 \gg t$$

where $t = \frac{\pi}{\omega}$

Thus, it provides the same output voltage as most full-wave demodulators. Many switches are available, including the Harris HI 5049, which has previously been successfully used in this type of application.

Integrator - Following the demodulator is an integrator which is mechanized with an LM-108 operational amplifier. This circuit provides the high loop gain necessary to ensure minimal non-linearity and scale factor drift.

The transfer function of the integrator is

$$-\frac{e_o}{e_i} = \frac{K_d}{\left(1 + K_d \tau_i s\right)\left(1 + \frac{\tau_a}{k} s\right)} \approx \frac{1}{\tau_i s} \tag{2}$$

where

K_d = DC gain of the op-amp ($\approx 3 \times 10^5$)

τ_i = Integrator time constant (≈ 0.036 sec)

τ_a = Corner frequency of the operational amplifier compensation (≈ 0.2 sec)

As indicated, the transfer function is really that of a dc amplifier with two poles. One pole is due to the external components, R_3 and C_3, and the other pole is due to the amplifier compensation.

Since K_d has a nominal value of 3×10^5, using the time constants shown, the corner frequencies equivalent to the poles are about 1.5×10^{-5} Hz for $K_d \tau_i$ and 2×10^5 Hz for τ_a / K_d. The approximation shown is therefore valid for any analysis except for dc stability.

Errors - The required 1.0×10^{-3} Vdc stability at the input of the demodulator and integrator is easily achievable with the selected components.

An assumed short term drift in K_d of ±50 percent and a long term drift of -300 percent give rise to scale factor errors of 3×10^{-3}Y and 8×10^{-3}Y, respectively. Assuming a non-linearity of 20 percent in K_d results in an error (for the minimum expected value of K_d) of less than 1×10^{-3}Y in the system closed-loop gain.

In summary, the integrator and demodulator mechanization is straightforward. The errors produced are negligible compared to other sources such as the feedback current generator. The output of the integrator is converted to a digital signal by the ADC, which is described in the following topic.

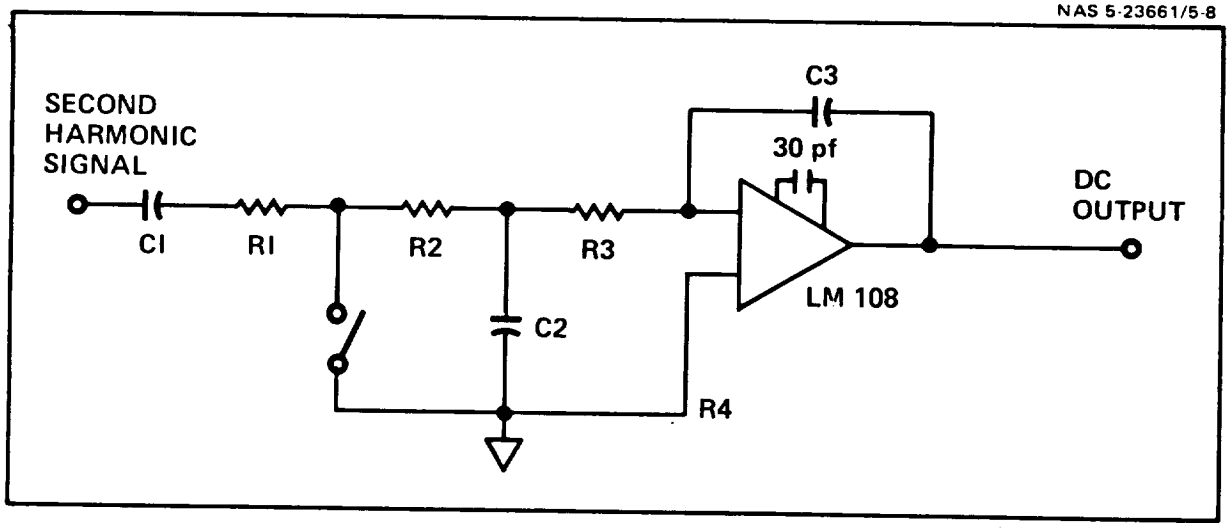

Figure 5-8. Demodulator-Integrator Design. This simple, straightforward design meets all system requirements.

DESIGN OF THE 12-BIT ADC

The ADC design is a dual-slope integrating type. This is a proven technique which results in small error contributions and also eliminates offset errors.

The ADC converts the analog output from the loop integrator to a digital signal. The overall system was designed to simplify this circuit by necessitating that only positive inputs from zero to 10 V be converted. Twelve-bit conversion was selected so that the digital output would contain a fair measure of the system noise to allow its evaluation. This approach, of course, also reduces the resolution error from the required ±1.0Y to half that value.

Recommended Solution - The schematic shown in Figure 5-9 shows the recommended implementation of the ADC. This system is a dual-slope integrating type ADC with the feature that an additional cycle is added which measures the system offset and subtracts it from the digital output data.

Four subcycles of the system operation are used — each requires a time equivalent to 4096 clock periods, where the clock period is approximately 2 μs. The conversion thus requires about 32 ms.

At the beginning of the first period, S4 is opened and S1 closed. The integrator output, at the end of 8 ms, is proportional to the offset voltage, V_{01}. This offset is adjusted to ensure that the polarity of the offset is equivalent to a positive input.

During the second period, S1 is opened and S2 is closed, applying the reference voltage to the input. Clock pulses are then counted into the logic system until the comparator fires. This count, N_2 of Equation (1), is a measure of the total offset voltage.

During the third period, S3 is closed, thus integrating the total value of $(V_i + V_{01})$ for 4096 counts.

Finally, in the fourth period, S2 is again closed while clock pulses are counted in the logic until the comparator threshold is again reached (note that the comparator fires twice — both times in the same direction, eliminating hysteresis and timing problems). The count stored in N_4 is shown in Equation (2).

The logic subtracts N_2 from N_4, giving a total count N_t, as shown in Equation (3). The two important characteristics of this equation are that the offset voltage of the comparator, V_{02}, has been eliminated from the output count and that the integrator offset has been converted to a scale factor error.

System Errors - Table 5-6 shows an estimate of the system errors, including those of the reference voltage (which is described in the DAC section) and the integrator. The total RSS error expected for both temperature and long-term drift is approximately 0.2Y.

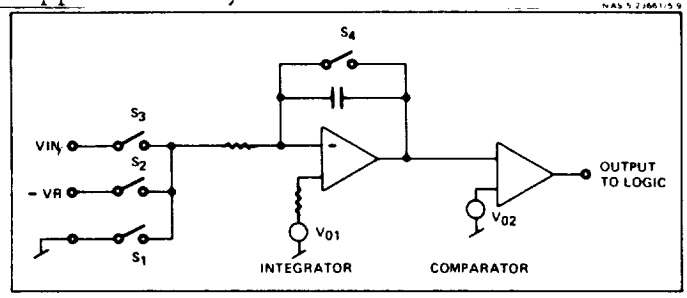

Figure 5-9. Design of the 12-bit ADC.

TABLE 5-5. DETERMINATION OF OUTPUT COUNT

The equations show that the comparator offset voltage is cancelled and the integrator offset causes a scale factor error.

$$N_2 = \frac{V_{01}N}{(-V_R + V_{01})} - \frac{\tau}{\Delta t}\frac{V_{02}}{(-V_R + V_{01})} \quad (1)$$

$$N_4 = \frac{(V_i + V_{01})N}{(-V_R + V_{01})} - \frac{\tau}{\Delta t}\frac{V_{02}}{(-V_R + V_{01})} \quad (2)$$

$$N_t = N_4 - N_2 = \frac{N\,V_i}{(-V_R + V_{01})} \quad (3)$$

N_2 = Counts for offset
N_4 = Counts for input plus offset
N_t = Output count
N = Full scale count (4096)
Δt = Converter clock period
V_{in} = Input voltage
V_{01} = Integrator Offset
V_{02} = Comparator offset
V_R = Reference voltage
τ = Integrator time constant

TABLE 5-6. ADC SYSTEM ERRORS

The ADC errors are minor with no temperature control.

(a)

Source	Scale Factor Error PPM/°C	PPM/yr
Voltage Ref	1.0	12.5
Integrator V_{os}	0.1	2.0
Integrator i_{os}	0.4	12.0
Sw Res γ_{os}	0.5	10.0
Sw Time t_{sw}	0.01	0.2
RSS Total (PPM)	1.2	20.1
RSS γ	0.005 γ	0.08 γ

(b)

Error Source	Error γ No Temp Control ±30°C
Scale Factor Temp	0.15
Scale Factor Long Term	0.08
RSS Total	0.17 γ

DESIGN OF THE FEEDBACK CURRENT GENERATOR

The outputs of both inner and outer loops are summed and converted to a current for the feedback coil. Temperature control of the critical components is required.

The magnetometer system stability is directly proportional to the stability of those elements in the feedback loop which include the current generator. A simplified schematic of this circuit is shown in Figure 5-10.

The system consists of a two-stage voltage summing amplifier which accepts the outputs of the inner and outer loops and scales them properly, and a two-stage current generator which converts its input voltage to a current through a scale factor equal to the resistor, R1.

Two stages of gain were used for both the summing amplifier and the current generator to ensure negligible errors due to gain drift and nonlinearities in the operational-amplifiers. Precision Monolithic Op-07 amplifiers are used in both input stages due to their extreme stability. This device was also used in the current generator output stage due to its current output capability (8 mA full-scale current is assumed).

The precision resistors required are R1 through R4. These would be mechanized using Vishay precision film components, which experience has shown to be highly reliable and stable.

Standard non-precision resistor-capacitor networks are used to stabilize both loops, with one series network used across the coil. The only significant pole in this circuit is that due to the L/R feedback coil constant, which is 0.11×10^{-3} second.

Component Instabilities - The component instabilities which were utilized in the error analysis are shown in Table 5-7.

Error Analysis - Using the value of Table 5-7 an analysis was performed to determine offset and scale factor errors, which are temperature dependent both with and without a temperature controlled environment, and long-term errors. The results of this analysis are shown in Table 5-8(a) and (b).

As indicated, the total inaccuracy of the current generator, both long and short term, for scale factor and zero offset, are reduced by a factor of four if the critical components are kept in a temperature controlled environment of ±5°C. This is highly recommended to provide a margin of error and also to eliminate moisture from entering the components if the thermal environment is hermetically sealed and evacuated.

The other critical element in the feedback path is the DAC of the outer loop, which is described next.

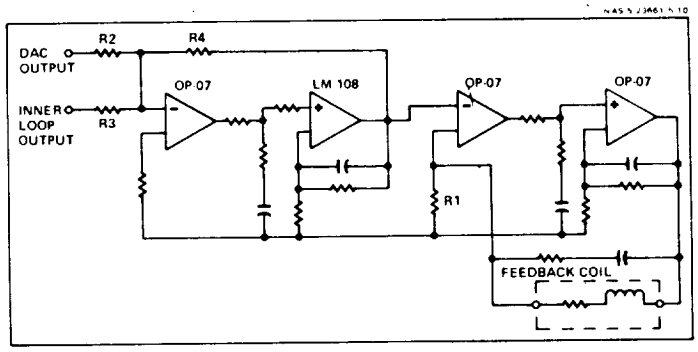

Figure 5-10. Feedback Current Generator. The circuit sums the voltage outputs of both loops and converts the sum to a feedback current.

TABLE 5-7. COMPONENT INSTABILITIES USED IN ERROR ANALYSIS

Source	Instability	
	Temperature	Long-Term
OP-07		
Offset Voltage	0.6 μV/°C	12 μV/year
Offset Current	25 pA/°C	700 pA/year(1)
Gain Error	10% over ±30°C	50%/year
Vishay Resistor		
Tracking	0.5 ppm/°C	3 ppm/year(2)
Absolute	1.0 ppm/°C	3 ppm/year(2)

(1) This was based on an assumed doubling of the offset current over a 5-year period.

(2) This assumes that the resistors will be hermetically sealed to eliminate a possible 25 ppm/year instability due to moisture.

TABLE 5-8. ANALYSIS OF OFFSET AND SCALE FACTOR ERRORS. The DAC errors are significantly reduced by a crude temperature controller.

(a)

Source	Scale Factor		Zero Offset	
	ppm/°C	ppm/yr	ppm/°C	ppm/yr
DAC Input R4/R2	0.47	2.8		
F.B. Input R3/R2	0.03	0.2		
S.F. Res. R1	1.0	3.0		
Z_1 Vos			0.2	3.0
Z_1 Ios			0.01	0.28
Z_1, Z_2 Gain	0.007	0.5		–
Z_3 Vos			0.12	2.4
Z_3 Ios			0.001	0.03
Z_3 Gain	0.001	0.15		–
RSS Total (ppm)	1.1	4.1	0.23	3.9
RSS Totalγ	0.07γ	0.26γ	0.01γ	0.25γ

(b)

Error Source	Errors (γ)	
	No Temperature Control ±30°C	Temperature Control ±5°C
Scale Factor Temperature	2.1	0.35
Scale Factor Long-Term	0.26	0.26
RSS	2.1	0.44
Zero Offset Temperature	0.30	0.05
Zero Offset Long-Term	0.25	0.25
RSS	0.39	0.26
Total Accuracy RSS	2.14γ	0.51γ

DESIGN OF THE DIGITAL-TO-ANALOG CONVERTER (DAC)

As with the current generator of the previous section, the DAC is also in the feedback path and, therefore, must exhibit high stability. Simple temperature control of critical elements enhances performance.

The DAC accepts inputs from the Up/Down counter in the OFG logic and converts the 6-bit counter state to a corresponding precision voltage. The DAC output is then fed back to the feedback coil of the sensor through the previously described current generator. Each step is equivalent to 2500 Y.

Several DAC configurations were examined (see the next topic) and the one recommended is shown in the simplified schematic of Figure 5-11. It consists of two precision reference supplies (one of each polarity), a precision R-2R network, precision switches, and an output buffer amplifier. The principal reasons for selection of this topology are simplicity, symmetry, and the availability of suitable components.

Component Instabilities - As with the previously described current source, Op-07 amplifiers and Vishay resistors are used. The previous table showing the instability of these components is applicable. In addition, Harris HI 5049 switches and National LM-199 voltage references are used. Their instabilities are shown in Table 5-9 below.

Error Analysis - Using the value of Table 5-9, an analysis was performed to determine their effect on the subsystem performance. The results of this analysis are shown in Table 5-10 (a) and (b). As with the current generator, the results of temperature control are significant. Again it is recommended that this be used to maximize the probability of a successful mission.

The DAC described above is only one of several configurations which were investigated. Two alternative methods of providing this function are described in the next topic.

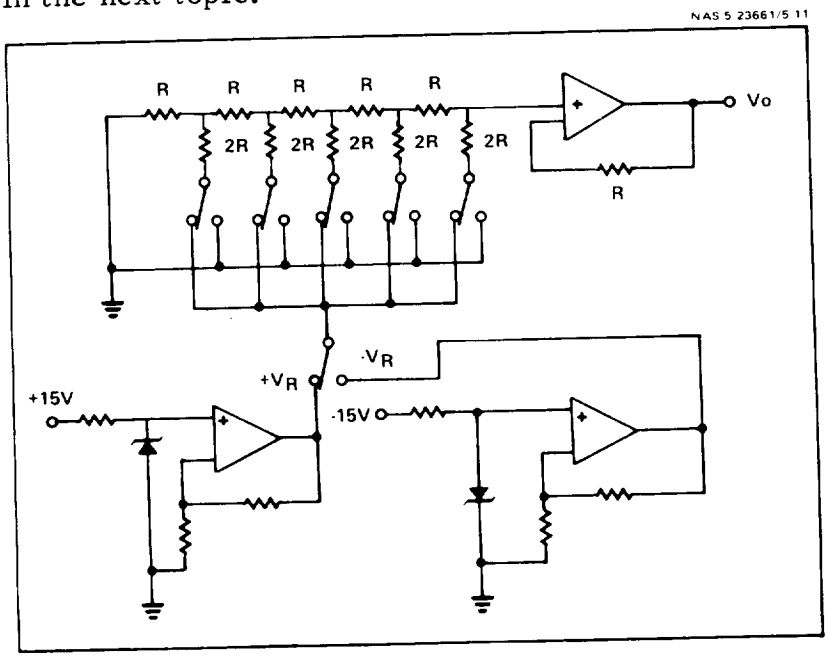

Figure 5-11. Digital-to-Analog Converter (DAC). The DAC configuration uses precision R-2R network and two Reference Supplies.

TABLE 5-9. COMPONENT INSTABILITIES USED IN ERROR ANALYSIS. The instabilities of the additional components used in the DAC are shown.

Source	Instability	
	Temperature	Long Term
Switch		
ON resistance	0.05 Ω/°C	1.0 Ω/year
OFF leakage	1.8 na/°C	31 na/year
Zener voltage	0.5 ppm/°C	12 ppm/year

TABLE 5-10. ANALYSIS OF OFFSET AND SCALE FACTOR ERRORS. The error analysis shows that temperature control reduces errors about in half.

(a)

Source		Scale Factor		Zero Offset	
		ppm/°C	ppm/yr	ppm/°C	ppm/yr
Switch on Res.	r_{DS}	0.29	5.8	–	–
Switch Leakage	$I_{D\ off}$	0.07	0.9	–	–
R/2R Network		0.29	1.73	–	–
Z_1	V_{os}	–	–	0.06	1.2
Z_1	i_{os}	–	–	0.125	3.5
Voltage Ref	V_R	1.0	12.5	–	–
RSS Total		1.1	13.9	0.14	3.7
RSS Total γ		0.07γ	0.89γ	0.009γ	0.24γ

(b)

Error Source		Errors (γ)	
		No Temperature Control ±30°C	Temperature Control ±5°C
Scale Factor Temperature		2.1	0.35
Scale Factor Long Term		0.9	0.9
	RSS	2.3	0.97
Zero Offset Temperature		0.27	0.05
Zero Offset Long Term		0.24	0.24
	RSS	0.36	0.25
Total Accuracy	RSS	2.3γ	1.0γ

ALTERNATIVE DAC CONFIGURATIONS

Two alternative methods of implementing the DAC were investigated and are worthy of consideration for use – switched coils and pulse-width modulation.

Switched Coils - One configuration uses a constant current source which is passed through multiple coils, as shown in Figure 5-12. The output of the UP/DOWN counter is used as the control inputs for the coil switches via a ROM code converter. The key to this implementation is that the current can be passed through each coil in either direction or may bypass the coil completely. This ternary type system can be implemented with four coils of ratios 1, 3, 9, 9 to provide plus and minus 22 steps of OFG flux.

The switches can be mechanized by devices such as the Harris HI5049. The ON resistance of these devices is nominally 30 ohms, for a total of 240 ohms for the eight switches. A preliminary error analysis indicates that this resistance is non-critical, as in the leakage current of the OFF switch sections.

The primary disadvantages of this system, which precluded its recommendation for use, is that the number of wires required complicates the boom cable and also complicates the fabrication of the feedback coils. One method of easing the cabling problem would be to transfer serial data down the boom to a non-magnetic logic hybrid in the sensor assembly which would perform the required storage and decoding.

Pulse-Width Modulator - A second configuration which has merit is a DAC which utilizes pulse-width modulation. Figure 5-13 shows a simplified schematic.

This system generates a dc pulse of the proper polarity with constant amplitude and a width proportional to the contents of the UP/DOWN counter at a sample rate of about 700 Hz. This frequency was selected as the geometric mean of the loop bandwidth (25 Hz) and the 2fo frequency (20 kHz) to minimize the effect of ripple on system operation.

The errors for this system are very comparable to the recommended DAC with the additional error of about 1.0 ppm/°C due to drift in the switching transients. The primary reason, however, for not recommending this method is lack of experience with its operation.

Next we describe the auxiliary circuits, which are not part of the basic magnetometer but would be required in a full system implementation.

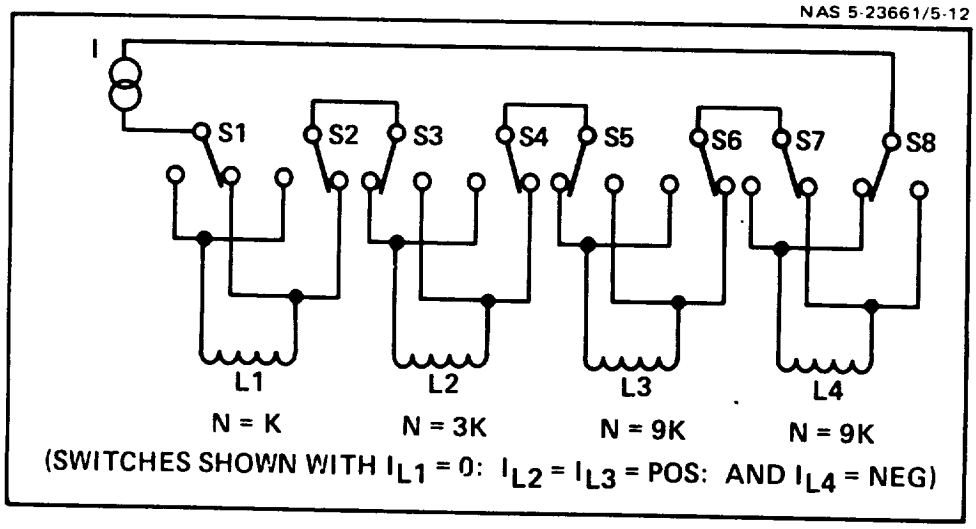

Figure 5-12. Constant Current Source. The current is applied through switched coil segments.

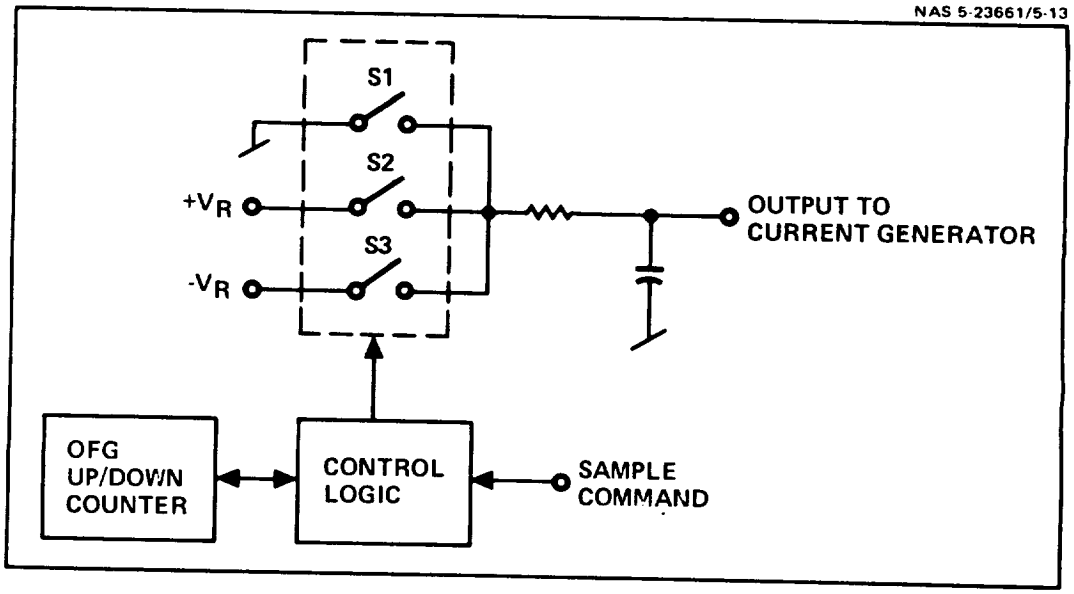

Figure 5-13. This DAC is basically a pulse-width modulator.

AUXILIARY SUBSYSTEMS AND POWER ANALYSIS

The basic magnetometer studied has been described. To perform overall weight and power estimates, the auxiliary subsystems must be included.

The simplified block diagram of Figure 5-14 shows the auxiliary circuits which will be required to mechanize the magnetometer system. They include the digital subsystems, interface circuits, a low voltage power supply, and temperature controllers. Each of these circuits has been investigated in sufficient detail to enable realistic power estimates and to allow an estimate of a typical mechanical configuration.

Logic and Telemetry Subsystem - The logic and telemetry blocks were sized assuming the use of CMOS logic elements throughout. It was assumed that the telemetry interfaces would be typical of other spacecraft and that the data would not have to be double buffered. Elements for system initialization were included. A total of 50 CMOS packages are required.

Temperature Controlling - One temperature controller is required for the sensor and is described elsewhere. An additional temperature controller for the critical components of the DACs and the current generators will require an estimated 0.7 W of power. The temperature control requirements are easily met since ±5°C is sufficient. An operating temperature of +85°C is assumed with a basic construction consisting of discrete elements mounted on a hybrid substrate which, in turn, is mounted in a hermetically sealed, evacuated housing to minimize heat leaks.

Low Voltage Power Supply - Many designs are available to meet the LVPS requirements. The LVPS should use switching techniques to provide efficiencies in the order of 75 percent. Post regulators are assumed on ±15 V analog lines to provide better than 0.5 percent regulation.

Power Estimate - Table 5-7 shows the estimated power breakdown. These estimates are considered realistic and, as indicated, enable the system to conform to the specified 6 W limit.

We next describe a method of packaging the entire system and give results of a weight analysis.

TABLE 5-11. POWER ESTIMATE.
The power estimate meets the specification.

Subsystem	Power (mW)
Sensor Drive (3)	216
AC Amplifier (3)	60
Demodulator (3)	30
Integrator (3)	30
ADC (12-Bit) (3)	525
DAC (6-Bit) (3)	405
Current Generator (3)	705
Reference Supplies (3)	195
Logic and Interface (1)	352
Temperature Controller (2)	1000
	3518
Low Voltage Supply at 75% Efficiency	1173
	4691

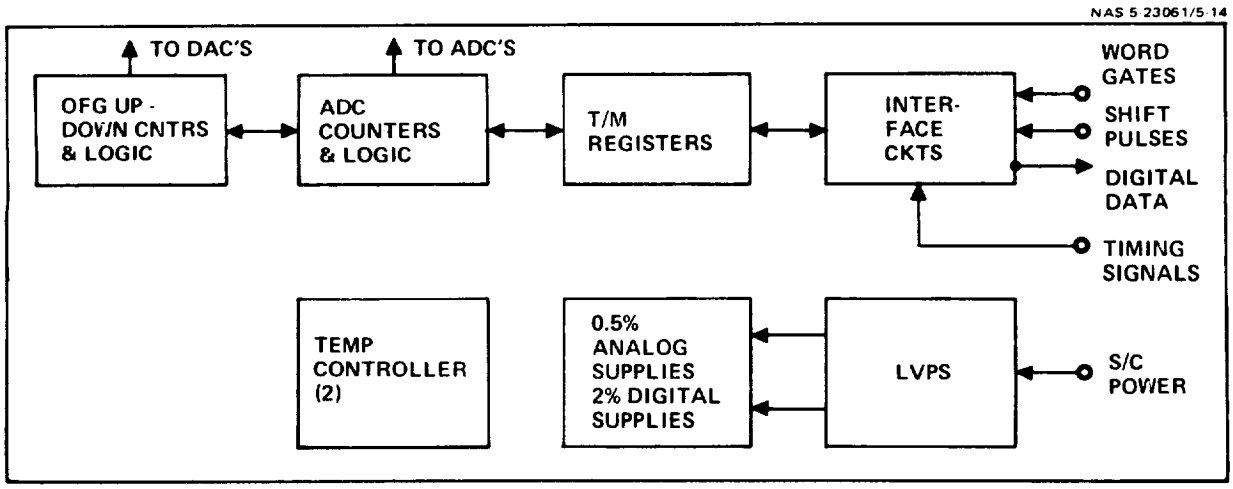

Figure 5-14. Auxiliary Circuits. Auxiliary circuits were included in weight and power analysis.

PACKAGING AND THERMAL CONTROL OF THE ELECTRONICS

A one-piece aluminum housing with a top access cover provides a structurally rigid, lightweight housing with good heat transfer characteristics.

The electronics must be designed to withstand shock and vibration and operate in a vacuum. The electronics housing must be lightweight, use space approved materials, and meet electrostatic and RFI requirements.

Structural Rigidity - The electronics housing is a high strength, aluminum alloy structure with a resonant frequency at least one octave higher than the circuit cards. The mounting of the circuit cards provides additional stiffening to the chassis. Resonant frequency of the circuit cards is about 200 Hz, with a Q of 14. With a 5 g input, this results in a maximum stress in a card equal to 1200 pounds per square inch, which is well below the allowable yield stress of 35,000 pounds per square inch for epoxy glass material.

Heat Transfer - Heat transfer within the electronics housing is by a combination of radiation (between circuit cards and between circuit cards and the aluminum case) and conduction (through the circuit card mounts and the aluminum case). The principal method of heat transfer from the electronics housing is through the aluminum case to the spacecraft shelf. With normal spacecraft surface specifications (63 microinch finish and 0.001 inch per inch flatness), a thermal resistance between the aluminum case and the spacecraft shelf of $R_i = 10^{o}C\text{-inch}^2/W$ can be expected. With an interface area equal to 30 square inches and a maximum dissipation of 5 W, the spacecraft to aluminum case temperature rise will be about $2^{o}C$.

Material Cleanliness Requirements - Materials selected for use will meet the low out-gassing requirements of 1% total weight loss and 0.1% volatile condensibles. All materials, with the exception of certain component leads and magnetics, have magnetic permeabilities of less than 1.02.

Electrostatic and RFI - The aluminum case will be chromate conversion coated, providing an electrically conductive mounting surface. The cover will fit in a groove in the case to provide a lap joint with a long path to avoid radiated noise. An internal RFI filter is used at the spacecraft interface connector for conducted noise.

Accessibility - Assembly of each circuit element into the case is facilitated by use of an internal harness. Because each circuit card size is identical, test setup is simplified.

Size and Weight - Overall housing size is 6 inches (15.24 cm) long by 5 inches (12.7 cm) wide by 3 inches (7.62 cm) high. Total weight is 2.25 pounds (1.02 Kg).

The electronics housing is designed to meet the requirements normally imposed on space flight hardware.

TABLE 5-12. DESIGN REQUIREMENT AND APPROACHES

Requirement	Approach
Structural Rigidity	- High cross section modulus. - High strength-to-weight ratio materials. - Additional support from circuit cards.
Good Heat Transfer	- Good thermal path from dissipating elements to heat sink. - Low thermal resistance from instrument base to spacecraft shelf.
Material Cleanliness	- Low outgassing. - Low magnetic permeability.
Electrostatic and RFI	- Electrically conducting case. - Line filters. - RFI-tight joints.

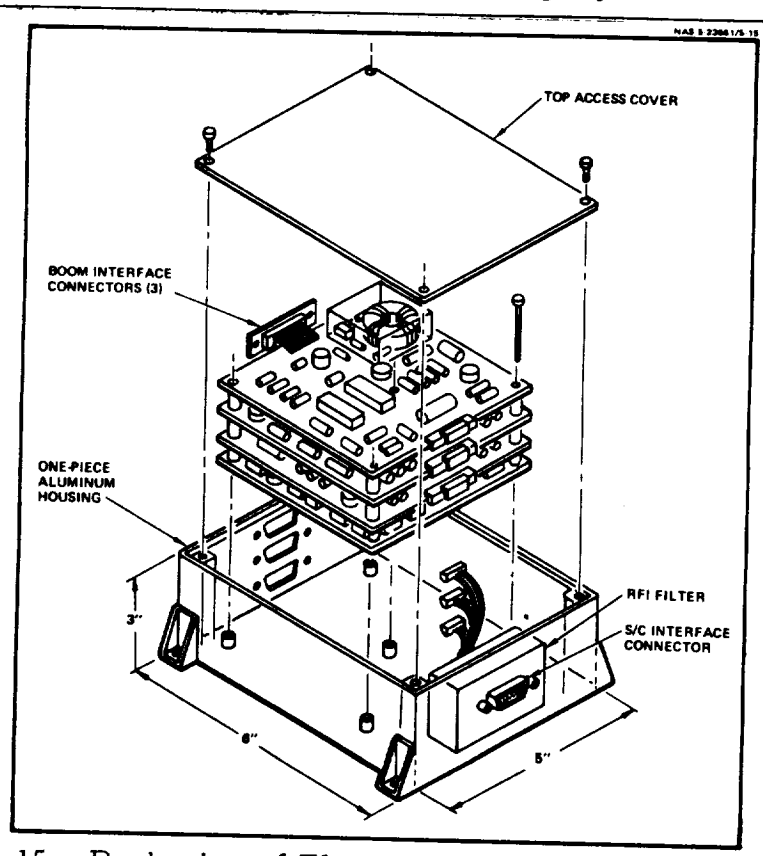

Figure 5-15. Packaging of Electronics. The instrument is designed to meet the requirements of space flight hardware.

SECTION 6
CALIBRATION AND ALIGNMENT

Nature of the Calibration and Alignment Problem 6-2
Identification of Contributions to Response Matrix 6-4
Determination of the Response Matrix 6-8
How Alignment is Determined 6-12
Summary of Accuracy and Equipment Requirements 6-14

NATURE OF THE CALIBRATION AND ALIGNMENT PROBLEM

The total specified overall accuracy of 5γ per vector field component for this instrument requires a stringent error budget limiting the contribution of each of the many potential sources of error. With individual sources necessarily small, their accurate determination becomes difficult.

The projected performance of this magnetometer substantially exceeds that of previous designs in stability and accuracy of alignment of the magnetic axes. This advance in the state of the art in magnetometers will require a commensurate advance in the techniques and instrumentation used to characterize and calibrate such sensors. The degree of precision sought in the determination of sensor parameters is in many cases as great or greater than that of the available measuring instruments.

The table opposite enumerates the primary sensor parameters that the calibration program must determine and the allowable errors attributed to each of them expressed in units of magnetic field.

Offset - The zero applied magnetic field output of the sensor is called offset and its maximum value and drift per year is specified at 0.4γ. Due to the presence of the earth's magnetic field, measurement of this parameter requires the generation of an opposing vector field to obtain a field-free volume near the sensor. Since any such cancellation procedure is likely to be imperfect, a gimbal mount for the sensor is also required to allow 180-degree rotations to remove the effects of any residual fields on the measurement.

Noise - The random fluctuations in output from a sensor in a steady field can readily be measured for a given bandwidth provided that a sufficiently quiet field environment can be supplied. Measurement of sensor noise of 0.3γ will require an environment that is an order of magnitude (0.03γ) quieter. The earth's magnetic field variations range in amplitude from a few γ at periods of 10-50 seconds to $\lesssim$1γ at periods of 2-8 seconds. A mu-metal flux tank can reduce ambient fields by several orders of magnitude; since variations scale the same way as amplitudes, adequately quiet fields can be achieved over periods of time of the order of one minute.

Scale Factor - The magnitude of voltage output due to a magnetic field applied parallel to a given sensor axis is subject to variation as a function of sensor operating temperature. The allowable error due to both initial uncertainty and stability over the operating environment is budgeted at 2.6γ. Since the scale factor determination involves knowledge of an output voltage and a magnetic field, both quantities must be measured to the required accuracy. For a maximum applied field of $6.4 \times 10^4\gamma$ the budgeted error represents 20 ppm which, equally distributed, allows 10 ppm errors from each source. Currently achievable accuracies in magnetic field measurement at GSFC are in the neighborhood of 16 ppm, and available potentiometric voltmeters have absolute accuracies of ~20 ppm. Statistical averaging of many readings will be needed to improve the precision of the measurements.

Linearity - In addition to varying with ambient temperature, the scale factor for each axis can vary as a function of the applied magnetic field magnitude. Such variations are budgeted to less than 2.6γ, the same as the accuracy specified at a given field, and the same considerations apply to this parameter. They can best be determined simultaneously with the magnitude of the scale factor by a least squares fit of data to a straight

line. The slope is then the scale factor and the deviation from it is the non-linearity for each magnetometer axis.

Axis Stability - The position of each magnetic axis may vary due to thermal and/or mechanical effects. The cone of uncertainty allotted to each axis is 5 arc-seconds, which, at maximum applied field, translates into an allowable error of ±1.6γ. In order to determine changes of orientation less than 5 arc-seconds, the precision of field and voltage measurements must be better than the 10 ppm specified for the scale factor determination. In order to eliminate the effects of changes in sensor output due to rotations of the complete sensor assembly relative to the applied field, the changes in orientation of the whole assembly must be monitored to the same or better precision as that desired in the final result. A system consisting of fixed autocollimators (theodolites) and optical reflectors mounted on the sensor assembly can fulfill this requirement.

Axis Orientation - In addition to measuring changes in orientation, the absolute position of at least two of the magnetometer axes must be defined to within one arc-second with respect to an optical reflector on the sensor package. This extremely stringent specification requires not only great accuracy of magnetic field and voltage measurements, but also knowledge of the absolute position of the test facility field axes to the same degree of accuracy (better than 1 arc-second). When last measured several years ago, the position of the GSFC test facility axes were determined to an accuracy of ~10 arc-seconds. It may be possible to improve on this measurement with a precision two-axis gimbal sensor mount. Such mounts presumably exist in high precision theodolites, but whether they can be modified to properly mount the magnetometer sensor is not known (they are likely to be made of ferrous metals).

The philosophy of defining separable sources of error and specifying the contribution of each to the desired total seems most likely of assuring reproducible performance within the overall requirements. Representing the response of the magnetometer to applied magnetic fields as a vector-matrix equation

$$\vec{V} = S\vec{B} + \vec{V}_o$$

the various contributions to the matrix S must be identified and separated. These contributions are discussed next.

TABLE 6-1. BUDGETED ERRORS

Parameters to be Determined	Budgeted Error
Offset	0.4γ
Noise	0.3γ
Scale Factor	2.6γ
Linearity	2.6γ
Axis Stability	1.6γ
Axis Orientation	0.3γ
	4.0γ Sensor Total
A-D Converter	3.0γ
	5.0γ Overall Total

IDENTIFICATION OF CONTRIBUTIONS TO RESPONSE MATRIX

The sensor response matrix operator can be decomposed into a sequence of linear transformations consisting of axis distortions and rotations. From these, the sensor scale factors and orientation can be determined.

The three output voltage components of the magnetometer can be considered to form a vector response to an applied magnetic field vector. For each sensor axis the output minus the offset voltage is proportional to the field component directed along that axis, with the "constant" of proportionality equal to the corresponding scale factor. That is $V_i - V_{io} = \lambda_i (\vec{B} \cdot \vec{i})$ where $\vec{i}$ is a unit length vector directed along the i-th sensor axis and λ_i is the i-th axis scale factor. Expressed in vector form, this is the instrument response equation shown in the table; the response matrix S contains the scale factors as well as the direction cosines describing the relative orientation of the sensor axes in the field. From measurements of sensor output voltage $\vec{V}$ and knowledge of a pplied field $\vec{B}$, S may be determined, but the various contributions to S must be identified and separated since the scale factors and axis orientations must be individually determined. The contributions are enumerated opposite.

Coordinate Systems - For the instrument response equation to be meaningful, vector components on both sides of the equation must refer to the same coordinate system. The choice of coordinates is arbitrary, but ultimately the calibration program must allow the determination of magnetic field components in the orthogonal "mirror" coordinate system from measured sensor output voltages. The "mirror" coordinate system is defined by sensor mounted mirrors which form a part of the optical attitude transfer system that will monitor boom twist and deflection in flight. Taking $\vec{V}$ to be composed of the three measured sensor output voltages and $\vec{B}$ the three known field components applied along the test facility axes, the matrix S is composed of a coordinate transformation from field axes to sensor axes followed by a scale factor transformation. The decomposition of the coordinate transform depends on the orthogonality and orientation of the two sets of axes.

Scale Factor Matrix - If sensor and field axes are both orthogonal and aligned with each other, then $(\vec{V} - \vec{V}_o) = E\,\vec{B}$ where E is a diagonal matrix whose elements are the three scale factors λ_i, i = 1, 2, 3 for the three axes.

Distortion Matrices - Neither the sensor axes nor the test facility field axes are necessarily orthogonal. If we denote the matrix operator that transforms an orthogonal set of axes into a distorted one by D, then the inverse transform, D^{-1}, transforms non-orthogonal axes into orthogonal ones. With the matrix for the sensor axes and field axes denoted by D_V and D_B, respectively, $D_V^{-1}(\vec{V} - \vec{V}_o) = E\, D_B^{-1} \vec{B}$ if the resulting orthogonal axes are aligned. The matrices D contain terms $d_{ij} = \vec{i} \cdot \vec{j}$ where $\vec{i}$ and $\vec{j}$ are vectors directed along the i-th and j-th axis, respectively. Since vector dot products are commutative, $d_{ij} = d_{ji}$ and the matrices are symmetric. If the distortions are small, the matrices are also nearly diagonal.

Rotation Matrices - The orthogonalized sensor axes are in general not aligned with the orthogonalized field axes. Representing the transform that expresses field components in the rotated orthogonal sensor coordinates by R_{BV}, $D_V^{-1}(\vec{V} - \vec{V}_o) = E\, R_{BV}\, D_B^{-1} \vec{B}$. Multiplying both sides of this equation by D_V, $(\vec{V} - \vec{V}_o) = D_V E\, R_{BV}\, D_B^{-1} \vec{B}$ and the response matrix S is equal to $D_V E R_{BV} D_B^{-1}$. This is a sequence of linear transformations that represents the transfer of applied fields into measured voltages. Note that matrix multiplication is not in general commutative, $XY \neq YX$, and the order of the sequence is therefore important.

The rotation from field to sensor axes can be decomposed into a rotation from field axes to mirror axes R_{BM} followed by a rotation from mirror axes to sensor axes R_{MV}, $R_{BV} = R_{MV} R_{BM}$. In terms of these rotations $D_V^{-1}(\vec{V} - \vec{V}_o) = E R_{MV}\, R_{BM}\, D_B^{-1} \vec{B}$ and $R_{BM}\, D_B^{-1} \vec{B} = R_{MV}\, E^{-1}\, D_V^{-1}(\vec{V} - \vec{V}_o)$, but $R_{BM}\, D_B^{-1} \vec{B} = \vec{B}_M$ is the magnetic field in components of the orthogonal mirror coordinate system. The calibration equation $\vec{B}_M = R_{MV}^{-1}\, E^{-1}\, D_V^{-1}(\vec{V} - \vec{V}_o)$ is then what allows the in-flight determination of orthogonal field components from telemetered sensor output voltages and the quantity $R_{MV}^{-1}\, E^{-1}\, D_V^{-1} = (D_V\, E\, R_{MV})^{-1}$ must be experimentally determined.

Discussion - The matrix S is in effect a measured parameter whose nine elements may be determined as described later. Assuming that the distortion matrices D_B and D_V have been independently determined, then $ER_{BV} = D_V^{-1}\, S\, D_B = T$ expresses the unknown scale factor matrix and sensor orientation in terms of known quantities. Because rotation matrices are orthonormal operators, their determinant is equal to one and the sum of the squares of the elements of each row or column is also one. Since E is a diagonal matrix of λ_i's, it just multiplies the i-th row of R_{BV} by its i-th diagonal element λ_i.

IDENTIFICATION OF CONTRIBUTIONS TO RESPONSE MATRIX (Continued)

The sum of the squares of the i-th row of the matrix T is therefore λ_i^2, the i-th scale factor, and dividing each row of T by its corresponding λ_i leaves just R_{BV}.

This procedure obtains E and R_{BV} under the stated assumptions. The rotation matrix R_{MV} must also be determined for the calibration equation. If R_{BM} can be independently measured, then $R_{MV} = R_{BM}^{-1} R_{BV} = R_{BM}^{T} R_{BV}$ where T denotes transpose and the equation is a result of the orthonormal properties of rotation matrices. Thus the scale factors and orientation of the sensor are determined as desired when S, D_B, D_V and R_{BM} are determined. We next consider the determination of the response matrix S.

TABLE 6-2. SUMMARY OF CONTRIBUTIONS TO RESPONSE MATRIX

Instrument Response Equation

$$(\vec{V} - \vec{V}_o) = S\,\vec{B}$$

$\vec{V}$ is the measured 3 component output voltage

$\vec{V}_o$ is the voltage offset vector

$\vec{B}$ is the 3 component applied field vector

S is a 3 x 3 instrument response matrix

Contributions to Response Matrix S

Matrix Operator	Source
E	different scale factor λ_i for each axis
D_B	$\vec{B}$ axes not orthogonal
D_V	$\vec{V}$ axes not orthogonal
R_{MV}	sensor axes rotated with respect to mirror axes
R_{BM}	field axes rotated with respect to mirror axes

Result:

$$S = D_V E\, R_{BV}\, D_B^{-1} = D_V E\, R_{MV}\, R_{BM}\, D_B^{-1}$$

Calibration Equation:

$$\vec{B}_M = (D_V E\, R_{MV})^{-1} (\vec{V} - \vec{V}_o) = G\,(\vec{V} - \vec{V}_o)$$

where $\vec{B}_M$ is magnetic field expressed in orthogonal mirror coordinates and

$$G = (R_{BM}\, D_B^{-1})\, S^{-1}$$

Scale Factor Determination

$$E R_{BV} = D_V^{-1}\, S D_B = T = [t_{ij}]$$

$$\lambda_i^2 = \sum_i t_{ij}^2$$

DETERMINATION OF THE RESPONSE MATRIX

The response matrix S and its variation with field amplitude can be determined as a least squares error estimate from a large number of sensor voltage and magnetic field measurements over the $\pm 6.4 \times 10^4$ γ range. The precision of the estimate improves with an increasing number of measurements.

The precision with which the response matrix S can be determined is a limiting factor in the precision of the scale factors and orientations derived from it. A statistical approach is most likely to yield the best estimate of the true value as well as allowing an estimate of the precision of the determination from the computed rms deviations. The inverse of the response matrix, S^{-1}, is also needed in the calibration equation referred to earlier. Since inversion of matrices whose elements are measured quantities is subject to potentially large errors, obtaining the inverse directly from the statistical analysis is a better procedure.

We now consider a linear least squares error fit of the measured data to the instrument response equation. The following assumes that all sensor output voltages have been corrected by subtraction of the previously determined offset voltages. This is not strictly necessary since they could be determined as part of the fitting procedure if enough measurements are made, but the independent measurement is likely to be more precise and the discussion is simplified under the assumption that the corrections have been made.

Measurement Vectors - For each sensor axis k = 1, 2, 3 the output V_k can be measured and expressed in terms of the three applied field components as indicated opposite. The unknown S_k are the elements of the k-th row of the response matrix S which is to be determined. If three such measurements are made for each sensor axis with different applied fields, a system of three equations in three unknowns results for each axis. In vector form this can be represented by $\vec{V}_k = B\vec{S}_k$ k = 1, 2, 3. The elements of the measurement vectors $\vec{V}_k$ and the rows of the 3 x 3 matrix B now refer to the three different measurements. Assuming the matrix B is non-singular, the exact solution is $\vec{S}_k = B^{-1}\vec{V}_k$ where $\vec{S}_k$ is the k-th row vector of the matrix S which is then determined. If a fourth measurement is made for each axis, its equation will be inconsistent with the other three due to errors in all four measurements. In general, for n measurements (n > 3) at fields over the full $\pm 6.4 \times 10^4$ γ range, each will have some error

and therefore deviate slightly from the best estimate. This can be represented in vector form as $B\vec{S}_k - \vec{V}_k = \vec{\Delta}_k$ for each axis where the measurement vectors $\vec{V}_k$ and the deviation vectors $\vec{\Delta}_k$ have n components and B is a 3 x n matrix.

Least Squares Error - The best estimate of error is the computed deviation. We wish to find that estimate $\vec{S}_k$ of the true value that minimizes the sum of the squares of the deviations. In matrix form, we minimize

$$\left(\vec{\Delta}_k^T \vec{\Delta}_k\right) = \vec{S}_k^T B^T B \vec{S}_k - \vec{S}_k^T B^T \vec{V}_k - \vec{V}_k B \vec{S}_k + \vec{V}_k^T \vec{V}_k$$

where T denotes transpose and the minimization is with respect to $\vec{S}_k$. That is we set the partial derivative to zero:

$$\frac{d}{d\vec{S}_k}\left(\vec{\Delta}_k^T \vec{\Delta}_k\right) = 0 = 2 B^T B \vec{S}_k - 2 B^T \vec{V}_k$$

This equation has a unique solution if $B^T B$ is non-singular

$$\vec{S}_k = (B^T B)^{-1} B^T \vec{V}_k$$

which is the desired least squares estimate for the k-th axis and the best estimate for the response matrix S has therefore been found in terms of the measured fields and voltages.

Inverse Estimate - The same data used to generate the response matrix S can also be used to generate its inverse $Q = S^{-1}$. This inverse is needed to define the calibration equation $\vec{B}_M = (R_{BM} D_B^{-1}) S^{-1} (\vec{V} - \vec{V}_o)$, previously derived, that allows the in flight determination of orthogonal field components from sensor output voltages. Re-expressing the instrument response equation as $\vec{B} = S^{-1} \vec{V} = Q\vec{V}$, we see that the data from the n measurements made can be rearranged in the following way: for each applied field axis k = 1, 2, 3 the k-th field component can be expressed in terms of the three measured voltage components as indicated below. The unknown Q_k are the elements of the k-th row of the inverse response matrix Q. For n measurements we have n such equations which in vector form are $\vec{B}_k = V \vec{Q}_k$ where $\vec{B}_k$, $\vec{Q}_k$ are n component vectors and V is a 3 x n matrix.

This form is identical to that used in the determination of S, and by direct analogy the least squares error solution for Q is determined by $\vec{Q}_k = (V^T V)^{-1} V^T \vec{B}_k$.

Statistical Weighting - The results above assume uniform statistical weights; that is, each measurement is given equal emphasis on the assumption that each of them is of equal importance and has equal probability of error.

DETERMINATION OF THE RESPONSE MATRIX (Continued)

This may not be the case; for example, perhaps during flight one axis of the magnetometer is more likely to be measuring low fields most of the time. Given such a situation, low field calibration data for that axis should be emphasized. This can be accomplished by minimizing the weighted least squares error ($\vec{\Delta}^T W\vec{\Delta}$) with appropriately chosen weights W. In this case the least squares error solution for S becomes $\vec{S} = (B^T WB)^{-1} (B^T W) \vec{V}$.

Estimate of Precision - The best estimate of the precision of the determination of $\vec{S}_k$ is $\left[\left(\vec{\Delta}_k{}^T \vec{\Delta}_k\right)/(n - 3)\right]^{1/2}$, assuming gaussian statistics and n measurements. The rms deviation of the experimental data from the best estimate value (non-linearity) is $\left[\left(\vec{\Delta}_k{}^T \vec{\Delta}_k\right)/n\right]^{1/2}$. These same formulas apply to the determination of the inverse with the appropriate change of variables.

The least squares error estimates of S and S^{-1} can thus be obtained as described above, complete with estimates of the variation of these quantities over the applied field range. From them the scale factors and orientation of sensor axes as well as the calibration equation can be derived as described, provided the associated axis distortions and rotations are known. We next consider the determination of these parameters.

TABLE 6-3. SUMMARY OF EQUATIONS

$$\vec{V} = S\vec{B}$$

for each sensor axis k and the i-th measurement:

$$V_{ik} = B_{i1} S_{k1} + B_{i2} S_{k2} + B_{i3} S_{k3} \quad i = 1, \ldots, n$$

$$\vec{V}_k = B\vec{S}_k$$

where $\vec{S}_k$ is the k-th row of response matrix S due to measurement error:

$$B\vec{S}_k - \vec{V}_k = \vec{\Delta}_k$$

minimize square error:

$$\left(\vec{\Delta}_k^T \vec{\Delta}_k\right) = \vec{S}_k^T B^T B \vec{S}_k - \vec{S}_k^T B^T \vec{V}_k - \vec{V}_k^T B\vec{S}_k + \vec{V}_k^T \vec{V}_k$$

solution is:

$$\vec{S}_k = (B^T B)^{-1} B^T \vec{V}_k$$

and

$$S = \begin{bmatrix} \vec{S}_1 \\ \vec{S}_2 \\ \vec{S}_3 \end{bmatrix}$$

for inverse $Q = S^{-1}$; $\vec{B} = Q\vec{V}$ for each field axis k and the i-th measurement:

$$B_{ik} = V_{i1} Q_{k1} + V_{i2} Q_{k2} + V_{i3} Q_{k3} \quad i = 1, \ldots, n$$

$$\vec{B}_k = \vec{V}Q_k$$

by analogy solution is:

$$\vec{Q}_k = (V^T V)^{-1} V^T \vec{B}_k$$

HOW ALIGNMENT IS DETERMINED

Alignment stability can be determined from a matrix equation relating changes in sensor axis orientation to the response matrix S and an optically measured rotation matrix. An unanalyzed technique for determining absolute alignment makes use of a precision gimbal to also relate the desired parameters to the response matrix S.

The instrument response matrix previously dissected into components and measured as described relates the output of the sensor axes to the magnetic test field axes. To obtain the sensor alignment and its stability over temperature and shock, the reference to test field axes must be removed since only parameters internal to the sensor assembly are of interest. For both absolute and stability measurements this will require an optical system to measure changes in orientation of the sensor assembly with a precision of better than 1 arc-second.

Rewriting the expression for the response matrix as

$$S = E\left(T_{MV}\, R_{BM}\, D_B^{-1}\right) = E\left(T_{MV}\, T_{BM}\right)$$

where $T_{MV} = D_V R_{MV}$ and $T_{BM} = R_{BM}\, D_B^{-1}$, then T_{MV} is a matrix of the direction cosines relating sensor axes to mirror axes. The change in this matrix ΔT_{MV} is what we wish to determine for stability, and its value describes the absolute alignment of the sensor axes. We next consider the properties of infinitesimal matrices that will allow determination of ΔT_{MV} without reference to an absolute external coordinate system.

Infinitesimal Matrix Properties - An infinitesimal matrix is one whose second order differences from the identity matrix I can be neglected. Infinitesimal distortion and rotation matrices commute, $XY \approx YX \approx (X + Y - I)$. If the initial alignment of the sensor assembly is kept within 0.1 degree, then the off diagonal elements of D_V, D_B, R_{BV} are less than 2.2×10^{-3} and they can be considered infinitesimals.

The equation for S may then be rewritten

$$S \approx E\left(T_{MV} + R_{BM} + D_B^{-1} - 2I\right)$$

where $T_{MV} = D_V\, R_{MV}$.

Alignment Stability - Changes in the alignment due to heat or shock change both $T_{MV} = D_V + R_{MV} - I = D_V\, R_{MV}$ and R_{BM}. The change in T_{MV}, ΔT_{MV}, which consists of the change in direction cosines of the sensor axes relative to the mirror axes, must be determined. Writing the difference equation

$$\Delta S = S' - S = E(\Delta T_{MV} + \Delta R_{BM} - 2I),$$

we see that if S and S' are measured, only ΔR_{BM} is needed to obtain the desired result. Since ΔR_{BM} is just the change in orientation of the mirrors mounted on the sensor assembly, this can easily be determined by two theodolites monitoring their orientation along two orthogonal lines of sight. This measurement thus does not require any absolute reference since only changes are needed.

Absolute Alignment - The specification for the absolute orientation of at least two of the sensor axes requires a well defined external mechanical

reference. Since the measured response matrix S determines the orientation of sensor axes relative to the field axes, knowledge of the orientation of either axis relative to the external reference will determine the other. If the same optical system that monitors the sensor mirrors also either defines or can relate the mirror axes to the mechanical reference, the absolute sensor orientation with respect to the mirrors will have been determined. In matrix terms, expressing $R_{BM}D_B^{-1}$ as T_{BM}, then $T_{BM} = T_{XM}\,T_{BX}$ where X refers to the external reference system and the T's are matrices of direction cosines. Expressing S as

$$S = E\,(T_{MV}T_{BM}),$$

then

$$T_{MV} = E^{-1}S\,T_{BM}^{-1} = E^{-1}\,S(T_{XM}\,T_{BX})^{-1}$$

and the absolute alignment is determined when T_{XM} and T_{BX} are determined.

One possibility for a suitable reference system X is that defined by the rotational axes of a precision 2-axis gimbal. Appropriately mounted mirrors will allow theodolites to obtain the transform matrix T_{XM}, and T_{BX} may be obtained as follows: Referring to the figure below, rotating one sensor axis around $\vec{\omega}$ by a precisely known angle c will determine the direction cosine of the applied Field $\vec{B}$ with respect to $\vec{\omega}$ with the formula given. Another rotation around an orthogonal axis will then define another direction cosine and so on. In this way the direction cosines of each of the test field axes can be determined and T_{BX} is defined.

The details of this procedure have not been worked out and the precision that can be expected for T_{MV} has not been determined. Nevertheless, the procedure may be adequate if a sufficiently precise 2- or 3-axis non-magnetic gimbal mount can be obtained.

TABLE 6-4. SUMMARY OF EQUATIONS

$$S = E(D_V R_{BV} D_B^{-1}) = E(D_V R_{MV} R_{BM} D_B^{-1})\;E(T_{MV} R_{BM} D_B^{-1}) = E(T_{MV}T_{BM})$$

Stability Equation: $\Delta T_{MV} \approx (E^{-1}\Delta S - \Delta R_{BM} + 2I)$

Alignment Equation: $T_{MV} = E^{-1}S(T_{XM}T_{BX})^{-1}$

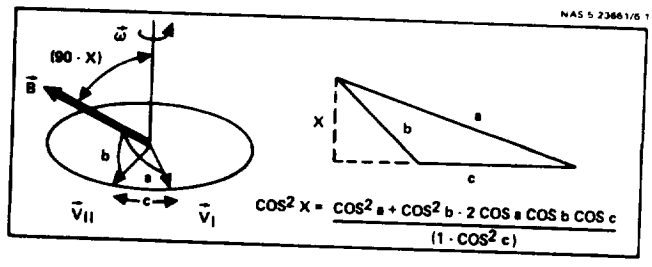

Figure 6-1. Absolute Orientation. The direction cosine of an applied field B, cos x, can be determined relative to a rotation axis $\vec{\omega}$ by two sensor output measurements: $\vec{V}_I \cdot \vec{B} = \lambda B \cos a$ and $\vec{V}_{II} \cdot \vec{B} = \lambda B \cos b$ separated by a precisely known sensor rotation c.

SUMMARY OF ACCURACY AND EQUIPMENT REQUIREMENTS

To obtain the required accuracy of measurement the GSFC magnetic test facility must be upgraded to 0.1γ field accuracy and the orientation of its magnetic axes must be specified to 0.4 arc-seconds.

The accuracy desired in the determination of this magnetometer's scale factors and alignment exceeds that of currently available instrumentation. Almost every parameter must be measured to within a few parts per million (ppm). Using the best available equipment and careful statistical handling of the data obtained from it should allow the requirements to be met. It may be necessary, however, to relax the requirement for the absolute alignment of sensor axes to within 1 arc-second if the orientation of the test facility field axes relative to some optical axes cannot be determined with better accuracy. The requirements due to each of the sensor parameters are enumerated in the table opposite and discussed below, assuming sensor scale factors on the order of 150 $\mu V/\gamma$.

Offset - Since the magnetic field in the GSFC test volume can be set to zero only within 0.2γ, measurement of the offset to higher precision must be accomplished by reversing the magnetometer axes. For a uniform field where slight translational differences between "up" and "down" measurements are negligible, the accuracy of reversal need not be great — 10 degrees error in angle only produces a 1% change in the measured offset for 0.2γ residual field. The factor limiting the precision of the offset determination is therefore likely to be the voltmeter used, which must measure ~60 μV.

Noise - To measure sensor noise of 0.3γ over the dc to 25-Hz bandwidth in a 10-second period will require a strip chart recorder and voltmeter capable of measuring 45 μV at up to 25 Hz. Also required is a mu-metal flux tank to reduce ambient field variations by a factor of 300 or better. A superconducting shield would be even better and could also be used to determine offset, but the large sensor diameter (6 inches) may make this impractical. In any case, a flux tank is adequate.

Scale Factor and Linearity - The scale factor must be determined to 20 ppm, which allows 10 ppm uncertainty in each of the magnetic field and voltage measurements. Available voltmeters have accuracies of ~20 ppm and current GSFC field accuracies are also ~20 ppm. Neglecting the effects of drifts during multiple measurements, the improvement in precision from n measurements varies as $(n - m)^{-1/2}$ where m equals the number of parameters to be determined. Since the response matrix has nine elements, a factor of two improvement requires a minimum of 13 separate measurements at each field value.

Alignment - The alignment stability of 5 arc-seconds and absolute alignment of 1 arc-second is the hardest specification to meet. With high quality theodolites and mirrors, the changes in orientation of the sensor assembly with respect to the optical axes can be monitored to 0.1 arc-seconds, which is adequate. The orientation of the magnetic axes involves knowledge of both the magnetic field and the sensor output voltage. Since 1 arc-second is 5 ppm, both quantities must be determined to better than 5 ppm.

A field of 50,000γ must therefore be accurate to better than $\pm 0.25\gamma$, and corresponding voltages of 7.5 V must be measured to better than ± 38 μV absolute. The required field accuracy may be obtainable by taking 100 measurements with the proton reference magnetometer at GSFC. For

a field accuracy of ±0.1γ and voltmeter accuracy of ±10 μV, the remaining error budget of ±0.4 arc-second from an RSS total of 1.0 arc-second represents the total allowable error in determining the optical orientation of the magnetometer mirrors relative to the GSFC field axes.

Accuracies on the order of a few arc-seconds in the determination of the field axis orientation with respect to an optical reference may be attainable by the previously suggested gimbal mount technique. This is not within the allowable 0.4 arc-second budget, however. Further analysis is required to determine the accuracies attainable by this or any other suggested procedure for the absolute alignment.

TABLE 6-5. REQUIREMENTS

- Offset
  - 0.2γ null field
  - 60 μV voltmeter
  - 180^{o} ±10^{o} gimbal mount
- Noise
  - Strip chart recorder
  - 45 μV voltmeter
  - Mu-metal fluxtank
- Scale Factor
  - 64,000 ±0.5γ magnetic field
  - 7.5 V ±100 μV voltmeter
- Alignment
  - 6.4×10^{-4} ±0.1γ magnetic field
  - 7.5 V ±10 μV voltmeter
  - 0.1 arc-second theodolites
  - 1 arc-second 2-axis gimbal mount
  - 0.4 arc-second GSFC field axis orientation

Note - The analyses of this section have assumed a single range analog electronics system and an error budget appropriate to that approach. For a multiple range OFG system the budgeted errors can be larger since part of the ADC function is included in the sensor electronics. The calibration voltmeter requirements are less stringent, but each sensor range must be separately calibrated.

APPENDIX A
NOISE PERFORMANCE OF FLUXGATE SENSORS

SIGNAL-TO-NOISE RELATIONSHIPS FOR RING-CORE SENSORS

Despite contrary suggestions in the fluxgate literature, it is possible to make quantitative estimates of the signal-to-noise ratio for ring core sensors. The noise equivalent field strength varies inversely as the square root of the product of frequency and core volume.

The fluxgate literature contains no clear-cut analysis of the signal-to-noise performance for fluxgate sensors. This lack is apparently caused by the fact that it is customary to cite an early work by William and Noble (1) on Barkhausen noise which does not predict effects of the observed magnitude. In fact, recent explanations of Barkhausen noise do appear to predict the observed fluxgate signal-to-noise ratio, especially when values of the demagnetizing factor appropriate to the cylindrical geometry are used.

The most authoritative review of Barkhausen noise appears to be that of H. Bittel, who reviews earlier work on the effect. The principal reason why the effect appears to be larger than at first thought is that the elementary magnetic dipoles in the material are not reversed one by one but rather in clustered groups containing up to 10^{+17} elementary dipoles. The effect of this clustering is to produce fewer but much larger noise pulses, which causes a much higher noise signal than that calculated by G. W. McFarlane and reported by Williams and Noble. As a simple approximation to a very complex phenomenon, Bittel calculates that the Barkhausen noise energy is enhanced over the white noise expected from the flipping of single dipoles by a factor porportional to $n_c v_d I_s$, where n_c is the number of domains interacting in a cluster, v_d is the domain volume, and I_s is the saturation magnetization (expressed in the same units as B, so that $I_s \approx B_s$).

The work on which Bittel based his review was performed on grain-oriented 3% Si-Fe, a very noisy material unsuitable for fluxgates (but ideal for the study of Barkhausen noise). Fortunately, T. Higuchi (6) has performed measurements on a number of core materials used in magnetic amplifiers and modulators, including Supermalloy and Mo-Permalloy as well as grain-oriented 3% Si-Fe. The noise for Mo-Permalloy is about 500 times less than it is for the 3% Si-Fe, which, comparing with Bittel's paper, leads to a value of $n_c v_d$ for Mo-Permalloy of 4×10^{-12}, less by a factor of 25×10^4 than for the 3% Si-Fe materials.

One may now calculate the signal-to-noise ratio expected in a fluxgate sensor. To keep things simple, we have assumed that the sensor preamplifier is untuned so that all even harmonics are kept; in practice, this procedure would probably give rise to high order harmonic sensitivity and phase instability, but the signal-to-noise ratio should not be greatly different from that of a practical system.

The result, derived in detail in the subsequent pages, is shown opposite. The noise-equivalent magnetic field varies directly with the saturation field of the core and inversely with the demagnetizing factor and the square root of the core volume, drive frequency, and integration time. This result checks quantitatively as well, predicting noise levels of ~0.04Y rms with typical core geometries. (A slight over estimate due to various simplifications.)

THE NOISE EQUIVALENT FIELD FOR A FLUXGATE MAGNETOMETER

The noise-equivalent magnetic field for a ring-core fluxgate is approximated by the following formula. The value of $n_c v_d$ is about 4×10^{-12} cm^{-3} for the Permalloy used by Higuchi.

$$\Delta B_n = \frac{K}{2}\sqrt{\frac{n_c v_d}{VfT}}\, B_s$$

n_c = cluster number

v_d = domain volume

V = core volume

f = drive frequency

T = integration time (1/(2x noise bandwidth)

B_s = saturation field of core

K = demagnetizing factor

References

1. F.C. Williams and S.W. Noble, Proc. IEE (London) 97, 455 (1950)
2. D.I. Gordon, R.H. Lundsten, R.A. Chiarodo, IEEE Trans. on Magnetics, Vol MAG-1, 330 (1965)

   D.I. Gordon, R.E. Brown, IEEE Trans. on Magnetics, Vol MAG-8, 76 (1972)
3. M.H. Acuna and C.J. Pellerin, IEEE Trans. Geoscience Electronics, 253 (October 1969)
4. S.V. Marshall, IEEE Trans. on Magnetics, Vol MAG-3, 459 (1967)
5. H. Bittel, IEEE Trans. on Magnetics, Vol MAG-5, 359 (1969)
6. T. Higuchi, IEEE Trans. on Magnetics, Vol MAG-7, 317 (1971)
7. R.M. Bozorth and D.M. Chapin, J. Appl. Phys. 13, 320 (1942)
8. M.M. Weiner, IEEE Trans. on Magnetics, Vol MAG-5, 98 (1969)

EVALUATION OF THE DEMAGNETIZING FACTOR FOR RING-CORES

The demagnetizing factor for radially thin ring-core sensors can readily be calculated in cylindrical geometry from first principles. The correct result differs materially from the long cylindrical rod result often quoted in the literature.

The field inside the core is not as high as it would be in an infinite parallel-plane geometry because of the influence of end effects. For long rods, the demagnetizing factor is given by Bozorth and Chapin (7). While their formula is usually used in the literature to apply to ring cores, it is better to use the correct geometry if one wants correct results.

The ring core behaves as a magnetic shield, blocking the field from its interior by guiding it inside the core material (see sketch). Thus, it has what amounts to a capture cross section for the incident flux lines. For high enough permeability, all of the field is contained in the metal and further increases in permeability do not increase the captured flux. Since the width of the core tape is large compared to thickness, an infinite-cylinder calculation should provide a good estimate of the captured flux.

Consider an infinite cylindrical magnetic shell with isotropic, homogeneous relative permeability $K_m = \mu/\mu_o$, placed in a magnetic field ΔB, normal to the axis of the cylinder. Let the inner and outer radius of the shell be a and b respectively. Then, the magnetic scalar potential outside the cylinder, inside the iron, and inside the cylinder must satisfy the following equations.

Outside: $$\Omega_m = -(\Delta B r + Ab^2/r^2)\cos\theta \qquad (1A)$$

In the iron: $$\Omega_m = -(Br + Cb^2/r^2)\cos\theta \qquad (1B)$$

Inside: $$\Omega_m = -Dr\cos\theta \qquad (1C)$$

The constants A, B, C and D are as yet unknown. This form follows because, at infinity, the field must be all in the x direction, so that the scalar potential must have the form

$$\Omega_m = -\Delta B\, x = -\Delta B\, r\cos\theta \qquad (2)$$

The terms in $\cos\theta/r^2$ are the only other solutions of Laplace's equation allowed which have the same angular dependence.

The four constants A, B, C, and D can be found by matching the magnetics boundary conditions at r = a and r = b: namely, that the normal component of $B = -\Delta\Omega_m$ as well as the tangential component of $H = B/\mu$ must both be continuous. The exact result for the field inside the iron at right angles to the outside field is

$$\Delta B' = 2K_m B_o[(K_m+1)b^2/a^2 + (K_m-1)b^2/r^2]/[(K_m+1)^2b^2/a^2 - (K_m-1)^2] \qquad (3)$$

If we write this in terms of the diameter for a radially thin core of high permeability by putting

$a = b = d/2$, $(b - a) = t$, and $K_m \gg 1$, the result for the average field reduces to

$$\Delta B' \approx K_m \Delta B/(1 + K_m t/d) \approx \Delta B(d/t),\ K_m \gg 1 \qquad (4)$$

This result, while still approximate, is more nearly correct than the usual long rod approximation in which $\Delta B'$ varies nearly as d^2/wt, where w is the core width. The "demagnetizing factor" is thus $K = t/d$. The capture cross section is simply the geometric cross section wd.

We shall now apply this result to calculate the sensitivity of a ring-core fluxgate.

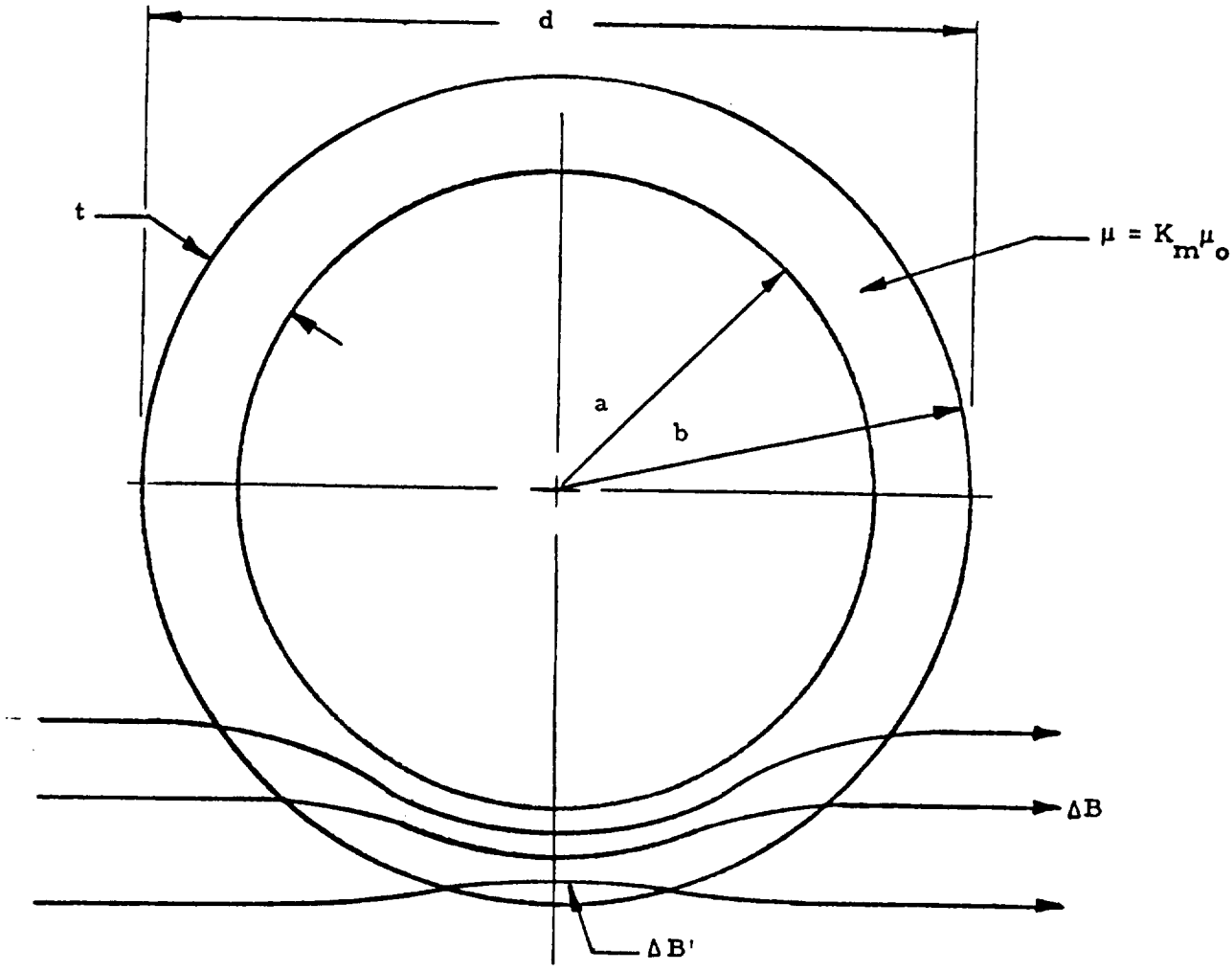

Cylindrical Geometry used in Calculation. The ring core is approximated by a thin-walled cylindrical shell.

MINIMUM SENSITIVITY OF THE RING CORE SENSOR

Simple formulas for the minimum sensitivity can now be derived by taking advantage of the square-loop approximation and the knowledge of the demagnetizing factor.

To calculate the signal-to-noise ratio, we will need to know the sensitivity of the fluxgate sensor.

Estimation of Sensitivity - The sensitivity to ambient field variation has been calculated by a number of authors, not always with consistent results (1, 2, 3, 4). We prefer a simplified viewpoint. Instead of calculating the second harmonic output, we will calculate the output of the even-harmonic synchronous demodulator assuming use of a broadband amplifier so that all even harmonics are used. This calculation is easily performed in the time domain without the need for Fourier representation (which complicates the noise analysis). To simplify matters, we assume use of a square-loop core, and a triangular current drive waveform which results in a rate of change of flux and concomitant induced voltage along the vertical sides of the loop, and zero induced voltage elsewhere. The derivation is as follows (see the accompanying figure).

First consider the output of a single half of the core with no field outside. As the field increases along the vertical side of the square loop from $-B_S$ to B_S, the pickup coil produces a voltage output pulse of amplitude $E = NA\dot{B}$ and width $2B_S/\dot{B}$, where N is the number of turns on the pickup coil, A is core area, and $\dot{B}$ is the rate of change of magnetic field. A corresponding negative pulse is produced as the field sweeps through the opposite side of the loop. This zero-field output signal contains only odd harmonics of the drive field.

When the core is biased by an external field, ΔB so that the internal field is biased by $\Delta B'$, the pulses tend to separate in one half of the core and come together in the other half, as shown. The pulses move by a time interval $\Delta t = \Delta B'/\dot{B}$. When the pulses from the two half cores are differenced by appropriate connection of the pickup coil (simply by winding it around the core), the difference signal becomes a doubled-frequency signal, as shown, with no odd harmonics of the drive frequency remaining. When demodulated by an appropriately phased synchronous demodulator, and averaged for a time T, the contribution to the average for each cycle is $8E\Delta t/T$. For a total of fT cycles, we obtain the output voltage

$$e_s = 8fNA\ \Delta B' = 8fNAd\ \Delta B/t = 8fNdw\ \Delta B \qquad (5)$$

where we have used the demagnetizing factor derived in the last section to express $\Delta B'$ in terms of the external ambient field ΔB. The symbols d, w, and t represent core diameter, height, and radial thickness respectively.

The derived sensitivity is a minimum because we have neglected the contribution of partially saturated regions which still have enough permeability to contribute signals but which do not contribute Barkhausen noise.

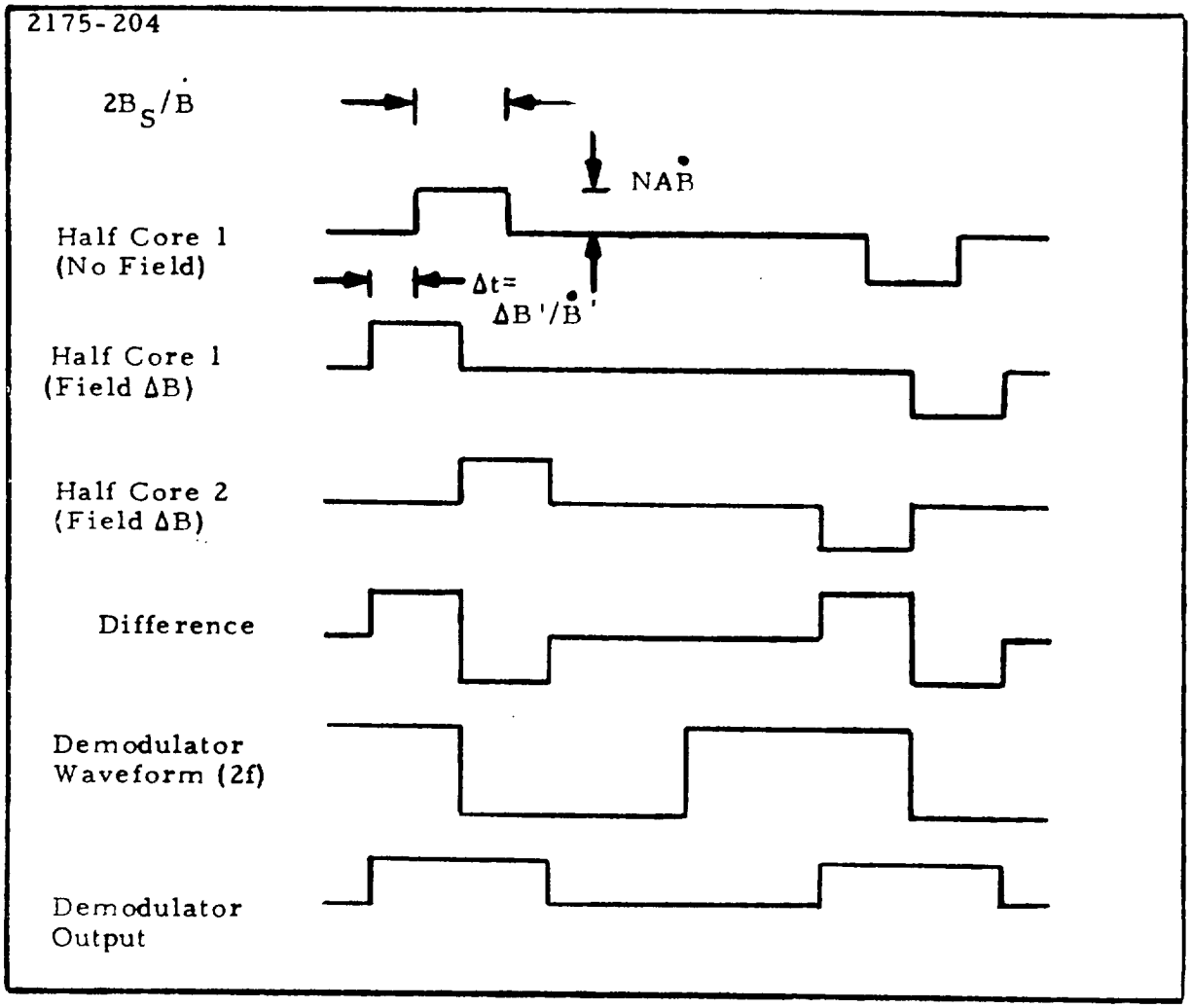

Analysis of Fluxgate Sensitivity. Fluxgate Waveforms are shown for an idealized square B-H loop and untuned amplifier.

BARKHAUSEN NOISE AND THE NOISE-EQUIVALENT FIELD FOR RING-CORE FLUXGATES

Using a simple model for Barkhausen noise, calibrated for typical fluxgate core materials by reference to published data, we can calculate the Barkhausen noise and noise equivalent field for the ring-core sensor.

We can now see how the details of the noise calculation are carried out.

Noise Calculation - Because the simplified model for Barkhausen noise is really only a shot noise model (with cannonballs for shot) we can use a time domain method of evaluation.

The effect of the demodulator on the noise is insignificant, since all it does is reverse the sign of pulses which are already bipolar. Thus, all we need do is calculate the effect of integrating the noise energy. Bittel (5) has already done this, in effect; his formula for the noise energy from the pickup coil, integrated along one side of the hysteresis loop, is

$$E_n = 8 n_c v_d N^2 (A/\ell) B_s^2 \qquad (V^2 - s^2) , \tag{6}$$

where n_c is the average number of domains per noise cluster, v_d is the average domain volume, N is the number of turns of the pickup coil, A and $\ell = \pi d$ are the coil cross-sectional area and length, and where we have replaced the saturation magnetization by the saturation field B_s, because the permeability is high.

The noise voltage per cycle generated at the output of an integrator can be calculated from Campbell's theorem:

$$e_n^2 = \int A^2 h^2(t) R dt \tag{7}$$

where R is the rate of arrival of events of mean-square amplitude A, and $h(t) = 1/T$ for $0 \geq t \geq T$ and is zero otherwise. Bittel's formula is already integrated, so that to apply it we need only to multiply equation (6) by (1) a factor fT to allow for the total number of noise bursts; (2) a factor 2 to allow for the differential pickup winding; and (3) $1/T^2$ to normalize $h^2(t)$. The end result for the noise at the output of the integrating filter is

$$e_n^2 = 16 \frac{f}{T} n_c v_d N^2 (A/\ell) B_s^2 \tag{8}$$

Noise Equivalent Field Strength - By setting the signal-to-noise ratio equal to unity and solving for the ambient field strength, we can find the noise equivalent field strength. Formally,

$$\Delta B_n = e_n / (\sigma e_s / \sigma \Delta B) \tag{9}$$

The result of performing this operation using the sensitivity and demagnetization factor $K = t/d$ derived earlier, is

$$\Delta B_n = \frac{1}{2} \sqrt{\frac{n_c v_d}{fTv}} \; B_s \left(\frac{t}{d} \right) \tag{10}$$

Here, as before, v is core volume; the factor t/d which represents the demagnetizing effect is kept separate to show the fundamental dependencies on core volume and demagnetization separately. However, the volume v for a ring-core is πdtw; when this relation is plugged in, the result is

$$\Delta B_n = \frac{1}{2}\sqrt{\frac{n_c v_d}{\pi f T}\,\frac{t}{d^3 w}}\;B_s \qquad (11)$$

It is good to make the core big, thin, and wide. This is a new result, since the thin-rod analysis presented in the literature leads to the conclusion that the core width w should be small.

In the table below we present the calculation of the actual noise-equivalent magnetic field strength for a 1971 Time-Zero sensor which exhibited a noise for a 1 Hz single pole bandwidth of 0.14γ peak to peak. The calculated rms noise equivalent ΔB (NE ΔB) seems only a factor of two high; in view of neglected signal contributions and metallurgical differences between Time-Zero in California, Bittel in Germany and Higuchi in Japan, the agreement seems rather good. None of this rationale has been published but it will be.

Conclusion - Fluxgate noise levels are consistent with observed values for Barkhausen noise. The noise varies as $(t/d^3w)^{1/2}$.

Calculation of NE ΔB for TZ Sensor

$$n_c v_d = 4 \times 10^{-12}\ \text{cm}^{-3}$$

$$d = 1.5 \text{ inches} = 3.8 \text{ cm}$$

$$t = 0.001 \text{ inches} = 0.0025 \text{ cm}$$

$$w = 0.28 \text{ inches} = 0.71 \text{ cm}$$

$$f = 15 \text{ kHz}$$

$$T = 0.5 \text{ (1 Hz noise BW)}$$

$$B_s = 0.8 \text{ Tesla}$$

$$\Delta B_n = \frac{1}{2}\sqrt{\frac{n_c v_d}{\pi f T}\,\frac{t}{d^3 w}}\;B_s = 0.04\gamma \text{ rms}^*$$

*This value is for ordinary 4-79 Permalloy, used by Higuchi and in the TZ sensor. The value of $n_c v_d$ is about two orders of magnitude lower for well-annealed 6-81.3 Permalloy.

ESTIMATE OF MAGNETOSTRICTIVE OFFSET

A simplified estimate of the magnetostrictive offset shows that the offset, like the noise, is reduced by use of thin tape and a large diameter bobbin.

It is generally agreed that the principal source of residual offset in a properly constructed fluxgate sensor is magnetostrictive. The research conducted at the Naval Ordnance Laboratory in developing the lunar surface magnetometer for Apollo showed that the best offset performance was attained by using as a core material a permalloy containing 6 percent molybdenum and 81.3 percent nickel. For this nickel concentration, the longitudinal magnetostriction is zero[2]. Even when such material is used, some residual effect may be present, so it is important to understand how the offset is generated. Weiner[8] has presented a theory of the effect, assuming sinusoidal waveforms and a particular shape for the magnetostriction curve. Weiner also presents data showing that the effect varies with drive level, peaking if the core is driven just to saturation, and becoming much smaller if the core is overdriven.

For permalloys whose nickel content is near 80%, the magnetostrictive elongation is small until the material saturates, when the elongation increases to the (small) saturation value λ_s. It seems reasonable to treat the magnetostrictive curve as a step onset at saturation (Figure A). Then, the flux and magnetostriction during the cycle will vary somewhat as shown in Figure B.

The voltage induced in the second-harmonic pickup coil is given by:

$$e = NA\frac{dB}{dt} + NB\frac{dA}{dt} \quad , \tag{1}$$

where N is the number of turns on the pickup coil, A is the core cross-sectional area, and B is the field intensity. The second term is the derivative of the magnetostrictive flux change term in Figure B. The magnetostrictive part of the voltage waveform (Figure C) consists of a series of spikes at the second harmonic of the drive frequency.

The area of each spike is roughly given by

$$\int e\,dt = NB\,\Delta A = NB_s\lambda_s A \tag{2}$$

When divided by the sensitivity calculated earlier, the offset expressed in magnetic field units is

$$B_o = \frac{1}{4}\lambda_s B_s \frac{t}{d}$$

where d is the core diameter and t is the tape thickness. This formula predicts that the offset is independent of tape height, a rough result because it is based on the infinite-cylinder calculation of the demagnetizing factor. For d = 1 inch, t = 0.0005 inch, $\lambda_s = 5 \times 10^{-6}$ (79% NiFe) and $B_s = 0.8$T, the offset estimated from this formula is 0.5γ — not far from what is observed. The effect is temperature-dependent which presumably gives rise to the observed offset instability of a few tenths of a gamma.

When the longitudinal magnetostriction is reduced by use of the proper alloy, residual volume magnetostriction still exists. This effect is very small, about 1 part in 10^8 for the typical sensor drive conditions, and may be neglected.

Thus, to obtain a sensor with stable offset characteristics, it is advisable to use as a core material a Ni-Fe-Mo alloy with 81.3% nickel.

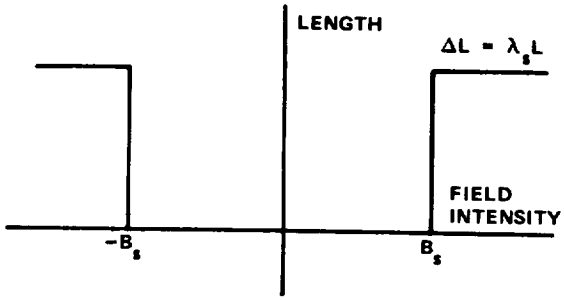

Figure A. Magnetostriction Model
The length change is assumed to occur suddenly at saturation. B_s is field intensity at the knee of the stiffness curve.

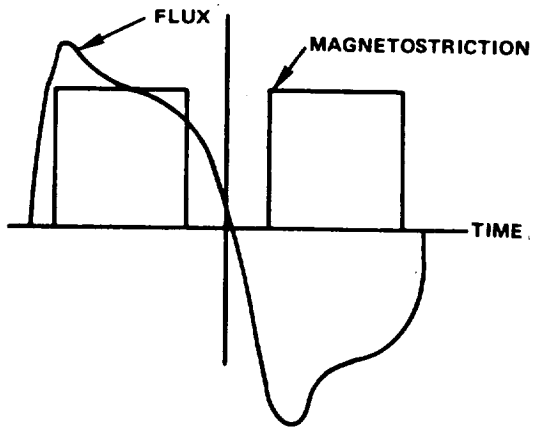

Figure B. Variation of Flux and Magnetostriction During the Sensor Drive Cycle
The flux variation curve assumes the use of a reactive pumping drive circuit.

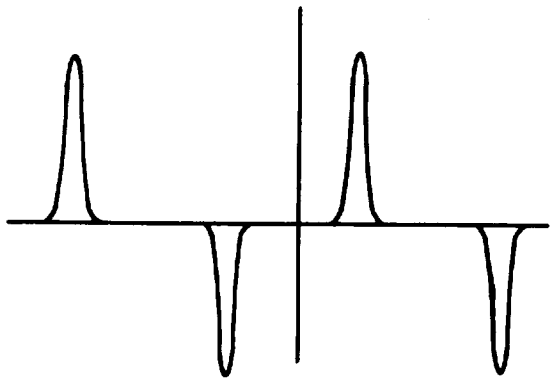

Figure C. Magnetostrictive Error Voltage
The voltage is proportional to the derivative of the magnetostrictive curve; the spikes occur at twice the drive frequency.

APPENDIX B

DETAILS OF STRUCTURAL ANALYSIS

APPENDIX C

ANALYSIS OF STRUCTURAL STABILITY

SUPPORTING STRESS AND VIBRATION ANALYSIS

Sensor Structural Stability

1. Deflection of spherical coil form

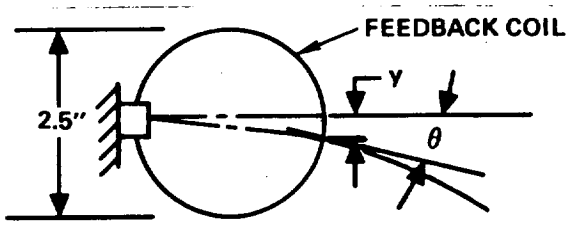

Note that we are concerned with y deflection, not Slope G

The sphere can be conservatively modeled as a hollow cylinder with 0.2-inch thick walls.

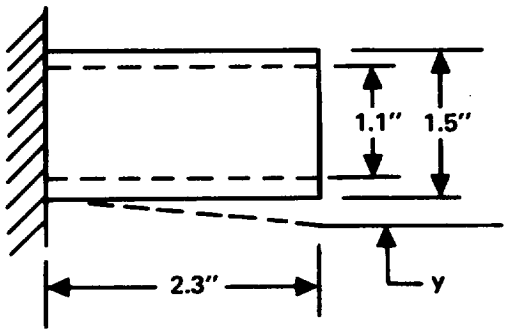

then max $y = \frac{W\ell^3}{3EI}$

where E = 12×10^6 psi for graphite-epoxy

$$I = \frac{\pi}{4}(R_2^4 - R_1^4)$$

$$= \frac{\pi}{4}\left[\left(\frac{1.5}{2}\right)^4 - \left(\frac{1.1}{2}\right)^4\right]$$

$$I = 0.17664$$

(273 turns No. 36 wire)

W = wt. of coils and coil form

$$= \left(\frac{\pi}{4}\right)(0.005)^2 (2.5\pi)\, 6 \times 273 \times 0.323 + \frac{4}{3}\pi(1.3^3 - 0.9^3)\, 0.058$$

= 0.46 less 0.03 for groove and hole

W = 0.43 lb.

$$y = \frac{(0.43)(2.3)^2}{3 \times 12 \times 10^6 \times 0.17664} = 0.83 \times 10^{-6} \text{ in.}$$

$$\frac{\Delta y}{y} = \frac{0.83 \times 10^{-6}}{2.3} = 0.36 \times 10^{-6} \sim 4 \times 10^{-7} \text{ in./in.}$$

$$\frac{3.6 \times 10^{-7}}{5 \times 10^{-5}} \approx 0.01 \text{ arc-second}$$

where

5×10^{-5} in./in. = 1 arc-second

2. Deflection of coil with respect to mirror mount.

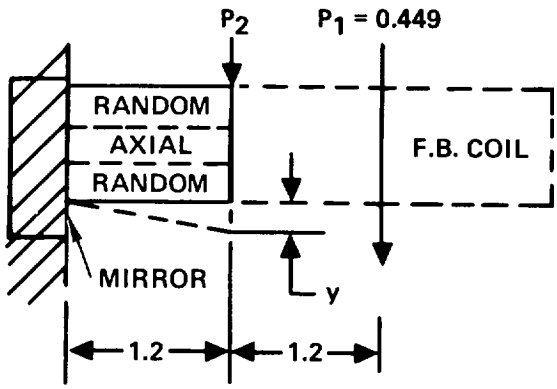

P_1 = Wt. of feedback coil + Wt. of tower stand

$= 0.43 + \frac{\pi}{4}(0.6)^2 \times 1 \times 0.058 = 0.449$ lb.

$P_2 = 2P_1 = 0.898$ lb.

$$y = \frac{Wl^3}{3EI}$$

where E = 20×10^6 graphite-epoxy with fibers oriented axially and random

$$I = \frac{\pi}{4}(0.7)^4 = 0.189$$

$$y = \frac{(0.898)(1.2)^3}{3\,(20 \times 10^6)(0.189)} = 1.4 \times 10^{-7} \text{ in.}$$

$$\frac{\Delta y}{y} = \frac{1.4 \times 10^{-7}}{1.2} = 1 \times 10^{-7} \text{ in./in.}$$

Dynamic

Random load factor g_f = 2.2 (12.9 rms gs) = 28

Sine g_f = 20 g max. at 36 - 150 Hz

Use 28 g

Find deflection of base

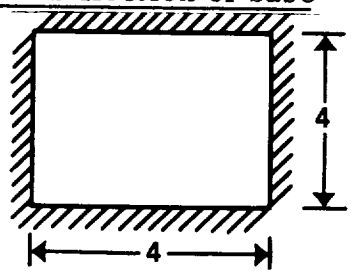

Flat plate clamped all edges dimensions 4 x 4 x 1/2-inch thick

From Roark and Young, 5th Edition, Table 26, Case 8a and 8b

8a uniform load over entire plate.

$$\text{max } y = \frac{\alpha q b^4}{Et^3} = \frac{(0.0138)(\frac{1.75}{16})(4)^4}{(20 \times 10^6)(0.5)^3}$$

max y = 0.15×10^{-6} in.

For sensor weight see below.

SUPPORTING STRESS AND VIBRATION ANALYSIS (Continued)

8b load concentrated over small area of radius R_o ~0.2"

$$\max y = \frac{\alpha W b^2}{Et^3} = \frac{(0.0611)(1.75)(4)^2}{20 \times 10^6 (0.5)^3} = 10.9 \times 10^{-6} \text{ in.}$$

Actual displacement can be approximated as 1×10^{-6} because it will be much closer to 8a.

Weight

Mirror	0.079 lb/in^3
Graphite-Epoxy	0.058 lb/in^3

Mirror

$$2 \times 2 \times 1/2 \times 0.079 = 0.158$$

Boom Cable

$$\frac{20}{22} \quad \frac{685}{454} = 1.37 + 0.10\,(1.37) = 1.51$$

Sensor

Windings - No. 36 wire 273 turns

Feedback Coils $6\left[\frac{\pi}{4}\ (0.005)^2 \times 2.5\pi \times 273 \times 0.323\right] = 0.104$

Cancellation Coils $6\left[\frac{\pi}{4}\ (0.005)^2\ 5\pi\ (64)(0.363)\right] = 0.038$

Total 0.142

Base

$$4 \times 4 \times 0.5 \times 0.058 = 0.464$$

Tower

$$\frac{\pi}{4}\,(0.6)^2\,(1)\,(0.058) = 0.016$$

Sensor Support

$$\frac{0.050}{0.063} \times \frac{9.4}{454} = 0.019$$

Cancellation Sphere - $\frac{0.058}{0.063} \times \frac{202}{454} = 0.410$

Feedback Sphere - $\frac{0.058}{0.063} \times \frac{176}{454} = 0.357$

Sensors = 0.015 Miscellaneous = 0.2

Total Sensor w/mirror 1.75 lb.

Resonant Frequency of Base

Using curves by Maarten Vet

$$\rho = \frac{1.75}{4 \times 4 \times 0.5} = 0.219$$

$$f_n = \alpha \left(\frac{h}{a^2}\right) \left(\frac{E}{\rho (1 - u^2)}\right)^{1/2} \qquad u \sim 0.13$$

$$= 35 \left(\frac{0.5}{4^2}\right) \left(\frac{20 \times 10^6}{(0.219)(0.99)}\right)^{1/2}$$

$$= 10,500 \text{ Hz}$$

Assuming cantilever spring and mass — very conservative

$$f_n = \frac{1}{2\pi} \left(\frac{g}{f}\right)^{1/2} = \frac{1}{2\pi} \left(\frac{386}{1 \times 10^{-6}}\right)^{1/2} = 3126 \text{ Hz}$$

Using Steinberg comparison method

$$f_n = f_1 \frac{0.0768h}{ab} \left(\frac{E}{\rho (1 - u^2)}\right)^{1/2}$$

$$= 451 \frac{(0.0768)(0.5)}{4 \times 4} \left(\frac{20 \times 10^6}{0.219\ (0.99)}\right)^{1/2}$$

$$= 10,400 \text{ Hz}$$

Safe to assume f_n >4000 Hz, which is twice highest input frequency.

Deflection and f_n of Sensor Support

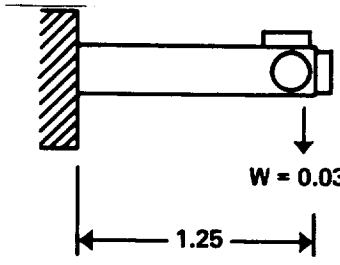

W = 0.019 + 0.015 = 0.034 lb.

See Roark and Young Table 3 Case 1a

E = 42×10^6 Fiber axially oriented graphite-epoxy

$$\max y = \frac{W\ell^3}{3EI} = \frac{(0.034)(1.25)^3}{3\ (42 \times 10^6)\ \frac{\pi}{4} \times (0.2)^4}$$

$$= 0.42 \times 10^{-6} \text{ in.}$$

$$\frac{\Delta y}{y} = \frac{0.42}{1.25} \times 10^{-6} = 0.34 \times 10^{-6}$$

$$f_n = \frac{1}{2\pi}\left(\frac{g}{f}\right)^{1/2} = \frac{1}{2\pi}\left(\frac{386}{0.42 \times 10^{-6}}\right)^{1/2}$$

$$f_n = 4800 \text{ Hz}$$

Maximum Dynamic Stress in Support

$$\sigma = \frac{28\,(0.034)(1.25)(0.2)}{\frac{\pi}{4}(0.2)^4} = 189 \text{ psi}$$

Well below allowable of 50,000 psi.

Dynamic deflection

$$\max y = 28\,(0.34 \times 10^{-6}) = 9.52 \times 10^{-6}$$

Maximum Sensor Stress

Occurs in baseplate

$$g_f = 28\,g$$

$$\sigma = \frac{B_2 W}{t^2} = \frac{(0.7542)\,(28 \times 1.75)}{(0.5)^2}$$

Load applied over small area of center of plate. Maximum stress occurs at center of edge of plate. See Roark and Young, Table 26, Case 8b

$$\sigma = 148 \text{ psi}$$

This is lower than stress in the sensor support. Maximum stress occurs in sensor support and is $\sigma = 189$ psi.

COIL WIRE STRESS

y_s = 10,000 psi copper coil wire

$$\epsilon = \frac{S}{E} = \frac{10,000}{17 \times 10^6} = 5.88 \times 10^{-4} \text{ in./in.}$$

D = 2.5 in

$$\Delta D = 2.5 \text{ in } (5.88 \times 10^{-4}) = 1.47 \times 10^{-3} \text{ in}$$

$$TC = 17.64 \times 10^{-6} = \alpha$$

$$\Delta D = \alpha D \Delta T$$

$$\Delta T = \frac{\Delta D}{\alpha D} = \frac{1.47 \times 10^{-3}}{(17.64 \times 10^{-6})\,(2.5)} = 33.3^{\circ}F$$

$$\Delta T = \frac{5}{9}(33.3) = 18.5^{\circ}C$$ ← maximum dynamic range coil wires can withstand

Required dynamic range $-50^{\circ}C$ to $+85^{\circ}C$ = $[135^{\circ}C]$

If coils are wound at $27^{\circ}C$ with no pre-stress and we assume the graphite-epoxy form is significantly stiffer than copper, then

$$-50^{\circ}C - 27^{\circ}C = [77^{\circ}C]$$

and copper would yield.

Copper coils must be wound at:

$$-50 + 18.5 = -31.5C$$

to avoid yielding when temperature is reduced to $-50^{\circ}C$.

Since coil wire is originally at 2.5 in. dia. it will try to increase to a larger dia.

$$\Delta T = -31.5 - 85 = [116.5]$$

$$\Delta D = \alpha D \Delta T = (17.64 \times 10^{-6})\ (2.5)\ (116.5 \times \tfrac{9}{5}) = 0.00925 \text{ in.}$$

However, it is not practical to wind coils at $-31.5^{\circ}C$. Wind at $21^{\circ}C$.

$$-50 + 21 = (71^{\circ}C)$$

$$85 - 21 = (64^{\circ}C)$$

$$\Delta D = (17.64 \times 10^{-6})\ (2.5)\ (71 \times 9/5) = 0.0056 \text{ in.}$$

$$Y_T = 32 - 35 \text{ ksi}$$

$$S = E\epsilon$$

$$S = 17 \times 10^{-6}\ (0.0056/2.5) = 38{,}080 \text{ ksi}$$

This could cause failure of some coil wires.

So back coil form groove with elastomer to allow coil wires to shrink without inducing stress above yield.

At high temperatures, hold coils in place with flexible adhesives.

APPENDIX D

PACKAGING OF THE ELECTRONICS

ANALYSIS: PC BOARD RESONANT FREQUENCY AND STRESS

Circuit Card Weight.

$$4 \text{ in} \times 4 \text{ in} \times 5 \text{ g/in}^2 \times \frac{1}{454 \text{ g/lb}} = 0.176 \text{ lb}$$

Resonant Frequency

Using Steinberg comparison method

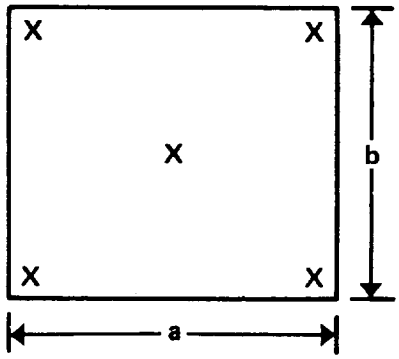

$$f_n = f_1 \frac{0.0768h}{ab} \left(\frac{E}{\rho(1 - u^2)} \right)^{1/2}$$

where

$h = 0.07 \quad a = 4 \quad b = 4$

$E = 2 \times 10^6 \text{ lb/in}^2$ for epoxy glass

$\mu = 0.12$

$$\rho = \frac{0.176}{4 \times 4 \times 0.07} = 0.157 \text{ lb/in}^3$$

From Table in Steinberg

$$f_n = 175 \frac{(0.0768)(0.07)}{4 \times 4} \left(\frac{2 \times 10^6}{0.157(0.9856)} \right)^{1/2} = 211 \text{ Hz}$$

for f_n of 211

$$Q = (f_n)^{1/2} = (211)^{1/2} \sim 14$$

PC Board Stress

Load Factor

Random $g_f = 2.2 (12.9) = 28$

Sine $g_f = Q g_{in} = 14(5) = 70$

Dynamic Load Intensity

$$q_o = \frac{w g_f}{a\ b} = \frac{(0.157)(70)}{4 \times 4} = 0.687 \text{ lb/in}^2$$

Bending Moment

$$M_y = \frac{q_o \left(\frac{\mu}{a^2} + \frac{1}{b^2} \right)}{\pi^2 \left(\frac{1}{a^2} + \frac{1}{b^2} \right)^2} = \frac{0.687 \left(\frac{0.12}{16} + \frac{1}{16} \right)}{\pi^2 \left(\frac{1}{16} + \frac{1}{16} \right)^2} = 0.312 \text{ in. lb/in.}$$

Dynamic Bending Stress

$$S_b = \frac{6 k_T M_y}{h^2} = \frac{6(3)(0.312)}{(0.07)^2} = 1150 \text{ psi}$$

K_T = Stress concentration factor

h = board thickness

$s_b \sim 1200$ psi

MAGSAT Vector Magnetometer

Study Program for Goddard Space Flight Center

by

Time-Zero Laboratories, Gardena, California

Mounting Structure
Design, Mechanics Analysis, and Materials Selection

input by:

Dr. Donald F. Adams, Engineering Consultant

421 So. 19th Street
Laramie, Wyoming 82070

October 1976

Overall Mechanical Design

The general design configuration as presented in the original Time-Zero Laboratories proposal is sound and will remain basically unchanged. This mounting structure consists of a baseplate, sensor mounting tower, a feedback coils support sphere, and a field cancellation coils support sphere.

The following sections describe the rationale for materials selection, the influence of this materials selection on the detail design, and an associated performance analysis.

Materials Selection

The combined requirements of low structural weight and ultra-low coefficient of thermal expansion make the selection of a fiber-reinforced, polymer-matrix composite a logical choice. A graphite fiber is recommended because of its low density, high strength and stiffness, and in particular because of its highly anisotropic thermal expansion properties. The anisotropy of the graphite fiber is caused by prefered orientation of its graphitic (lamellar, plate-like) crystalline structure during manufacture. For example, mechanical stretching of the precursor fiber during the graphitization process will cause this orientation. One result is a high fiber axial stiffness and tensile strength relative to the corresponding transverse properties. Also, the axial coefficient of thermal expansion is very low, actually slightly negative in most cases, while the transverse coefficient of thermal expansion is always positive and relatively large, comparable in magnitude to the coefficient of thermal expansion of common isotropic metals such as steel, aluminum, or magnesium. A wide variety of graphite fibers are commercially available, permitting the selection of one having the optimum combination of stiffness, strength, and thermal expansion anisotropies for a specific application.

A number of different polymer matrix materials are also readily available, including epoxy, polyester, phenolic, and polyimide, to name the most appropriate candidates for the present application. These polymers are all isotropic, and differ little in density, strength, or stiffness from one to another. Polyester is lowest in cost, but is the least thermally stable. Polyimide is a high temperature polymer (300°C or higher service temperature), but is somewhat more difficult to fabricate structures from since it is not as of yet as well-developed as the others. A comparison of a variety of factors such as these leads to the firm conclusion that epoxy is the best choice for the present application. While a large number of epoxy resins are commercially marketed, their mechanical and physical properties

do not differ significantly. Thus, unlike graphite fibers, the selection of a specific epoxy matrix material is not a critical factor.

Graphite/epoxy composites of three different basic configurations were considered for the present application: unidirectional, angle-ply, and chopped fiber. Each configuration has distinct advantages and disadvantages. Which to use depends upon the component design configuration, as discussed in the following paragraphs.

Baseplate - This component is a relatively simple, flat, rectangular plate, 8.5" long, 5.0" wide, and 0.5" thick. Two alignment mirrors are attached to one face, and the sensor mounting tower to the opposite face. The principal requirements are a high out-of-plane stiffness (i.e., bending and torsional rigidity) and low weight. A uniformly low coefficient of thermal expansion (i.e., low in all in-plane directions) is an important secondary property, to minimize out-of-plane distortions due to thermal gradients across the surface of the plate.

solid plate:

$$\text{volume} = 8.5 \times 5.0 \times 0.5 = 21.25 \text{ in}^3$$

$$\text{weight} = 21.25 \text{ in}^3 \times 0.058 \text{ lb/in}^3 = 1.233 \text{ lb}$$

The desire for thermal isotropy and high torsional rigidity suggests a $[0, \pm 45, 90]_S$ laminate, i.e., equal numbers of unidirectionally reinforced plies or laminae oriented at 0, +45, -45, and 90 degrees relative to the length axis of the plate, the total number of plies being as required to produce the desired plate thickness, and the resulting stacking sequence being symmetric about the thickness midplane of the plate.

As a general guideline, the higher the (axial) modulus of the graphite fiber selected, the higher the in-plane (quasi-isotropic) stiffness of the composite, the lower the coefficient of thermal expansion (always slightly positive), the lower the in-plane strain to failure, and the higher the material cost. Commonly

available commercial graphite fibers range in modulus from about 25×10^6 to 80×10^6 lb/in^2. Properties of typical graphite/epoxy materials, in isotropic (or more correctly, quasi-isotropic) laminated plate form, are given in Table 1.

One very important property of these composites is their very low coefficient of thermal expansion, α, and their low density. For example, invar, a metal generally considered when low thermal expansion is required, has a coefficient of thermal expansion, α, of 1.4×10^{-6}/°C, and density of 0.289 lb/in^3. That is, it has an expansion coefficient comparable to or even higher than that of the composites of Table 1, and is about five times heavier.

One apparent anomoly in Table 1 is the lower value of α for T300/5208 relative to HMS/3501-5, this value being much lower than that of AS/3501-5 also. While the coefficient of thermal expansion does vary from one epoxy resin to another, this alone probably does not account for the total difference in Table 1. A slight variation in fiber volume content from one system to another is also a contributing factor. A $\pm$5 percent variation in fiber volume content is not untypical; slight differences in resin viscosity can influence the resin flow during the temperature-pressure-time cure cycle. As important, however, is the ability to accurately measure these very low values of α. It has only been during the past year or so that effort has been concentrated on developing reliable techniques for measuring very low values. Thus, much of the data in the literature, from which the properties of Table 1 were taken, are of limited experimental accuracy. There is no question, however, that the value of α for any isotropic lay-up, graphite/epoxy composite is very low. In any current program, this property should be experimentally measured for the particular material system being used.

While considering thermal expansion coefficients, it should also be noted that fuzed quartz, the mirror material used in the present system, has a coefficient of thermal expansion of about 0.5×10^{-6}/°C. Thus, the isotropic laminate, graphite/epoxy baseplate matches this property of the mirrors very well. This

Table 1
Properties of Typical Isotropic Lay-up $[0,\pm45,90]_S$ Graphite/Epoxy Composite Materials

Material Designation	AS/3501-5	T300/5208	HMS/3501-5	T75S/3501-5
Supplier*	Hercules [1]	Narmco [2]	Hercules [1]	Union Carbide [3]
Fiber Type	low modulus high strength	low modulus high strength	medium modulus medium strength	high modulus high strength
Prepreg Cost ($/lb)	55	55	90	275
Elastic Modulus, $E(10^6$ lb/in$^2)$	6.6	8.1	10.1	15.8
Shear Modulus, $G(10^6$ lb/in$^2)$	2.6	2.5	3.9	6.0
Poisson's Ratio, ν	0.35	0.31	0.30	0.32
Coefficient of Thermal Expansion, $\alpha(10^{-6}/°C)$	2.29	0.49	1.12	0.39
Tensile Strength, $\sigma_u(10^3$ lb/in$^2)$	86	60	60	116
Shear Strength, $\tau_u(10^3$ lb/in$^2)$	35	31	36	32
Density, ρ (lb/in^3)	0.055	0.058	0.058	0.058
Thickness/Ply (in)	0.0052	0.0060	0.0077	0.0077

*Numbers in brackets indicate reference sources; isotropic lay-up properties computed using laminated anisotropic plate theory and unidirectional properties when experimental data not available for isotropic laminates.

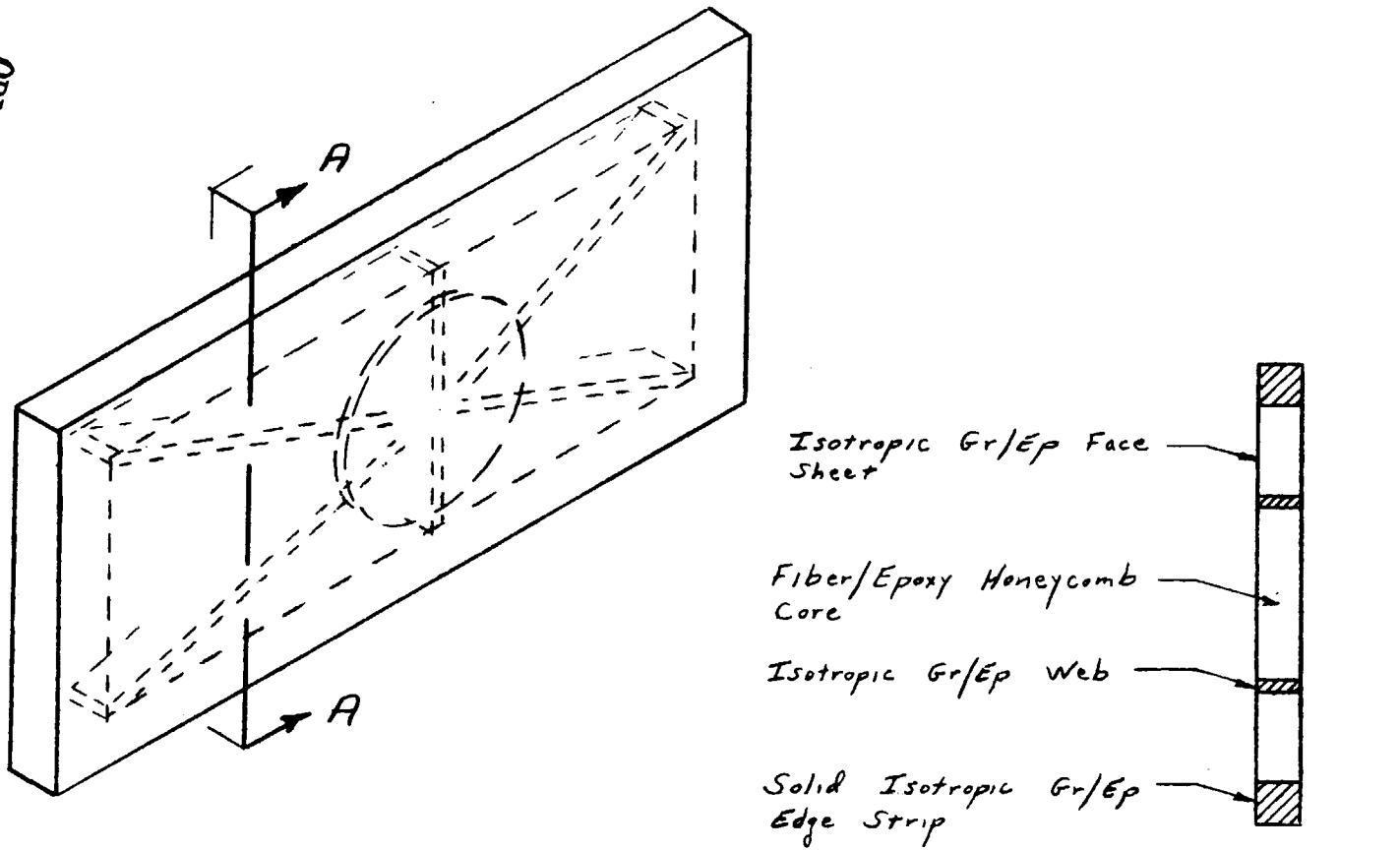

FIG. 1 : MAGNETOMETER BASEPLATE - COMPOSITE SANDWICH CONSTRUCTION

DFA
10/17/76

will permit adhesive bonding of the mirrors to the baseplate, without developing subsequent thermal expansion mismatch stresses and distortions in either component.

For the present baseplate design, any one of the materials of Table 1 would be satisfactory. All factors considered, the HMS/3501-5 system has been selected, based primarily on a good balance of elastic and shear moduli, an acceptable coefficient of thermal expansion, and a moderate cost. The excessive cost and therefore the lack of extensive use of the T75S/3501-5 system in prior applications has resulted in a limited data base, making the selection of this obviously attractive material unadvisable. Another high modulus graphite fiber, GY-70, produced by Celanese, Incorporated [4], is in a similar position of having a limited data base, although for different reasons. A typical composite form is GY-70/X-505, a graphite/epoxy prepreg produced by Fiberite Corporation [5]. While the cost is comparable to other, more commonly used systems, the high fiber modulus combined with a low to moderate strength results in a low strain to failure. That is, the material has developed a reputation for being somewhat brittle in certain applications. Efforts by the material supplier to increase the composite strength properties, by improving the fiber surface treatment and by modifying the epoxy matrix properties, are making this a steadily improving material system, however.

Should structural weight savings become an even more critical consideration than at present, the baseplate configuration should be the first for reevaluation during detail design. Two changes could be considered, each of which would result in a significant percentage weight savings. The most direct change would be to switch to a sandwich panel configuration, incorporating a fiber/epoxy honeycomb core and graphite/epoxy face sheets. Shear webs radiating from the region of the sensor mounting tower attach point would be added to transmit out-of-plane bending loads and to minimize deflections. A sketch of this configuration is shown in Figure 1. Fiber/epoxy honeycomb core weighs in the range of 5 to 15 lb/ft^3

(0.003 to 0.009 lb/in^3), depending upon cell size and fiber type. Thus, a total weight savings of as much as one-half pound relative to the solid plate design could be achieved, at a modest increase in cost.

The second modification, to achieve an even greater weight savings, would be to make the alignment mirrors an integral part of the baseplate. The two quartz mirrors are approximately 4" x 4" x ½" and 3½" x 3½" x 2" in size, respectively, containing a total of about 25 in^3 of fused quartz (after allowing for the non-planar contour of the latter mirror). Fuzed quartz weighs 0.080 lb/in^3. Thus, the two mirrors have a combined weight of about 2 lb. Quartz is selected as a mirror material because of its good stiffness ($E = 10.4 \times 10^6$ lb/in^2) and low thermal expansion ($\alpha = 0.5 \times 10^{-6}/°C$). As indicated in Table 1, the various graphite/epoxy isotropic laminate composites have comparable or even superior in-plane properties. The mirror side of the baseplate could be molded to the required mirror contour shape, polished to the flatness desired, and metal-plated. This general technique is currently being evaluated for weapon systems applications by industry [6]. By using this technique, most of the 2 lb. quartz mirror weight could be saved.

Sensor Mounting Tower - This component (see Fig. 2) serves two principal functions; it supports the sensors and provides a mounting base for the two coil spheres. Its required properties are compatible thermal expansion coefficients, and a high flexural stiffness.

The 2.5 diameter base ring which supports the field cancellation coil sphere (outer sphere) will be adhesively bonded (or possibly co-cured) onto the baseplate. Thus, it must have thermal expansion properties which at least approximately match those of the baseplate, and it must also be thermally isotropic so that it does not induce thermal stresses and distortions into the field cancellation coil sphere. Therefore, the 2.5" diameter base ring will be made of the same material

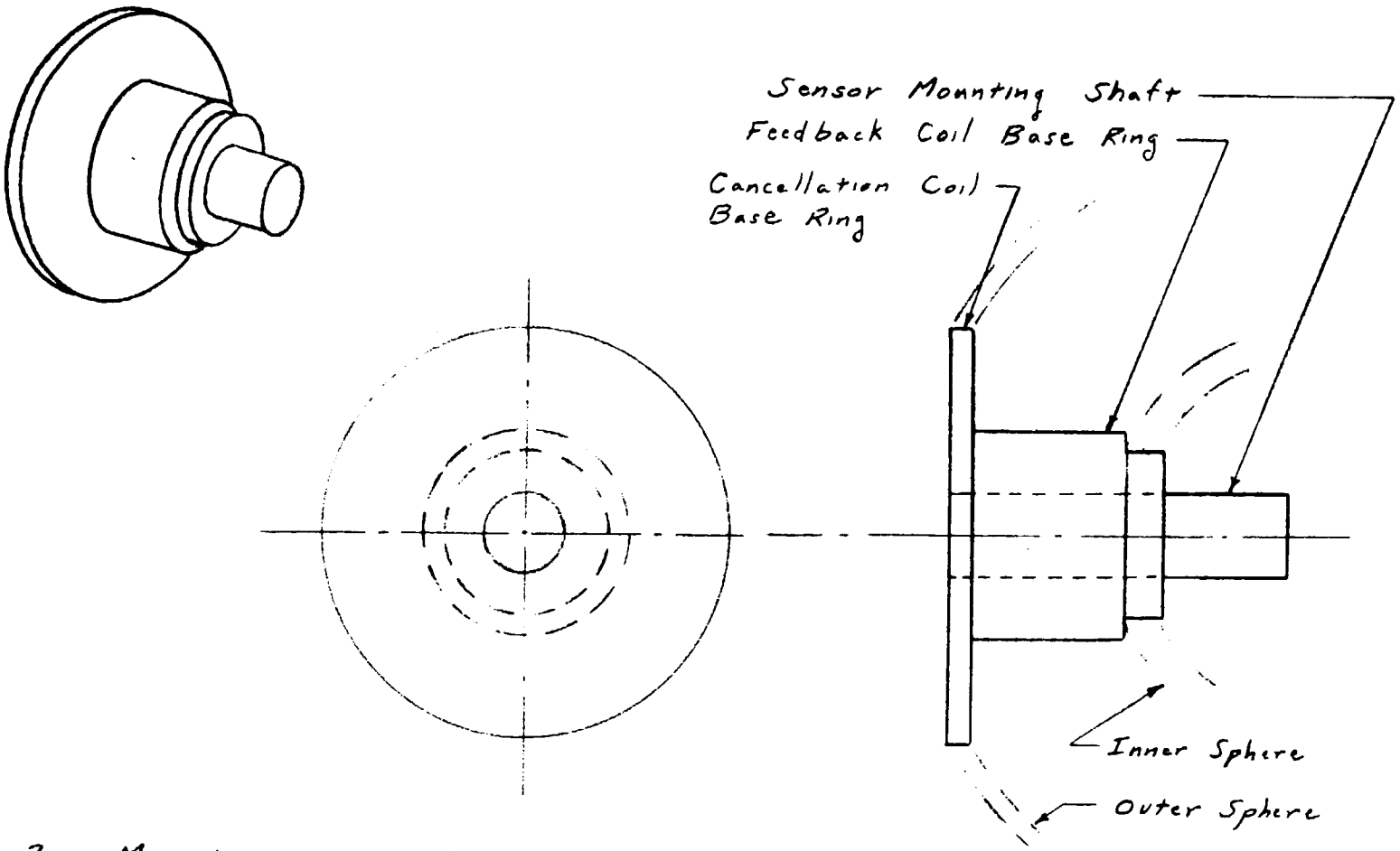

FIG. 2 : MAGNETOMETER SENSOR MOUNTING TOWER

as the baseplate, i.e., an HMS/3501-5 isotropic laminate. The thickness of this base ring will be such as to match the effective wall thickness of the outer sphere it mates with, i.e., slightly greater than 0.10".

The 1.25" diameter feedback coil base ring will be of the same material, for the same reasons. The depth of the sphere mounting step will be slightly greater than 0.20", to match the effective wall thickness of the inner sphere. The diameter of this step is 1.0".

The cancellation coil base ring and the feedback coil base ring are to be constructed of an isotropic laminate in order to match the radial thermal expansion of the cutouts in the spheres at their junction. The plies of the laminate thus lie in a plane perpendicular to the axis of the mounting tower. For the HMS/3501-5 composite, the elastic modulus and coefficient of thermal expansion in this (tower axis) direction are 1.1×10^6 lb/in^2 and 25×10^{-6}/°C, respectively. That is, this material has a low stiffness (low resistance to lateral flexural deflection of the tower axis) and high thermal expansion (poor thermal stability) in the axial direction.

To offset these undesireable properties, the sensor mounting shaft will be made of undirectional GY-70/X-505 high modulus graphite/epoxy (or T75S/3501-5 graphite/epoxy as a comparable alternate material), with the fibers oriented in the axial direction and the shaft running the entire length of the tower, as shown in Fig. 2. The properties of this material are given in Table 2.

The combination of a slightly negative axial coefficient of thermal expansion and a very high axial modulus combine to offset the poor thermal stability of the mating base rings. The high axial (flexural) elastic modulus provides the required flexural rigidity of the tower.

As given in Table 2, the transverse coefficient of thermal expansion of the unidirectional composite is very high, 31.7×10^{-6}/°C, and the transverse elastic modulus is very low, 0.9×10^6 lb/in^2. This high value of α is a disadvantage

Table 2
Properties of Unidirectional GY-70/X-505
Graphite/Epoxy Composite [5,7]

Elastic Modulus (10^6 lb/in^2)		
	Axial	44
	Transverse	0.9
	Flexural	41
Shear Modulus	0.6×10^6 lb/in^2	
Coefficient of Thermal Expansion (10^{-6}/°C)		
	Axial	-1.04
	Transverse	31.7
Density	0.061 lb/in^3	

in the sense that radial interface stresses will be developed between the shaft and rings due to any temperature change. However, this will be alleviated significantly because of the low transverse elastic modulus of the shaft. On the other hand, the high value of α is an advantage since it will permit shrink-fitting the shaft into the hole in the base rings. That is, the shaft can be cooled to shrink its diameter and then slipped into the hole. (There is no significant benefit in also heating the base rings since the coefficient of thermal expansion of this material is so low.) By controlling the shrink fit interference, a secure connection can be assured under all service temperature excursions above and below ambient.

Feedback Coils Support Sphere - The principal structural requirement of the feedback coils support sphere is a uniform and very low coefficient of thermal expansion. Each of the three pairs of coil windings must remain parallel within a small tolerance, and remain at a prescribed spacing within a small tolerance.

The requirement of uniform and low thermal expansion would be satisfied by any of the isotropic laminate composites listed in Table 1. However, it is not practical to fabricate a sphere in isotropic laminate form. It is difficult to maintain the fixed fiber-orientation angles around the surface. The most likely fabrication technique would be filament-winding; but this would not produce the required isotropy. The fiber angles at the winding axis poles would not be the same as at the equator. Hand lay-up of unidirectional prepreg material is also impractical because of the close tolerances required.

A viable alternative is to mold the sphere from a chopped fiber/epoxy molding compound or structural mat. The latter is a prepreg material available in sheet or roll form. It can be cut into random-size pieces and layed over a spherical mandrel, then vacuum bag cured to the finish dimensions using spherical segment caul plates to control the external surface smoothness and wall thickness. While this is not a standard fabrication procedure in the composites industry, it is not

expected to present any difficulties. The mat material is prefered over the molding compound for the present application because of the better control of fiber orientation in the surface plane of the sphere. Less fiber flow will occur during the curing process.

The chopped fiber in the mat prepreg material is randomly oriented in the plane of the mat. Thus, the composite exhibits in-plane isotropy. To achieve a very low coefficient of thermal expansion, it is necessary to use a very high modulus graphite fiber. This also maximizes the in-plane elastic modulus. One such material is hy-MAT 7534 structural prepreg [5] produced by Fiberite Corporation. The properties of this material are given in Table 3. The fiber is GY-70 graphite, chopped to a nominal length of 1 inch. The matrix is Fiberite 934 epoxy. The value of the isotropic coefficient of thermal expansion of $1.4 \times 10^{-6}/°C$ matches very closely the value of $1.12 \times 10^{-6}/°C$ for the isotropic lay-up HMS/3501-5 laminated composite of Table 1. The elastic moduli also are relatively close for these two materials. Thus, the molded sphere will mate with the base ring of the mounting tower with a minimum of thermal expansion mismatch. Adhesive bonding will be quite satisfactory.

Annular grooves will be machined in the outer surface of the molded sphere to carry the coil windings. Each groove must accommodate 273 turns of #36 copper wire (0.005" diameter), the wire having an insulation coating resulting in a total diameter of 0.0055". The shape of the groove is not critical; a rectangular geometry is selected as being simple to machine into the sphere. The diameter of each coil ring is to be large enough such that the rings laying in the three orthogonal planes will have to cross over each other at several points. Thus, in order to maintain the circular shape of each coil ring, the grooves into which these coils are wound will have to be of three different depths. That is, if one set of parallel grooves is of depth b, the next set must be of depth 2b, and the third set of depth 3b. Thus, it is desireable to make b as small as practical. It has been decided that a practical upper limit to the ratio of coil winding width to depth is

Table 3
Properties of hy-MAT 7534 High Modulus Graphite/Epoxy
Structural Mat Chopped Fiber Composite [5]

Elastic Modulus	(10^6 lb/in^2)
Axial	12.5
Flexural	12.0
Ultimate Strength	(10^3 lb/in^2)
Tensile	35.0
Compression	26.0
Flexural	50.0
Coefficient of Thermal Expansion	1.4×10^{-6}/°C
Density	0.060 lb/in^3
Fiber Volume	55 percent
Fiber Length	1 in. (nominal)
Thickness/ply	0.020 in.
Prepreg Cost	$80/lb.

about 4. A coil winding of 35 turns width wound to a depth of 8 turns gives a ratio of 4.38, a reasonable value. For a coated wire diameter of 0.0055", a groove 0.193" wide and 0.044" deep is adequate. Thus, the second set of grooves will be 0.088" deep, and the third set 0.132" deep.

The wall thickness of the sphere must be adequate to accommodate these deepest grooves while retaining adequate strength and stiffness. A wall thickness of 0.200" has been selected, resulting in a minimum section thickness of 0.068" at the deepest grooves. The chopped fiber composite has adequate strength (see Table 3) to permit this. This material is also essentially insensitive to stress concentrations because of its fibrous nature. Thus, the presence of the groove will not induce a local failure at the bottom corner of the groove. Since the highest flexural stresses will occur in the region of the attachment of the sphere to the base ring, the coil grooves oriented in the planes parallel to this base ring will be designed to be the shallowest. It is immatieral from a strength standpoint as to which of the other two sets of grooves is the deepest, the sphere geometry being symmetrical in this sense.

It should be noted that because of the different depths of the grooves, the resulting diameters of the coil windings will be slightly different, differing from one another by 0.088". Also, because of the necessity of having an opening in the sphere of sufficient size to permit the insertion of the sensor core assembly, the maximum diameters of the pairs of coils laying in planes parallel to the sensor mounting tower axis is limited. That is, the minimum spacing between these pairs of coils is limited by the required size of the opening. Denoting the radius of any pair of rings as R, and the spacing between the rings as 2x, the minimum permissible value of x will be approximately 0.75R.

Another important design consideration is the tension with which the copper wire is wound into the grooves. Two factors must be considered: the prestressing

effect on the sphere, and the thermal expansion mismatch between the copper and the graphite/epoxy composite during any service temperature change. The properties of the copper wire are given in Table 4, the wire being used in annealed form. The high coefficient of thermal expansion of the copper wire relative to the graphite/epoxy sphere means that the windings will tend to loosen with any increase in temperature, and tighten onto the sphere with any decrease. Excessive expansion could cause a local buckling of the wire bundle, and hence a permanent distortion of the coil geometry. Excessive contraction could induce a fracture of the sphere in the region of the groove. A stress analysis of these effects is presented in the analysis section of this report.

To alleviate this thermal stress problem, the use of selective reinforcement of the sphere at the inner surface was considered. A thin band of graphite/epoxy composite bonded to the inside surface of the chopped fiber mat, graphite/epoxy sphere directly under each coil winding groove would enhance the local strength significantly. This can be fabricated relatively easily since the band material can be positioned inside the sphere while in an uncured (prepreg) condition, and then cured in place. The negative aspect of this approach is that the uniformity of the basic molded sphere will be distorted. In particular, the sphere will no longer be isotropic in terms of stiffness and thermal expansion, which could lead to excessive thermal distortions. While a careful materials selection and design would minimize this possibility, the strength reduction problem is not severe enough to warrant the additional fabrication complexity and performance uncertainty associated with using stiffness rings. Had strength reduction been found to be a problem, a better solution would have been to increase the wall thickness of the sphere.

Table 4
Properties of CDA* No. 102 Oxygen-Free Copper
in Annealed Form [8]

Elastic Modulus	17×10^6 lb/in^2
Shear Modulus	6.4×10^6 lb/in^2
Tensile Strength	(10^3 lb/in^2)
Yield (0.5% offset)	10-11
Ultimate	32-35
Elongation (in 2")	45-55 percent
Coefficient of Thermal Expansion	17.6×10^{-6}/°C
Specific Heat	0.166 BTU/lb/°C
Thermal Conductivity	407 BTU/hr/ft^2/°C/ft
Electrical Resistivity	1.71 microhm-cm
Density	0.323 lb/in^3

* Copper Development Association

Field Cancellation Coils Support Sphere - The design problems associated with this component are essentially identical to those discussed in relation to the feedback coils support sphere, and the same graphite/epoxy chopped fiber composite mat will be used. The principal difference is that only 68 turns of the same #36 copper wire are required per coil. Thus, the depth of the grooves can be less. The same assumption of a desirable ratio of coil winding width to depth ratio of 4 or less applies. A coil winding of 17 turns width wound to a depth of 4 turns gives a ratio of 4.25, a reasonable value. For a coated wire diameter of 0.0055", a groove 0.094" wide and 0.022" deep is adequate. Thus, the second set of grooves will be 0.044" deep, and the third set 0.066" deep. A wall thickness of the sphere of 0.100" will result in a minimum section thickness of 0.034" at the deepest grooves.

As in the case of the smaller sphere, the shallowest grooves will be those oriented in planes parallel to the base ring. Likewise, the coil windings will be of different diameters, differing in this case by 0.044". In order for the inner sphere to be inserted inside this sphere, the diameter of the opening must be slightly larger than 2.5". Thus, the same coil radius to spacing ratio applies for this larger sphere as discussed previously for the small sphere. That is, the minimum permissible value of x will be approximately 0.75 R.

The interiors of both spheres will be vented to the exterior, to eliminate any induced stresses due to pressure differentials.

References

1. "Advanced Composites - Products and Capabilities Summary," Hercules, Inc., Bacchus Works, Magna, Utah, October 1976.

2. "Modmor Technical Bulletin," Whittaker Corp., Narmco Materials Division, Costa Mesa, California, 1975.

3. "Technical Information Bulletin," Union Carbide Corp., Carbon Products Division, New York, N.Y., 1975.

4. "Advanced Engineering Composites," Celanese Corp., Summit, New Jersey, 1976.

5. "Fiberite hy-E Advanced Composite Materials," Fiberite Corp., Winona, Minnesota, October 1976.

6. J.L. Perry, Private Communication, Aeronutronic Ford Corp., Aeronutronic Division, Newport Beach, California, October 1976.

7. "Advanced Composites Design Guide, Volume IV - Materials," Third Edition, Air Force Materials Laboratory, January 1973 (revised December 1975).

8. 1976 Materials Selector," Materials Engineering, Reinhold Publishing Corp., Stamford, Connecticut, Vol. 82, No. 4, Mid-September 1975, p. 75.